UNIVERSITY OF CALIFORNIA SAN DIEGO

Polymer Supercapacitors for Self-powered Electronics Applications

A Dissertation submitted in partial satisfaction of the requirements
for the degree Doctor of Philosophy

in

Materials Science and Engineering

by

Lulu Yao

Committee in charge:

Professor Tse Nga Ng, Chair
Professor Hanh-Phuc Le
Professor Ping Liu
Professor Xinyu Zhang

2024

THE DISSERTATION OF LULU YAO IS APPROVED, AND IT IS ACCEPTABLE IN QUALITY AND FORM FOR PUBLICATION ON MICROFILM AND ELECTRONICALLY.

University of California San Diego

2024

DEDICATION

To my family.

To all who supported me.

To all who helped me to learn and grow.

.

TABLE OF CONTENTS

LIST OF FIGURES

LIST OF TABLES

ACKNOWLEDGEMENTS

Chapter 2, in part, is a reprint of the material as it appears in Cell Reports Physical Science. Jiaxi Liu, Naresh Eedugurala, Paramasivam Mahalingavelar, Daniel J Adams, Kaiping Wang, Kevin S Mayer, Jason D Azoulay, Tse Nga Ng. Ultrafast high-energy micro-supercapacitors based on open-shell polymer-graphene composites. The dissertation author was the primary investigator and first author of the paper.

Chapter 3, in part, is a reprint of the material as it appears in Science Advances. Kai Zheng, Nandu Koripally, Naresh Eedugurala, Jason D Azoulay, Xinyu Zhang, Tse Nga Ng. Structural pseudocapacitors with reinforced interfaces to increase multifunctional efficiency. The dissertation author was the primary investigator and first author of the paper.

Chapter 4, in part, is a reprint of the material as it appears in ACS Energy Letters. Kaiping Wang, Lulu Yao, Mehran Jahon, Jiaxi Liu, Matthew Gonzalez, Ping Liu, Vincent Leung, Xinyu Zhang, Tse Nga Ng. Ion-exchange separators suppressing self-discharge in polymeric supercapacitors. The dissertation author was the primary investigator and co-first author of the paper.

VITA

2016 Bachelor of Science, Shanghai Jiao Tong University, Shanghai, China

2019 Master of Science, Shanghai Jiao Tong University, Shanghai, China

2024 Doctor of Philosophy, University of California San Diego, USA

PUBLICATIONS

[1] Wang, k., **Yao, L.**, Jahon M., Liu J., Gonzalez M., Liu, P., Leung V., Zhang, X., Ng, TN., ion-exchange separators suppressing self-discharge in polymetric supercapacitors. ACS Energy Letters 5(2020): 3276-3284

[2] **Yao, L.**, Zheng, K., Koripally, N., Eedugurala, N., Azoulay, J. D., Zhang, X., & Ng, T. N. "Structural pseudocapacitors with reinforced interfaces to increase multifunctional efficiency." *Science Advances* 9, no. 25 (2023): eadh0069.

[3] **Yao, L.**, Liu, J., Eedugurala, N., Mahalingavelar, P., Adams, D.J., Wang, K., Mayer, K.S., Azoulay, J.D. and Ng, T.N., Ultrafast high-energy micro-supercapacitors based on open-shell polymer-graphene composites. *Cell Reports Physical Science*, *3*(3). (2022).

ABSTRACT OF THE DISSERTATION

Polymer Supercapacitors for Self-powered Electronics Applications

by

Lulu Yao

Doctor of Philosophy in Materials Science and Engineering

University of California San Diego, 2024

Professor Tse Nga Ng, Chair

The development of self-power electronics has attracted wide-spread attention owing to their potential applications in internet of things (IoT), nanorobotics, health monitoring, wireless communications, *etc*. However, the harvested energy resources (solar energy, thermal energy, radio frequency energy, *etc*.) are normally intermittent and unpredictable, so suitable energy

storage devices that can store collected energies and have a stable are in high demand. Supercapacitors typically show a high-power density and an extended cycling life (>10,000 cycles) that perfectly fit the requirement of self-powered electronics. However, their practical applications are limited by the low energy densities and significant self-discharge problem.

To enhance the performance of the supercapacitors, we demonstrated the electro-deposition of an open-shell conjugated polymer with reduced graphene oxide achieves electrodes with capacitance up to 186 mF cm^{-2} (372 F cm^{-3}). The extended delocalization within the synthesized polymer stabilizes the redox states and facilitates a 3 V wide potential window, while the hierarchical composite electrode structure promotes ultrafast kinetics. The micro-supercapacitor shows a high-power density of 227 mW cm^{-2} with an energy density of 10.5 μWh cm^{-2} and stability of 84% capacitance retention after 11,000 cycles. These attributes allow operation at 120 Hz for fast charging and alternating current line filtering applications, which may be suitable to replace bulky electrolytic capacitors or serve as high-endurance energy storage for wireless electronics.

Beyond the electrode material development, a novel supercapacitor configuration, structural supercapacitor was also developed to enhance the energy density of the whole device. A gradient structural electrolyte was designed for structural supercapacitor to balance its ionic conductivity and mechanical strength. By combining this electrode-electrolyte system, a structural supercapacitor that can replace the metallic chassis of transportation vehicles to provide extra electricity was fabricated. The structural supercapacitor was shaped into the hull of a model boat with a solar energy harvesting system, and it achieved both a high electrochemical and mechanical strength compared to its monofunctional counterparts. The demonstration was a promising prototype to show that structural energy storage can complement energy harvesting system to make

electronics more energy-autonomous, requiring less maintenance cost if we have billions of electronics that can have operated on self-recharge.

In addition, to enhance the efficiency of the self-powered electronics, an ion-exchange mechanism was also developed to suppress the self-discharge problem of energy storage units of self-powered electronics. This design increases the charging efficiency of the device and prevents the loss of stored energy during standby. It was demonstrated to work with radio frequency energy-harvesting circuits and showed the potential to serve as an energy reservoir for wireless electronic applications.

CHAPTER 1: INTRODUCTION

1.1 Development of Self-Powered Electronics

Nowadays, portable electronics have become an indispensable component of everyday life, from global communication networks to personal health monitoring,[1,2] like sophisticated satellites, computers, mobile phones, and compact health sensors (Figure 1.1). The communications among these devices, a cornerstone of the Internet of Things (IoT), hinges on the efficient collection and transmission of data, facilitated by advanced sensors and signal emitters. To sustain these critical functions, the deployment of appropriate power sources is important. As illustrated in Figure 2.2, these power sources are categorized into three distinct types: distribution, harvesting, and storage.[3] Each type plays an important role in the operation of IoT electronics. However, their applications in small and portable devices, where size and efficiency constraints pose significant challenges, are highly limited. This necessitates ongoing development and optimization of power source technology to meet the growing demands of portal IoT electronics.[4]

To solve this concern, self-powered electronic devices[5] (Figure 1.3) was introduced in applications of internet of things (IoT)[6], nanorobotics[7], health monitoring[8], and wireless communications[9], *etc*. These electronics normally harvest energies like solar energy, thermal energy, and radio frequency energy, *etc*. from environment, thus avoiding the complex power system and further maintenances.[3] But the power supply of these energy resources are intermittent and unpredictable, so a suitable electrochemical storage devices that is able to store collected energies then output a stable power is highly demand.

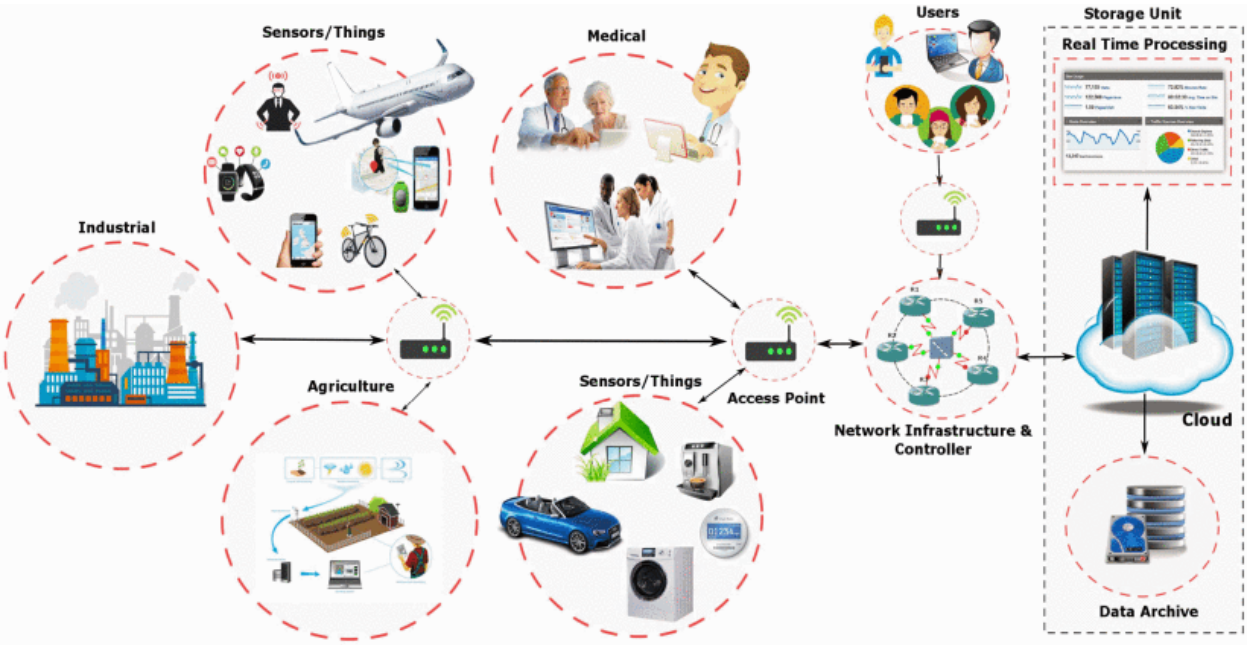

Figure 1.1. Internet of things (IoT) architecture.[1]

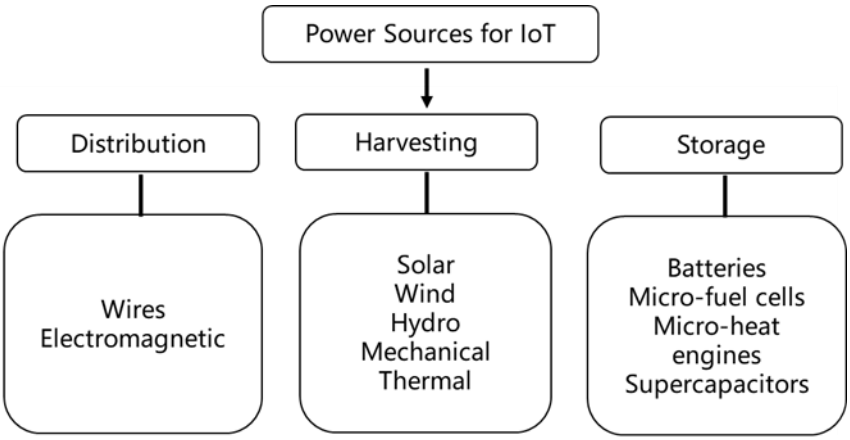

Figure 1.2. The Power Sources of IoT devices.[3]

Figure 1.4 presents a comprehensive summary of the power and energy densities of various energy sources alongside sensor/signal emitters[10]. For self-powered electronics to function effectively, the chosen energy storage devices must possess higher energy and power densities than the sensor/signal emitters[11]. Additionally, these storage devices need to be chargeable by different types of energy sources. Figure 1.5 illustrates two examples of self-powered electronics:

one utilizing a solar panel and the other employing a piezoelectric generator (PEG) as the energy sources.[12,13] In both cases, supercapacitors are utilized to store the harvested energy, which is then used to power the gas sensors. Micro-supercapacitors are utilized for these applications because they are easier to integrated into the whole system and they long cycling life.

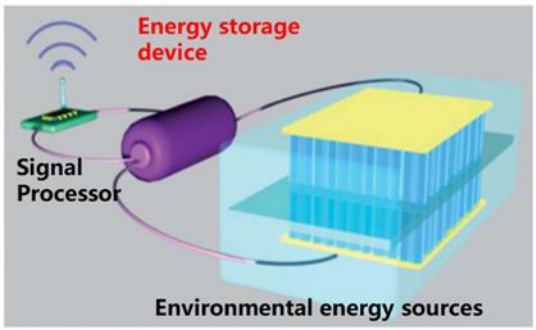

Figure 1.3. The scheme of self-powered IoT devices. The prototype of an integrated self-powered system by using a nanogenerator as the energy harvester.[14]

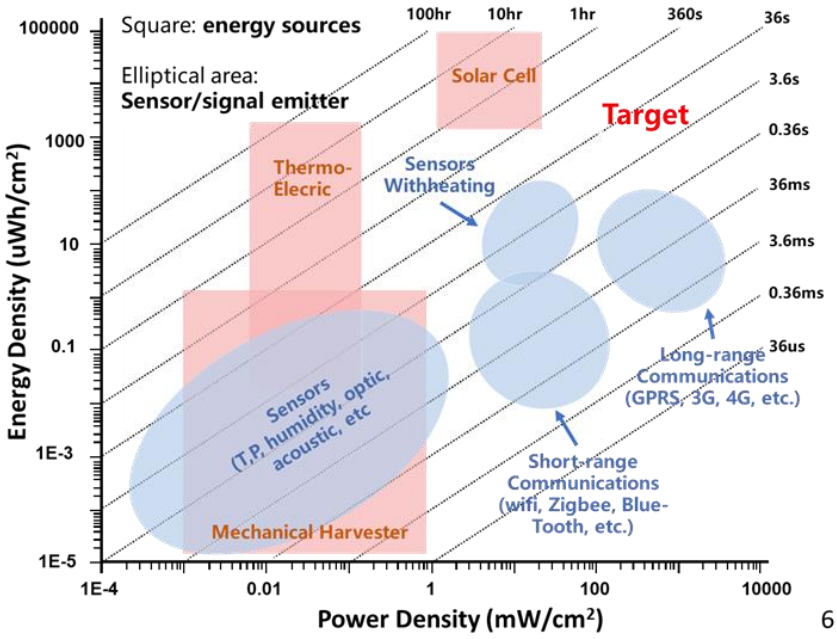

Figure 1.4. The summary of power and energy density of energy sources and sensor/signal emitter for IoT self-powered electronics.[10]

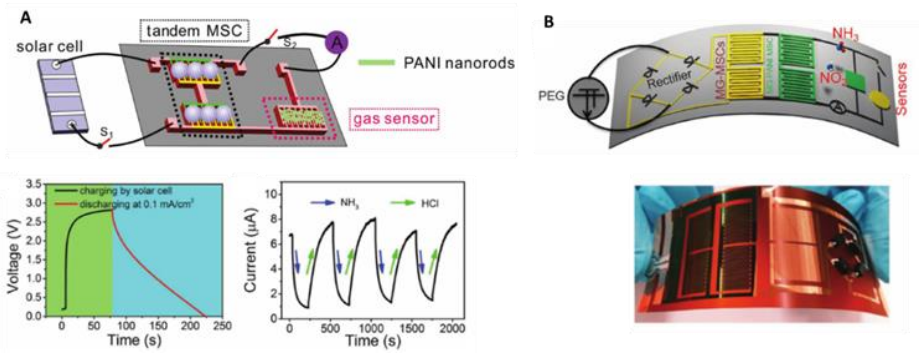

Figure 1.5. Application examples of self-powered electronics. (a) Solar panel powered gas sensor.[12] (b) PEG powered gas sensor.[13]

1.2 Electrochemical Supercapacitors for IoT devices

1.2.1 Working Mechanism of Electrochemical Supercapacitor

Since the innovation of the first Cu-Zn battery, the field of energy storage devices has undergone rapid developments for 2 centuries and given rise to diverse energy storage devices.[15,16] Among them, batteries and supercapacitors are the most important energy storage technologies for daily life, and support the work from portable electronics to large scale energy storage grid[17]. As depicted in Figure 1.6, these two types of devices employ different energy storage mechanisms[18]: supercapacitors store energy on the surface of their electrodes through electrostatic and electrochemical adsorption. In contrast, batteries store energy within the bulk of their materials, primarily through redox reactions with ion insertion into the electrode structure. This difference in energy storage mechanisms results in distinct performance characteristics for battery and supercapacitors. Batteries typically exhibit several order higher energy densities than supercapacitors, enabling them to store more energy per unit volume or mass. However, this comes at the cost of a shorter cycling life (< 800 cycles) and lower power density than supercapacitors. On the other hand, supercapacitors, while generally possessing a lower energy density, boast a significantly higher power density and an extended cycling life (>10,000 cycles).[19] These

differences showed the unique advantages and limitations of each technology, making them suitable for different applications in energy storage area.[17]

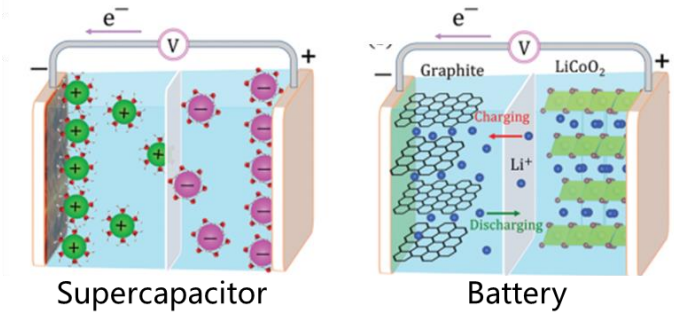

Figure 1.6. Energy storage mechanism comparison between supercapacitor and battery.[21]

As showed in Figure 1.5, powering the sensors and signal emitters integral to IoT devices necessitates the careful selection of power sources with appropriate power density and energy density. While both batteries and supercapacitors are capable of supporting the operation of IoT devices, their distinct characteristics determine the maintenance and efficiency of these IoT devices. Batteries, known for their higher energy density, are capable of sustaining IoT devices for extended periods. However, their relatively short cycling lifetime necessitates frequent replacements, and substantial maintenance costs. This drawback is particularly significant in IoT applications where consistent, long-term operation is needed. In contrast, supercapacitors stand out due to their extended cycling life, making them more suitable for IoT applications that do not require continuous operation. For example, in self-powered IoT devices that have intermittent energy supplies, the long cycling life of supercapacitors offers a more practical and cost-effective solution to the whole system. Of course, the low energy density of supercapacitors also limits the operating time of the signal emitter, thus not suitable for lots of applications. To solve this concern, looking for innovative strategies to enhance the energy density of supercapacitors become highly needed.[20] By increasing their energy storage capabilities, supercapacitors could become more

versatile and widely applicable in a range of IoT scenarios, bridging the gap between longevity and energy capacity of IoT devices.

Typically, supercapacitors are categorized into two different types: electrical double-layers capacitor (EDLC) and electrochemical supercapacitors.[22] For the EDLC, the energy is stored on the interface between electrode materials (*e.g.* activated carbon, AC) and electrolytes. The capacitance can be calculated based on equation 1.1:

$$C = \frac{A\varepsilon}{4\pi d} \quad \text{Equation 1.1}$$

in which A is the interface area, ε is the dielectric constant and d is the distance between cathode and anode. The distance between cathode and anode in EDLC is much smaller than conventional capacitor (*e.g.* aluminum electrolytic capacitors and ceramic capacitor), which is the thickness of single layer atom (0.3 nm – 0.8 nm). Meanwhile, the electrode materials of EDLC normally have large surface areas. The surface area of commercial activated carbon is over 1000 m^2 g^{-1}, several order higher than the conventional capacitor[23].

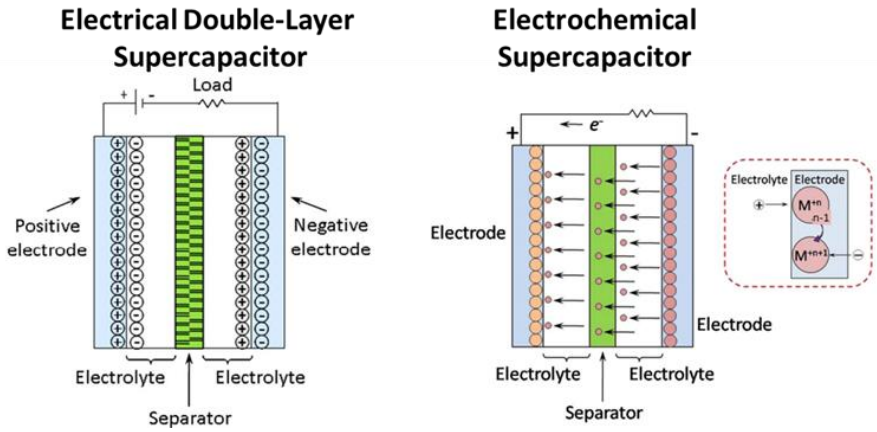

Figure 1.7. Comparison between EDLC and electrochemical supercapacitor.[24]

Compare with EDLC, the electrode surface of electrochemical supercapacitor is able to store energy with redox reaction, not simply depends on the adsorption of cations and anions in EDLC.[25] This energy storage mechanism is similar to batteries, during charging/discharging process of

device, reversible redox reaction happens on the surface of electrode materials[26]. However, it's important to note that this increase in energy density often comes with a trade-off in the form of reduced power density. This decrease in power density is a consequence of the more complex and time-consuming redox reactions as compared to the simpler ion adsorption processes in EDLCs. As a result, while electrochemical supercapacitors offer enhanced energy capacity, they may not be able to deliver energy as quickly as their EDLC counterparts, impacting their suitability for applications requiring rapid power delivery.

1.2.2 Electrochemical supercapacitor with conducting polymer

For electrochemical supercapacitors, the widely used active materials include metal oxides, conductive materials, two dimensional (2D) materials, etc.[27,28] Metal oxides and 2D materials, often comprising transition metals, are typically associated with higher costs and environmental concerns. In contrast, conductive polymers have emerged as a more sustainable and economical alternative, due to their low cost, high conductivity, and adjustable potential windows.[29] As showed in Figure 1.8, commercial conductive polymers, like PEDOT, PANI, PT, and PPy, *etc*. have different functional groups[30]. By fine-tuning these groups, conductive polymers can be engineered to be either n-doped or p-doped, thereby operating across different potential ranges.[30] This versatility allows for the customization of the polymer's electrochemical properties for specific requirements. Such advancements in polymer chemistry hold the potential to revolutionize the use of conductive polymers in electrochemical supercapacitors, offering a more cost-effective, environmentally friendly, and versatile solution for energy storage in IoT technology.

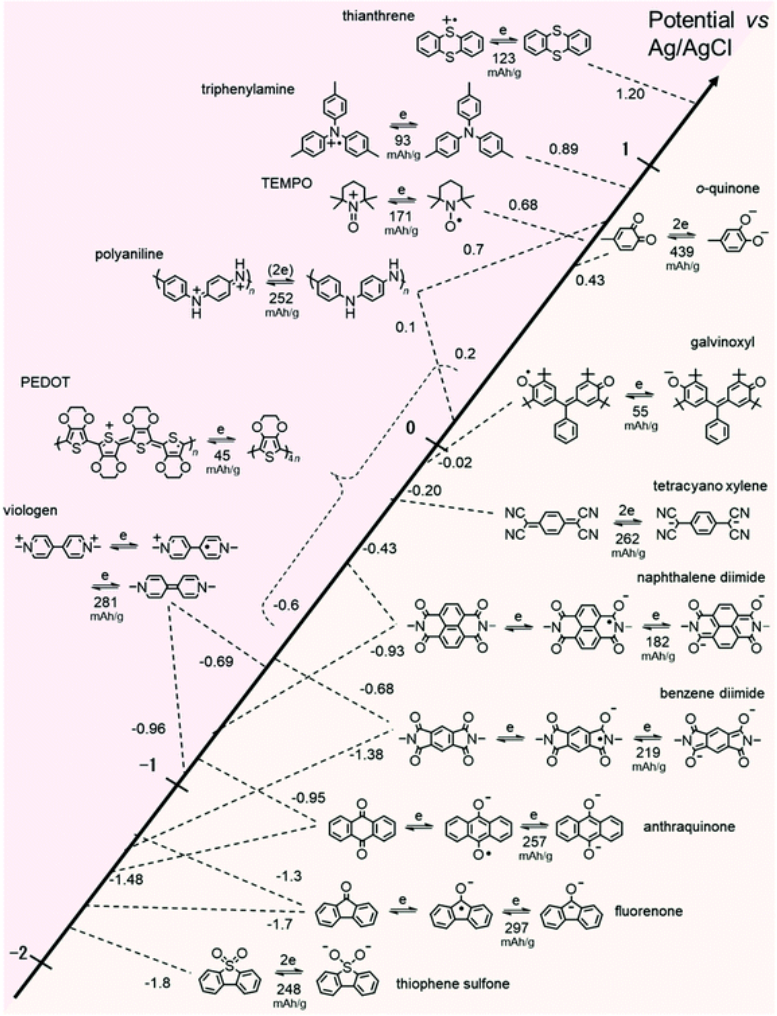

Figure 1.8 Typical redox couples involving organic molecules together with their corresponding redox potentials.[30]

One effective design rule is to combine the donor functional group and acceptor functional group together to create donor-acceptor conjugated polymer (Figure 1.9)[31,32]. So the polymer can inject electrons into the acceptor and extract electrons from the donor functional group. The resultant donor-acceptor polymers possess a unique dual functionality, allowing them to operate as both n-doped and p-doped polymers. This dual doping capability significantly enhances the versatility of these polymers. When incorporated into suitable electrolytes, the potential window of donor-acceptor polymers can be substantially expanded. This broadened potential range makes

them particularly suitable for a wide array of electrochemical applications[33]. Meanwhile, the electrochemical properties of donor-acceptor polymer can be fine-tuned by changing the structure of either donor or acceptor functional group.[34] Such modifications allow for precise control over the polymer's conductivity, stability, and energy storage capabilities. The ability to tailor these properties opens up new possibilities for creating highly efficient and adaptable materials, paving the way for innovative applications in various technological fields, particularly in the development of advanced materials for IoT devices.

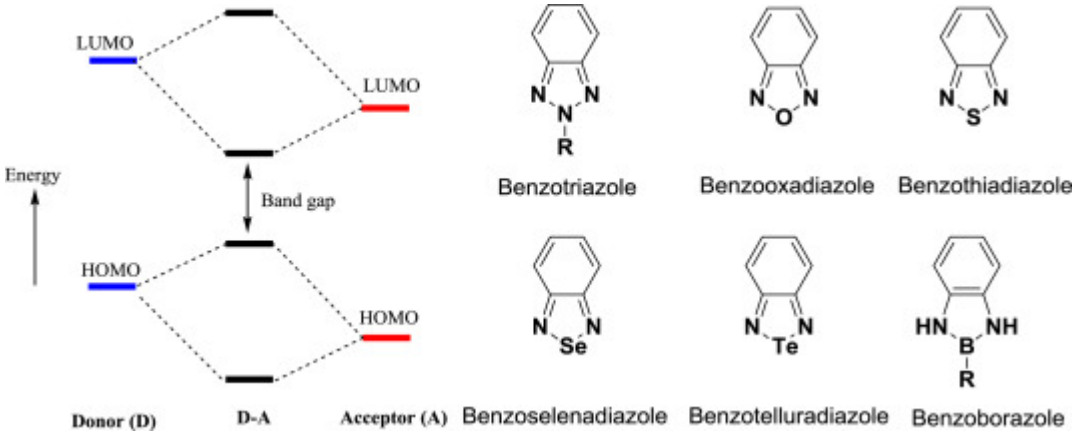

Figure 1.9 (left) Donor-Acceptor effect; (right) Different benzazoles used acceptor units.[34]

1.2.3 Strategies to Optimize the Performance of Supercapacitors

Beyond introducing new energy storage mechanism and novel electrode materials, the electrochemical kinetics and energy density of supercapacitors can be improved through some modification and design considerations.[35] As showed in the Figure 1.10,[36] a comparative analysis of different surface treatments on current collector of active materials, stainless steel was conducted to show that the interface between current collector and active materials played an essential role for the device kinetics. Compared to polished stainless steel, roughened stainless-steel surface exhibits a reduced interfacial resistance with the active materials, as indicated by the smaller semi-circle region in the electrochemical impedance spectroscopy (EIS) curve. This

reduction in resistance is critical for enhancing the charge transfer and electrochemical kinetics of supercapacitor. Further performance enhancement can be observed when a layer of gold coated onto the stainless steel. This modification eliminates the remaining interfacial resistance, thus further enhanced the electrochemical kinetics of the device. This clear evidence showed the important role of surface modifications and interface design in the overall performance of supercapacitors.

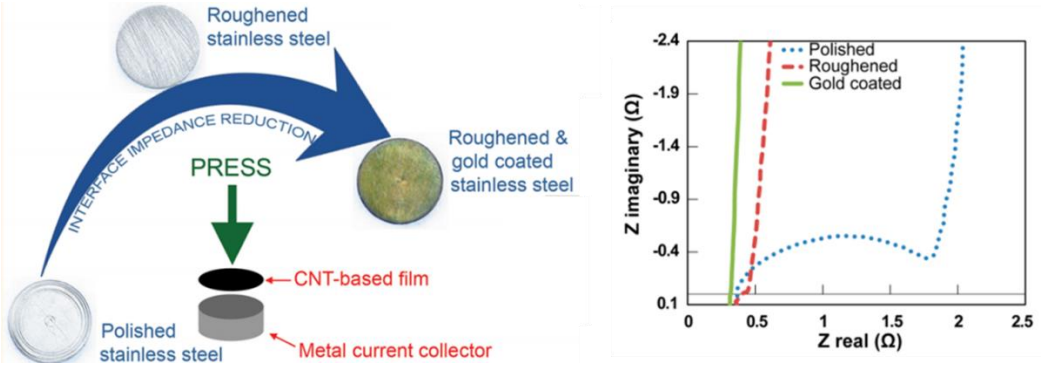

Figure 1.10. Influence of current collector surface modification on supercapacitor performance.[36]

The morphology of active materials is another critical factor that determines the electrode kinetics for supercapacitors.[37,38] As depicted in Figure 1.11a, the vertically aligned graphene sheets on the surface of current collector exemplifies this concept. This design shortens the diffusion path of the electrolyte within the active materials, thereby enhances the electrochemical kinetics of device. As to the conductive polymer-based electrodes, electrode morphology control is even more effective since a dense film structure impedes electrolyte diffusion. By introducing porous structures into the polymer layer, deeper electrolyte penetration in the active materials became feasible, consequently enlarging the electrode/electrolyte interface and reducing the diffusion distance for the electrolyte.[38] This architectural adjustment significantly boosts the electrochemical kinetics of the polymer materials. Additionally, similar kinetic improvements can be achieved by creating holes on the surface of 2D materials.[35] This approach has the same benefits provided by

porous structures, shorten the diffusion distance of electrolyte and facilitate electrolyte access and ion transport within the electrode. All of these methods were able to help electrochemical supercapacitor to operate at higher power density while maintaining the same or even higher energy density.

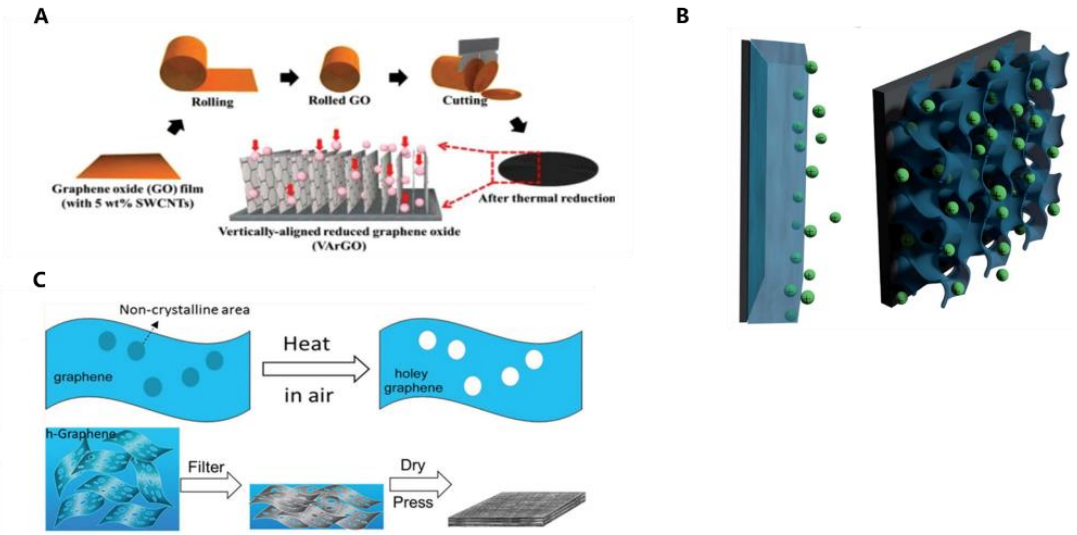

Figure 1.11. Influence of electrode morphology on supercapacitor performance.[37,38]

Another important performance parameter is the energy density of the whole device. Since the energy density of the supercapacitors has a square relationship with the potential window ($E=0.5CU^2$)[39], extending the potential window of supercapacitors become a straight forward method to enhance the energy density of active materials and the whole device. To achieve it, the determining factors of potential windows should be clarified. As showed in the Figure 1.12, the maximum available potential window of the device was determined by the decomposition reaction of solvent (*e.g.* for aqueous electrolyte, determined by the hydrogen evolution reaction and oxygen evolution reaction of water).[40] The practical potential range of supercapacitors was further limited by the operating range of the active materials.[27,41] So employing electrolyte with wider decomposition potential range is the most straight forward method to extend the working potential

range of the device.[42] For aqueous electrolyte, concentrated electrolyte can decrease the content of water inside the electrolyte, thus extending the potential window of electrolyte to even higher than 2 V. Of course, selecting organic electrolyte (propylene carbonate and acetonitrile, *etc*.) can also extend the potential window of device to even higher than 3 V directly.[43]

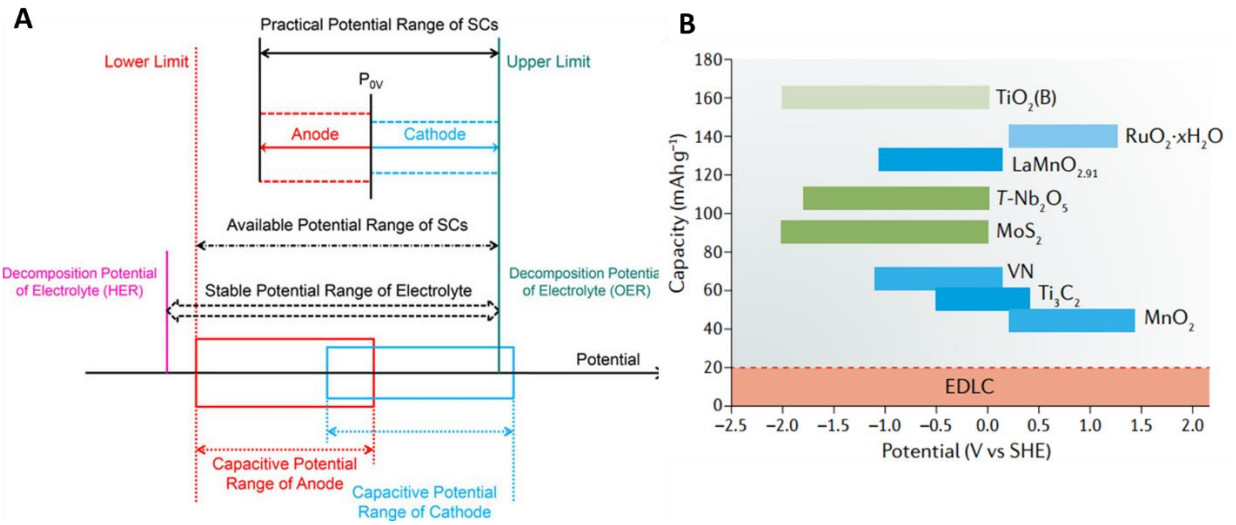

Figure 1.12. (a) Determining factors of potential window for supercapacitor devices.[40] (b) Capacity and potential window of some Electrode materials for supercapacitors.[27]

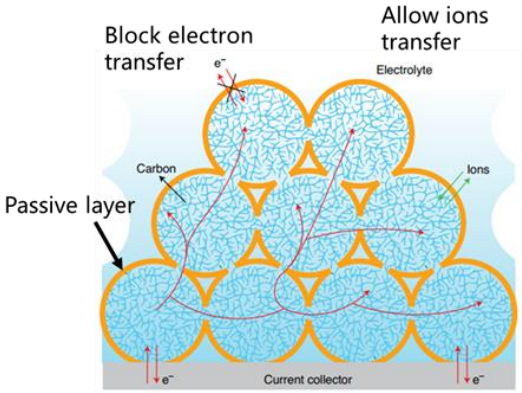

Figure 1.13. Inert coating layer on the surface of electrode for wider operating window.[44]

As discussed in previous section, the internal operating windows of active materials can be tuned by using donor-acceptor conjugated polymers. Beyond this method, surface modification of active materials is also an effective method. As illustrated in Figure 1.13, an electrochemical

inertly layer was coated on the surface of active materials. This layer decreased the interface area between active materials and electrolyte, thus made the stability of electrode materials become better.

Another strategy to enhance the potential window is to use new device configurational battery-type anode in the assembly of metal ion supercapacitors.[45] Figure 1.14 demonstrates a typical Li-ion capacitor configuration[44], employing graphite as the anode and activated carbon (AC) as the cathode. The graphite anode contributes to a broader operating window and higher gravimetric capacity, while the AC cathode offers high power density and extended cycling life. Consequently, this design enables the device to operate within a 4.2 V potential window, significantly surpassing the 2.7 V potential window of conventional supercapacitors.

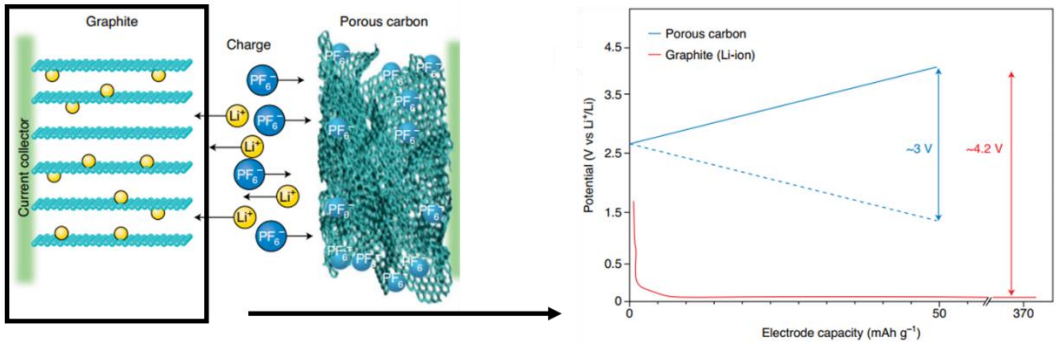

Figure 1.14. Structural of typical Li-ion capacitor and the working voltage of their cathode and anode side.[44]

1.3 Device Design of Electrochemical Supercapacitors for IoT Devices

1.3.1 Introduction of Micro-supercapacitors

As discussed in the previous sections, the power supplies of self-powered IoT devices are intermittent and unpredictable nature, and most of IoT sensors are small and integrated on integrated circuit. So, a high-performance miniaturized electrochemical storage device that is able to store collected energies then output a stable power is highly demand. Micro-supercapacitors

(MSCs, Figure 1.15) utilized EDLC or electrochemical capacitance materials mechanism to store charges on the surface of electrode material, This ensure MSCs high-power density, long cycling life, and short response time, thus becoming a promising candidate for energy storage unit of self-powered electronics.[11]

Figure 1.15 showed two typical configurations of MSCs: stacked configuration and planar configuration. In both configuration, the practical applications of MSCs are limited by their low areal capacitance (C_A) and energy density[11]. One solution is to increase the areal loading of active materials [46,47], but the fabricated thick electrodes limit the diffusion kinetics of electrolyte during the charging/discharging process, thus lowering the power density of MSCs[46]. Another promising method is to utilize pseudo-capacitance materials (*e.g.* conductive polymer[29], metal oxide[48], and MXenes[49], *etc.*) as electrode materials. Their high specific capacitance allows a high C_A with a thinner electrode thickness than EDLC electrodes. Unfortunately, due to the electrolysis of electrolyte and side reactions of electrode, the operating potential window of pseudo-capacitance materials is normally smaller than 1.8 V[2726], seriously limiting the areal energy density (E_A). So electrodes with high C_A and potential window, excellent electrochemical kinetics are key factors to enhance the performance of MSCs.

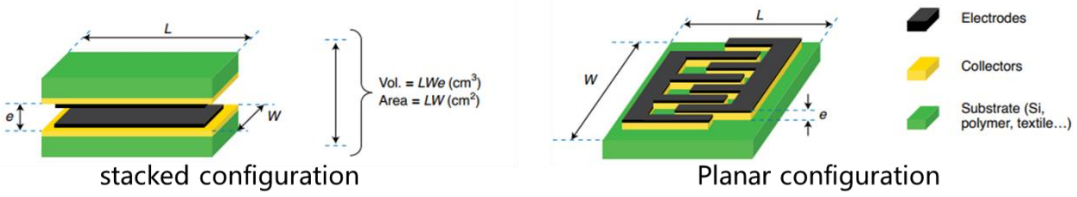

Figure 1.15. Two typical configurations of micro-supercapacitors: stacked configuration and planar configuration.[44]

1.3.2 Introduction of Multifunctional Supercapacitors

Supercapacitors, beyond their primary role in energy storage, can simultaneously perform a variety of tasks, leading to the emergence of multifunctional supercapacitors.[50] This field

represents a cross-disciplinary synergy encompassing materials science, physics, chemistry, and extends into mechanical, electronic, and biomedical engineering, among others.[50] After more than a decade of dedicated research, supercapacitors have been developed with robust mechanical strength, thermal efficiency, electronic functionality, photodetection capabilities, and energy harvesting features. These advancements are achieved through the careful selection of electrode materials and cell configurations, tailored to specific application scenarios.

Figure 1.16a presents a typical example of multifunctional supercapacitors, structural supercapacitors, which are designed to offer both energy storage capabilities and mechanical strength.[51,52] In this design, carbon fibers and glass fibers are employed as the electrode and separator, respectively, to replace conventional metal foils and cellulose paper due to their high modulus. To further enhance flexural strength, solid-state electrolytes have been employed to replace the typical liquid electrolytes. By altering the materials system and employing a novel fabrication method (Figure 1.16b, vacuum-assisted resin transfer molding process), structural supercapacitors have been successfully developed and demo various applications.[49]

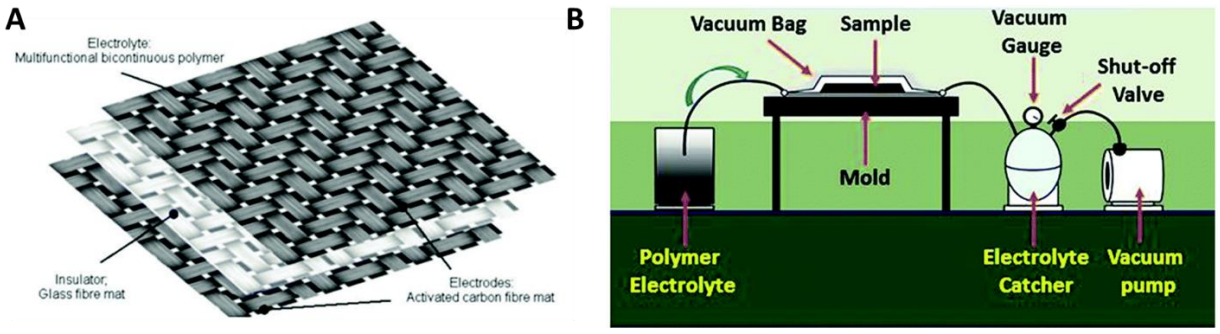

Figure 1.16. (a) Setup of typical structural supercapacitors.[52] (b) Setup of vacuum-assisted resin transfer molding process for structural supercapacitor fabrication.[51]

For conductive polymer-based electrode materials, here is also a special type of multifunctional supercapacitors: electrochromic devices (Figure 1.17)[53,54]. They have a unique phenomenon where the optical properties or color of the electrode materials can be altered by controlling the external

potential. This feature finds extensive applications in color-switchable windows and display screens. To fabricate electrochromic devices, replacing the current collector and separator with transparent materials and selecting active materials that optical properties are tunable through voltage are the basic requirements. The widely used electrochromic electrode materials are mainly transition metal oxides, such as WO_3, MoO_3, *etc*.[53] However, these inorganic materials-based devices have several drawbacks including single color change, expensive materials, and a slow response speed. Conductive polymers (CPs), as we discussed in previous sections, have tunable bandgap by changing their functional groups and even synthesizing conjugated polymers. Together with their high conductivity, devices with fast response speed and wide color change range are expected.

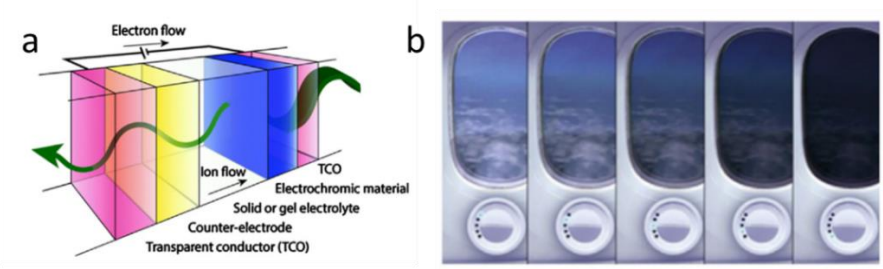

Figure 1.17. (a) Typical configuration of electrochromic devices.[53] (b) Application of electrochromic devices in color-switchable windows. [53]

CHAPTER 2: ULTRAFAST AND HIGH-ENERGY MICRO-SUPERCAPACITORS BASED ON OPEN-SHELL POLYMER-GRAPHENE COMPOSITES

2.1 Design of Supercapacitors with High Power Density

The ultimate goal of electrochemical energy storage technologies is to realize high power and energy density along with stability that spans thousands of charge-discharge cycles [26,27,44]. Current devices are hampered by trade-offs in their power, energy, and cycling stability. For example, the volumetric energy density of batteries exceeds that of electrochemical supercapacitors and electrolytic capacitors; however, the device power rating, frequency response, and cycle life follow an opposite trend. Currently most batteries and supercapacitors operate below 1 Hz, with slow kinetics that impede their application in alternating current (AC) circuits. A long-standing goal for supercapacitors is to synergistically increase the energy density towards the level achieved by batteries, and concurrently raise the power delivery to match electrolytic capacitors that operate at a typical AC line frequency of 60 Hz [55,56]. If these targets are met, supercapacitors will enable compact power circuits that are not presently achievable owing to the bulky size and weight of electrolytic capacitors. The realization of these supercapacitors will also provide energy storage platforms with much longer cycle lives than batteries, thereby reducing the replacement and maintenance costs of sensor networks [11,57].

Research on supercapacitors has built upon hierarchical electrode structures [46–49,58–61] that promote increases to the device capacitance *C* and potential window *V*, since the energy capacity follows from $E = CU^2/2$. One approach to raise the electrode capacitance is to increase the areal loading of active materials; however thicker electrodes are generally restricted by slow charge transfer kinetics which reduce the overall power density within devices. Another method to improve performance is to use redox-active materials such as metal oxides, MXenes, and

conducting polymers that raise *C*. However, redox electrodes comprised of these materials remain constrained to a potential window ≤ 2 V and exhibit lower cycle lifetimes than electric double layer capacitors [26,27]. Thus, new materials remain critical to achieve increased energy, power, and lifetime targets.

In this chapter, we describe a hierarchically structured electrode comprised of a novel open-shell redox polymer and reduced graphene oxide (rGO) [62–64] that offers state-of-the-art capacitance, an extended potential window, and excellent kinetics and cycle life. Traditionally, π-conjugated materials such as small molecules, polymers, and particularly open-shell species utilized for energy storage applications are unstable on account of the highly localized nature of reduced species and localized radical sites [65,66]. Recently, new classes of donor-acceptor (DA) conjugated polymers [33,67] have been reported that demonstrate significant electronic correlations within the π-conjugated backbone, very narrow bandgaps, open-shell ground states, and intrinsic electrical conductivity. The high degree of electronic coherence promotes extensive delocalization, which serves to thermodynamically stabilize unpaired spins and the resultant charged species. When applied in supercapacitors, this new class of redox-active polymer enabled an increase in the potential window to 3 V, but remained limited in specific capacitance on account of inert solubilizing side chains that are required for solution-processing. This structural feature reduced the energy density and power output of thick films in a similar manner to other kinetically-limited materials.

To overcome these drawbacks, we demonstrate an electro-polymerization methodology that proceeds directly from the constituent monomers and results in open-shell DA conjugated polymers that are unencumbered by inert solubilizing groups. The open-shell polymers are co-deposited with reduced graphene oxide (rGO) to form porous, conductive scaffolds that result in

micron thick electrodes with fast kinetics. The electro-polymerization process is facile, occurs at room temperature, and is amenable to direct integration on silicon chips, so as to enable the fabrication of micro-supercapacitors on integrated circuits for system miniaturization. The process is scalable to large-areas enabling high-capacity devices.

Variations in the open-shell polymer-rGO composites were examined to decouple the trade-off between device power and energy density. We further analyzed the impact of compositional changes on electrochemical kinetics through equivalent circuit models of the electrodes. Characterization of the devices over 100,000 charge-discharge cycles demonstrated exceptional stability, on account of the unique electronic delocalization of redox states and flexible mechanical framework that tolerated expansion and contraction during redox cycling. The compact, flexible supercapacitors operated at 120 Hz, suitable for ac filtering[56,68] and are also compatible with pulse and fast charging, which demonstrates their potential to replace bulky electrolytic capacitors in power electronics. In another use case, we integrated the composite device as the sole energy storage component within a wireless energy harvesting system, which enabled autonomous short-range electronics [10,69]. This report demonstrates a new generation of redox supercapacitors that enable ultrafast, energy-dense storage with unprecedented cycling durability, and which offers practical utility within emerging microelectronic technologies.

2.2 Electrode Materials Preparation

2.2.1 Synthesis of QxTh Monomer

The chemical reaction of QxTh monomer synthesis was showed in the Figure 2.1. All manipulations of air and/or moisture sensitive compounds were performed handled under an inert nitrogen atmosphere using standard glovebox and Schlenk techniques. 1,2-di(thiophen-2-yl)ethane-1,2-dione (0.650 g, 2.92 mmol) was added to a slurry of 4,7-di(thiophen-2-

yl)benzo[c][1,2,5]thiadiazole-5,6-diamine (0.650 g, 1.97 mmol) in acetic acid (50 mL). The formed mixture was stirred at 75 °C for 24 h and followed by stirring at room temperature for 2 h and then partitioned between chloroform (100 mL) and water (150 mL). The organic layer was separated, washed with water (3 × 100 mL), dried over anhydrous $MgSO_4$, and evaporated to dryness. The resulting residue was purified on a silica gel column and eluted with methylene chloride: hexanes (2:3), after which the solvents were removed under reduced pressure to afford 4,6,7,9-tetra(thiophen-2-yl)-[1,2,5]thiadiazolo[3,4-g]quinoxaline as a dark blue solid (0.785 g, 1.53 mmol, 78%). ^{1}H NMR (600 MHz, chloroform-*d*): δ 8.90 (d, *J* = 3.8 Hz, 2H), 7.70 (d, *J* = 5.1 Hz, 2H), 7.62 (d, *J* = 5.0 Hz, 2H), 7.56 (d, *J* = 3.7 Hz, 2H), 7.32 (t, *J* = 4.5 Hz, 2H), 7.08 (t, *J* = 4.4 Hz, 2H). ^{13}C NMR (151 MHz, chloroform-*d*): δ 152.19, 146.26, 141.77, 135.83, 134.37, 133.38, 131.68, 131.28, 131.04, 127.72, 126.98, 121.03. HRMS (ESI-TOF) exact mass calculated for $C_{24}H_{12}N_4S_5$: m/z 516.9743 $[M+H]^+$; found 516.9744.

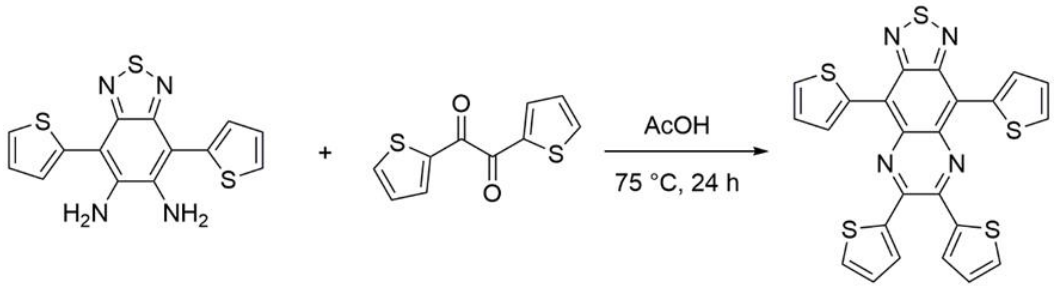

Figure 2.1. Chemical reaction for the synthesis of QxTh monomer.

2.2.2 Electro-Polymerization Synthesis of QxTh Polymer

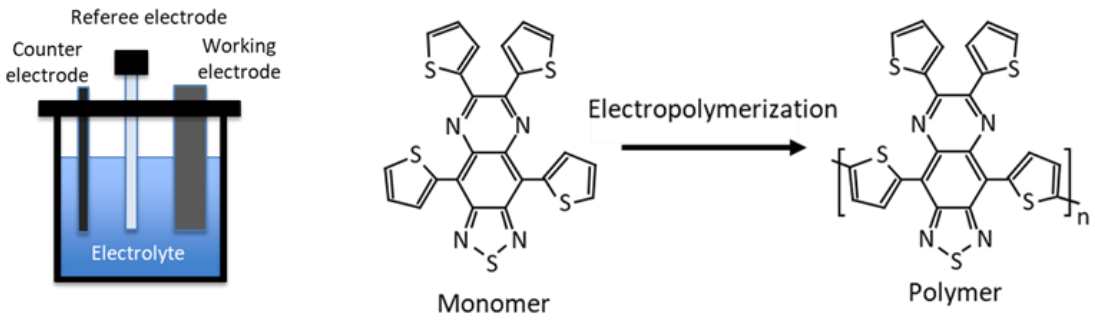

Figure 2.2. Scheme and Chemical reaction for the electro-polymerization of the QxTh polymer.

A In prior work [33,70–73], redox polymers were synthesized and purified in preparation for a separate deposition step, thus solubilizing groups were required to enable re-dissolution for coating onto substrates. The inert solubilizing groups add mass but do not contribute to the redox activities, lowering the specific capacitance of the materials. This motivated our development of poly(4,6,7,9-tetra(thiophen-2-yl)-[1,2,5]thiadiazolo[3,4-*g*]quinoxaline, an open-shell polymer comprised of alternating bithiophene donors and thiophene substituted thiadiazoloquinoxaline acceptors that could be synthesized using an electro-polymerization approach. As shown in Figure 2.2, the polymerization was carried out by suspending graphite foil electrodes in a mixed solvent of dichloromethane and propylene carbonate containing the monomer 4,6,7,9-tetra(thiophen-2-yl)-[1,2,5]thiadiazolo[3,4-*g*]quinoxaline (QxTh) and 0.1 M tetrabutylammonium hexafluorophosphate ($TBAPF_6$). The electro-polymerized films were used as grown without additional purification steps. The polymer demonstrated good adhesion to the graphite foil that served as the current collector in supercapacitor devices. The application of potentials higher than 0.5 V (versus Ag/Ag^+) resulted in the growth and deposition of polymer on the graphite foil.

2.2.3 Synthesis of QxTh-rGO Composite Electrode

The electrical conductivity and ionic conductivity of pure polymer-based electrode is always one of the biggest limiting factors for the applications in supercapacitors, especially when high power density is needed. To solve it, combing with conductive materials has been demoed as a good solution for these problems. Here rGO was selected, and mixed with QxTh monomer. QxTh-rGO composite was synthesized through a similar electro-polymerization method to the QxTh polymer (Figure 2.3).

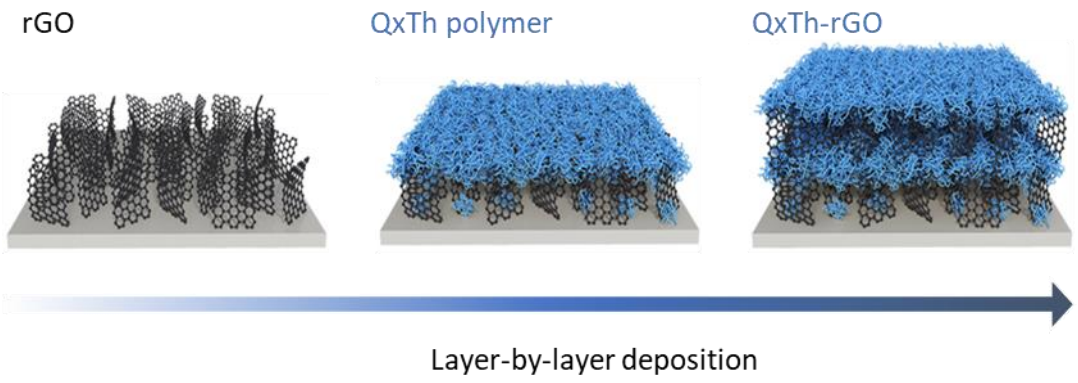

Figure 2.3. Schematics of the electro-polymerization process to deposit QxTh and rGO alternately.

The cathodic electro-polymerization process was conducted in a three-electrode configuration, with a graphite foil (conductivity: ~16,000 S cm^{-1}, thickness: 16 μm, from Emitac New Material Technology) as the working electrode, an activated carbon cloth for the counter electrode, and an Ag/Ag^{+} reference electrode. The process was conducted inside a nitrogen filled glove box. The chemicals purchased from Sigma-Aldrich were used as received. The synthetic procedure for the QxTh monomers is in shown in the supporting information.[33]. For the electro-deposition of QxTh, a mixed solvent of dichloromethane (DCM) and propylene carbonate (PC) in a 2:3 volume ratio was used to dissolve QxTh to give a concentration of 1 mg mL^{-1} and tetrabutylammonium hexafluorophosphate ($TBAPF_6$) concentration of 0.1 M. The applied voltage on the working electrode was cyclically scanned between –0.5 V and 0.8 V (versus Ag/Ag^{+}) at 50 mV s^{-1} to polymerize the monomers (Figure 2.4). For the deposition of rGO, either 1 or 5 mg mL^{-1} GO prepared by a modified Hummers' method[74] was added to the same electrolyte as used for QxTh, and the deposition potential was held at –2 V for 5 s. The deposition proceeded by repeating the deposition voltage waveform. After deposition, the electrodes were annealed at 200 °C for 30 min and then scanned between –0.5 V and 1 V in the electrolyte (0.1 M $TBAPF_6$ in DCM:PC) for 20 cycles to eliminate residual monomers in the films.

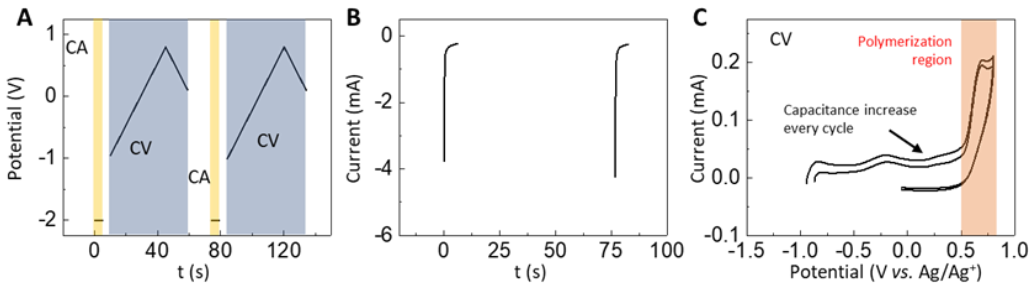

Figure 2.4. (a) Constant potential and cathodic electro-polymerization process at a scan rate of 50 mV s^{-1} for QxTh-rGO electrode deposition. (b) The current change with time for the constant potential process in (a). (c) The cathodic electro-polymerization process in (a).

To further understand the polymer properties of QxTh-rGO polymer, MALDI-TOF MS was conducted and measured with Bruker Autoflex Max MALDI-TOFMS instrument. The sinapinic acid (SA) matrix was prepared in water/acetonitrile (1:1) with 0.1% trifluoroacetic acid. The polymer/composite powder sample was then dispersed in dichloromethane, vortexed, before mixing with the SA matrix (5 µL sample mixed with 10 µL matrix), followed by spotting the mixture on the MALDI plate. After air drying, the sample plate was loaded for MALDI-TOFMS analysis. Measurements by matrix-assisted laser desorption ionization time of flight mass spectrometry (MALDI-TOF MS, Figure 2.5) pointed to the QxTh polymer. MALDI-TOF indicated the formation of polymers with up to 12 repeat units (n) using these conditions, indicating the formation of polymers with long conjugation lengths.

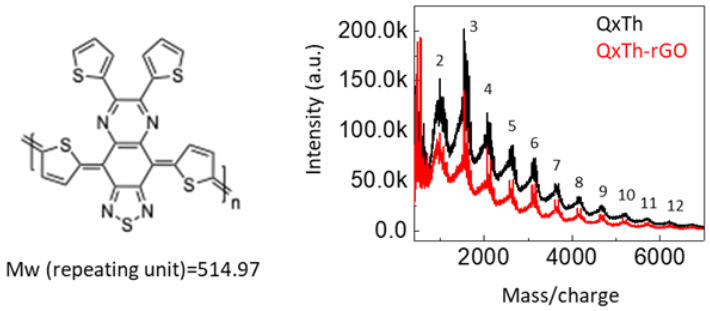

Figure 2.5. Matrix-assisted laser desorption ionization time of flight mass spectrometry (MALDI-TOF MS) of QxTh polymer and QxTh-rGO composite powders. The formed polymer powder included polymer chain length from 2 to 12.

2.3 Electrochemical Performance of Electrode Materials

2.3.1 Electrochemical Performance of QxTh Polymer Electrode

The electro-polymerization process of QxTh polymer and QxTh-rGO composite electrode eliminated the need for inert solubilizing groups, thereby increasing the specific capacitance of the polymeric material. Cyclic voltammetry (CV) (Figure 2.6) was consistent with this point, demonstrating a specific capacitance of 297.6 F g^{-1} between –0.5 V to –2 V (versus Ag/Ag^{+}), which is a 200% increase over previous generations of n-dopable conjugated polymers [33,70,71]. The CV in Figure 2.6C also showed that the polymer was stable to –2.2 V (versus Ag/Ag^{+}), a noteworthy attribute since the majority of n-type polymers are not stable at these low potentials [19,29,75]. Our polymer, comprised of alternating donor and acceptor heterocycles, promotes a narrow bandgap significant internal charge transfer characteristic, and extended delocalization of unpaired electrons and redox states, resulting in enhanced stability. Overall, the oxidation and reduction reactions of the polymer were reversible over a wide potential window of 3 V, facilitating high voltage storage that increased the energy densities of our supercapacitors.

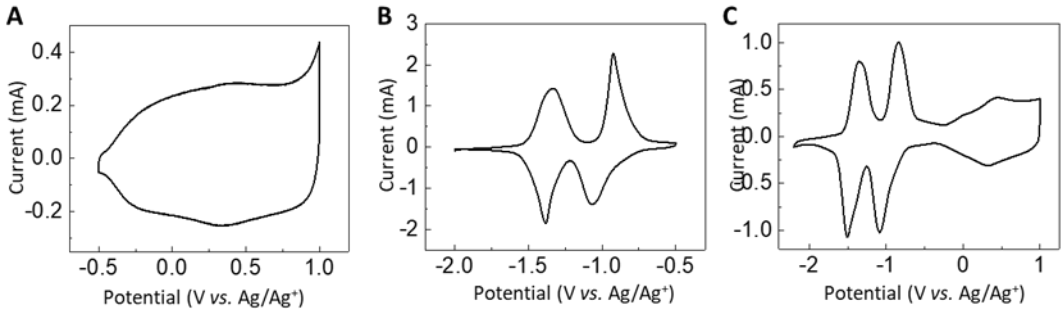

Figure 2.6. The scan rate was at 100 mV s^{-1}. Specific capacitance determination for QxTh working between (a) -0.5 and 1 V; (b) -2 V and -0.5 V; and (c) -2 and 1 V. The mass of QxTh was 0.15 mg, thus the calculated specific capacitances were (a) 143.3 F g^{-1}; (b) 297.6 F g^{-1}, and (c) 238.6 F g^{-1}.

Most pseudo-capacitive devices operate within a potential window smaller than 2 V. A primary reason is that many require aqueous electrolytes, so in which the water-splitting reaction limits the

operational voltage. However, electrode degradation is also an important limiting factor, since most pseudo-capacitive materials provide high redox capacitance only within a small potential window. Their potential windows are normally between –1 V to 1 V vs. Ag/Ag^+ reference, so as to limit irreversible reactions and severe degradation of the electrodes. There is a lack of redox materials that are stable in more negative potential range to utilize the full stability window of organic electrolytes, which can be generally safe to operate down to –2 V relative to Ag/Ag^+. Our QxTh-rGO redox composite fills in this gap, providing stable n-dopable electrodes that can be used as anodes together with other cathodes.

The polymer showed linear current–voltage (*I*–*V*) characteristics with conductivity σ_{RT} ~10^{-4} S cm^{-1} (Figure 2.7a). The transport properties can be associated with the narrow bandgap of the polymer, which promote a low energetic barrier for thermal excitation of free carriers and extensive delocalization[67]. At room temperature, continuous wave electron paramagnetic resonance (EPR) spectroscopy showed a broad single line 2–5 Gauss wide with a *g*-factor (*g*) of 2.0035 (Figure 2.7b), indicative of the open-shell nature of the polymer. Density functional theory (DFT) calculations at the unrestricted (U)B3LYP/6-31G** level of theory were carried out on oligomers with an increasing number of repeat units and show a rapid transition to an open-shell ground state at chain lengths of n = 6. A diradical character index (y) of 0.09 and 0.039 was obtained for the n = 6 and 8 oligomers respectively and accounts for the signal and spin-concentration obtained by EPR. Molecular electrostatic surface potential (MESP) plots of the n = 8 oligomer in the neutral, oxidized and reduced states ($+1e^-$ and $+2e^-$, respectively) are shown in Figure 2.7c.

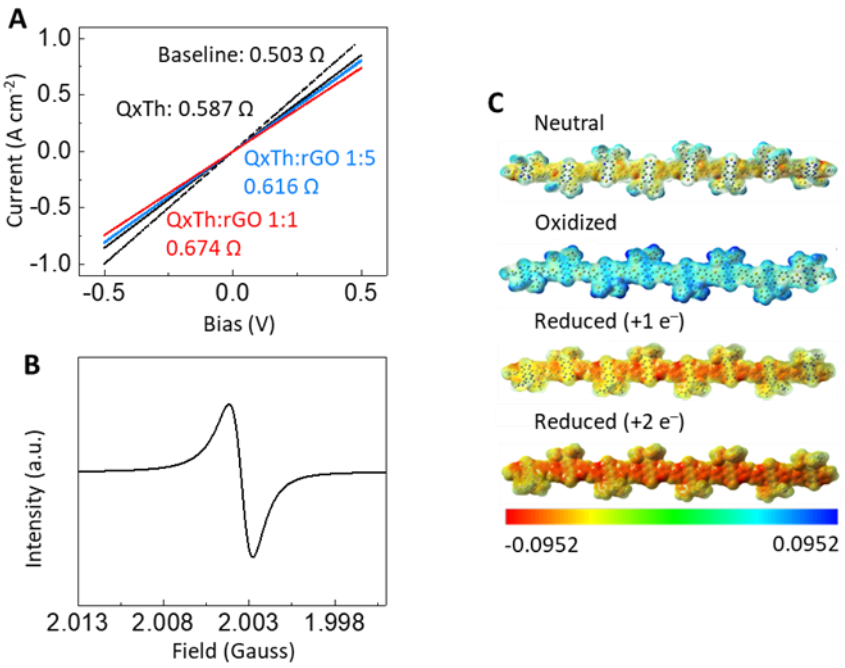

Figure 2.7. (a) Conductivity measurement of QxTh polymer film on graphite foil substrate. (b) Electron paramagnetic resonance results of QxTh powder. (c) Molecular electrostatic potential (MEP) surface of the polymer in the neutral, oxidized and reduced (+1e and +2e-) states at n = 8.

These calculations demonstrate that the spin density is distributed throughout the conjugated backbone in the neutral state. When the polymer is oxidized or reduced, charge density is delocalized throughout the π-conjugated backbone, which contrasts with other radical redox polymers where unpaired charge is located on specific radical functional groups. Furthermore, the addition or removal of an electron from the polymer serves to enhance the planarity of the π-conjugated skeleton, and this high degree of charge delocalization is likely to enhance the stability of different redox states.

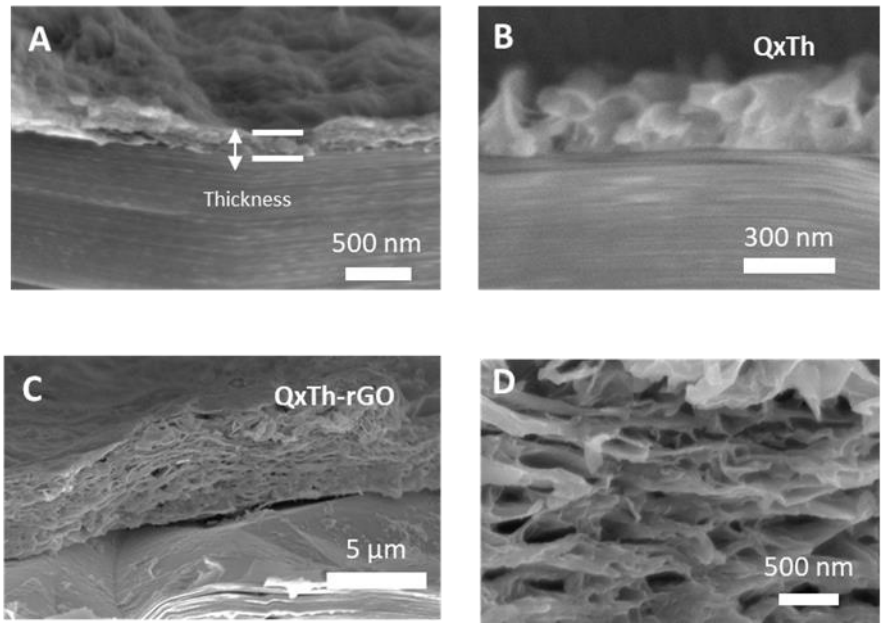

Figure 2.8. (a) SEM image of 1:5 film deposited with 10 cycles. (b) SEM images of QxTh:rGO 1:5 film deposited with 1600 cycles before redox cycling. (c) and (d) After 100k redox cycles.

Cross-sectional scanning electron microscopy (SEM) images of the electro-polymerized polymer film display a porous morphology (Figure 2.8a, b) that is advantageous for electrolyte penetration. However, as the polymer thickness was increased, the film became more resistive limiting further growth. To retain the porous structure while improving the overall conductivity of the electrodes, we adjusted the electro-deposition process to incorporate rGO as the conductive matrix. This sequential deposition of the polymer and rGO resulted in a porous composite (Figure 2.8c) in which the polymer contributes to the high specific capacitance, while rGO provided highly conductive pathways, overcoming the restrictions imposed by the electrical resistance of the neat polymer film. The deposition was carried out up to 3000 cycles, resulting in a film that is approximately 5µm thick (Figure 2.8c). This electro-polymerization process allows the direct deposition of thick films to increase mass loadings per unit area. Furthermore, the process is scalable in area and the composite could be directly integrated on a large 3 cm × 6 cm graphite foil (Figure 2.9).

Figure 2.9. Photograph of a QxTh:rGO 1:5 film prepared on a graphite foil.

2.3.2 Electrochemical characteristics analyzed with equivalent circuit models

We varied the composition of the electro-deposition solution to examine the effects of the polymer to rGO ratio on electrode properties. Electrodes of different composition were prepared by varying the concentrations of monomer and GO in the polymerization solution at either 1:1 or 1:5. Figure 2.10 shows the increase in electrode areal capacitance with deposition cycles, which demonstrates that adding GO raised the deposition efficiency per cycle. We anticipate that incorporating rGO provided additional nucleation sites for the polymerization process, so larger amounts of polymer were deposited when GO was present in the mixture. The 1:1 and 1:5 composite electrodes were nearly comparable in their capacitance. Changing the amount of rGO incorporated into the polymer-rGO composite minimally yielded only a small effect on the electrode capacitance. The gravimetric capacitance of rGO (typically 80–200 F g^{-1})[76] was smaller than the QxTh polymer (298 F g^{-1}). A large portion of the capacitance contribution was due to redox charge exchange in QxTh, and thus we did not raise the GO concentration beyond the 1:5 ratio to maintain a sufficient amount of QxTh within the composite.

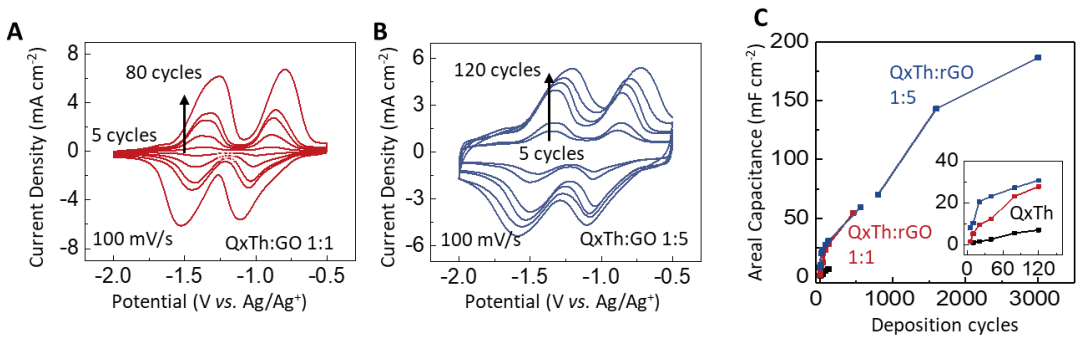

Figure 2.10. CV curves of (a) 1:1 QxTh:GO at 5, 10, 20, 40, 80 deposition cycles; and (b) 1:5 QxTh:GO at 5, 10, 20, 40, 80, 120 deposition cycles. (c) Areal capacitance as a function of deposition cycles.

Using 1:5 polymer:GO ratio, an areal capacitance of 186 mF cm^{-2} (372 F cm^{-3}) was achieved at 3000 deposition cycles which resulted in a 5 μm thick film, while at 1600 deposition cycles the film was 3.15 μm thick with an areal capacitance of 145 mF cm^{-2} (460 F cm^{-3}), as shown in Figure 2.10**.** These areal capacitance values were obtained from CV characteristics of the composite films as a function of deposition cycles, as shown in Figure 2.10 a, b. The change in volumetric capacitance with different film thickness indicated a gradual change in the distribution of active materials. The rate of film growth was reduced with high deposition cycles, with the film thickness increased by only ~2 μm between 1600 and 3000 cycles. Optimization of the conductive network and increasing the deposition voltage are possible avenues to maintain the deposition rate in the future.

Electrodes with a similar areal capacitance of ~10 mF cm^{-2} comprised of neat polymer, 1:1 and 1:5 polymer:GO were selected for comparative studies, and their electrochemical impedance characteristics are shown in Figs. 11a and 11b. The data were fit to an equivalent circuit model (Figure 11b, inset) with the best-fit values listed in Table 2.1. The parameter R_1 represents the electrical resistance of current collectors, and R_i and C_i represent the interfacial resistance and capacitance, respectively, which indicates the barrier for charge-transfer. The Warburg diffusion

element W_1 represents the diffusion-controlled resistance, and Q_1 is the constant phase element that models the non-ideal capacitance of the electrode.

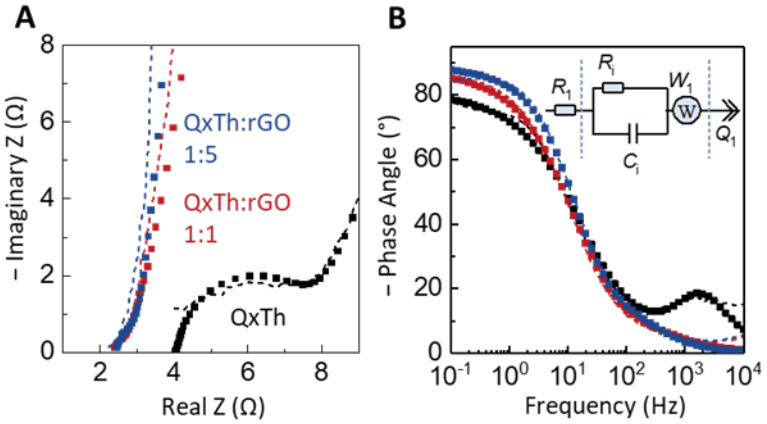

Figure 2.11. (a) EIS of electrodes with an areal capacitance of 10 mF cm^{-2}, biased at -1.5 V versus an Ag/Ag^+ reference. Measurements are shown in solid symbols, while model fits are represented by dashed lines. (b) Phase angle versus logarithm of frequency. Inset: equivalent circuit model used for data fits. The parameter definitions are listed in Table 2.1

Table 2.1. Fit values to the data taken with electrochemical impedance spectroscopy. The equivalent circuit model is shown in Figure 2c. The area of each electrode was 0.56 cm^2. The deposition cycles for each material were chosen to obtain similar capacitance (~10 mF cm^{-2}) across all the samples for comparison, and the fitting errors was < 10%.

	QxTh	1:1 QxTh:rGO	1:5 QxTh:rGO
Deposition cycles	120	20	5
R_1 (Ω)	4.0	2.3	2.4
R_i (Ω)	3.04	0.15	0.34
C_i (mF)	0.04	2.39	2.94
W_1 (mF $s^{-0.5}$)	30.1	8.6	5.2
Q_1 (mF s^{n-1})	2.3	6.1	4.3
n	0.91	0.98	0.99

R_1: resistance of current collectors. R_i: interfacial resistance. C_i: interfacial capacitance. W_1: Warburg diffusion element, with the constant phase angle of 45°. Q_1: constant phase element, with n as the phase angle.

In Figure 2.11a, a prominent difference between the neat polymer and composite electrodes was apparent in the low frequency regime, where the impedance slopes increased upon rGO addition. For the neat polymer electrode, the impedance data showed a section with a phase angle

of 45°, corresponding to W_1. When rGO was incorporated within the electrodes, the W_1 parameters (Table 2.1) became smaller, implying that electrolyte diffusion was more efficient in the composites. The additional surface area imparted by the rGO leads to shorter diffusion distances for the electrolyte ions to counter-balance charges in the composites.

For the electrode comprised solely of polymer, there was a prominent semi-circle region in the impedance plot and a bump in the phase angle at high frequencies above 1 kHz (Figure 2.11b). These characteristics were attributed to interfacial charge-transfer resistance, originating from either insufficient charge collection at the interface between the current collector and the electrode material, or poor charge conduction across the electrode [68]. The features associated with charge-transfer resistance disappeared upon rGO addition; the composite electrodes exhibited R_i values ten times lower than the neat polymer film. Electro-deposition of rGO also modified the surface of the current collectors. Neat polymer films were flat, while composite films are nanostructured with additional surface area serving to improve electrical contacts. The rGO also facilitated improved charge transport from the current collector throughout the bulk of the electrode, as depicted in Figure 2.12.

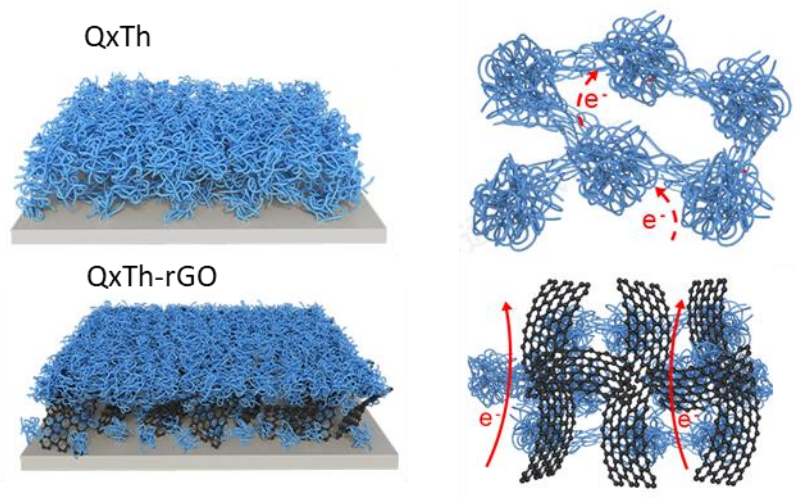

Figure 2.12. Schematics showing the effects of rGO on the interfacial resistance.

In Figure 2.13, the capacitance of the electrodes was monitored over 11,000 galvanostatic charge-discharge (GCD) cycles between –2 to –0.5 V (versus Ag/Ag^{+}) (Figure 2.13). While the capacitance retention was 87.7% for polymer-based electrodes, it was even higher for polymer-rGO electrodes, with 92 % retention for both the 1:1 and 1:5 composites. The cycling stability of the polymer was remarkably better than other *n*-type polymers which all degrade well below 80% well below a few thousand cycles [19,29,70,75,77,78]. The improved stability of the polymer-rGO composite could be attributed to rGO networks that withstand repeated expansion and contraction during cycling, while retaining the conductivity necessary to avoid charge trapping in polymer domains [79].

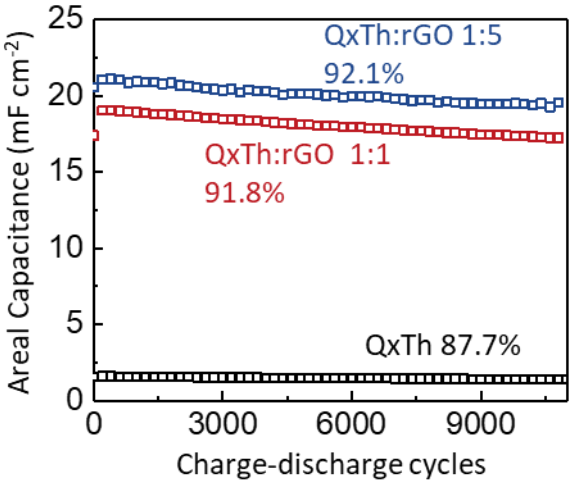

Figure 2.13. Areal capacitance versus charge-discharge cycles. The charging/discharging current density is 5 mA cm^{-2} for the QxTh electrode, and 35 mA cm^{-2} for the QxTh-rGO electrodes.

2.4 Electrochemical Performance Analysis of Supercapacitor Devices

2.4.1 Device Configuration for Supercapacitors

The electrodes fabricated from a 1:5 polymer:GO mixture were used for device fabrication since they displayed the lowest diffusion resistance and the highest cut-off frequency. Supercapacitors were fabricated in either a symmetric or asymmetric configuration as depicted in Figure 2.14. In a

symmetric supercapacitor, the same redox materials were used for both the cathode and the anode, while an asymmetric device used different materials for each electrode. Since each cathode and anode pair should have an equal charge capacity ($Q = C_A V$) to balance electrode utilization, the number of deposition cycles was tuned to match the areal capacitances C_A of the cathode and anode pair in their respective potential windows. Against an Ag/Ag^+ reference, cathodes operated between –0.5 V to 1 V, while the anodes operated between –2 V to –0.5 V. Thus each electrode spanned a 1.5 V range to give a total device voltage of 3 V.

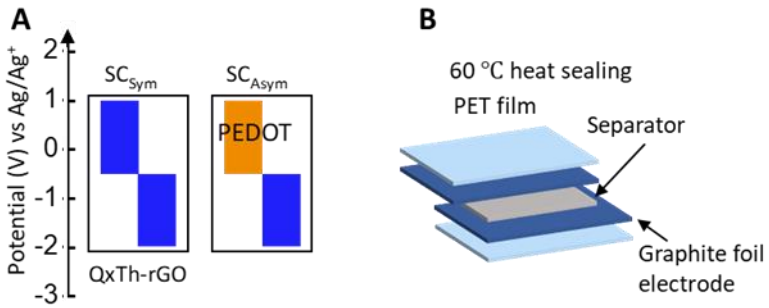

Figure 2.14. (a) Materials of symmetric and asymmetric supercapacitors. (b) Structure of a supercapacitor.

For symmetric supercapacitors, the composite electrodes operating in the cathodic range showed smaller currents and therefore a lower specific capacitance than in the anodic region. To compensate for the reduced specific capacitance, the loading mass of the cathode was increased relative to the anode, so that the resulting capacitance is equal on both electrodes. For asymmetric cells, we replaced the QxTh-rGO in the cathode with PEDOT-rGO composites. As seen in Figure 2.15c, the PEDOT-rGO electrodes showed high stability and a porous structure. Compared to symmetric devices, the asymmetric design allowed for similar loading masses between cathode and anode pairs, which increased the overall charge capacity as evident from the CV characteristics in Figure 2.15.

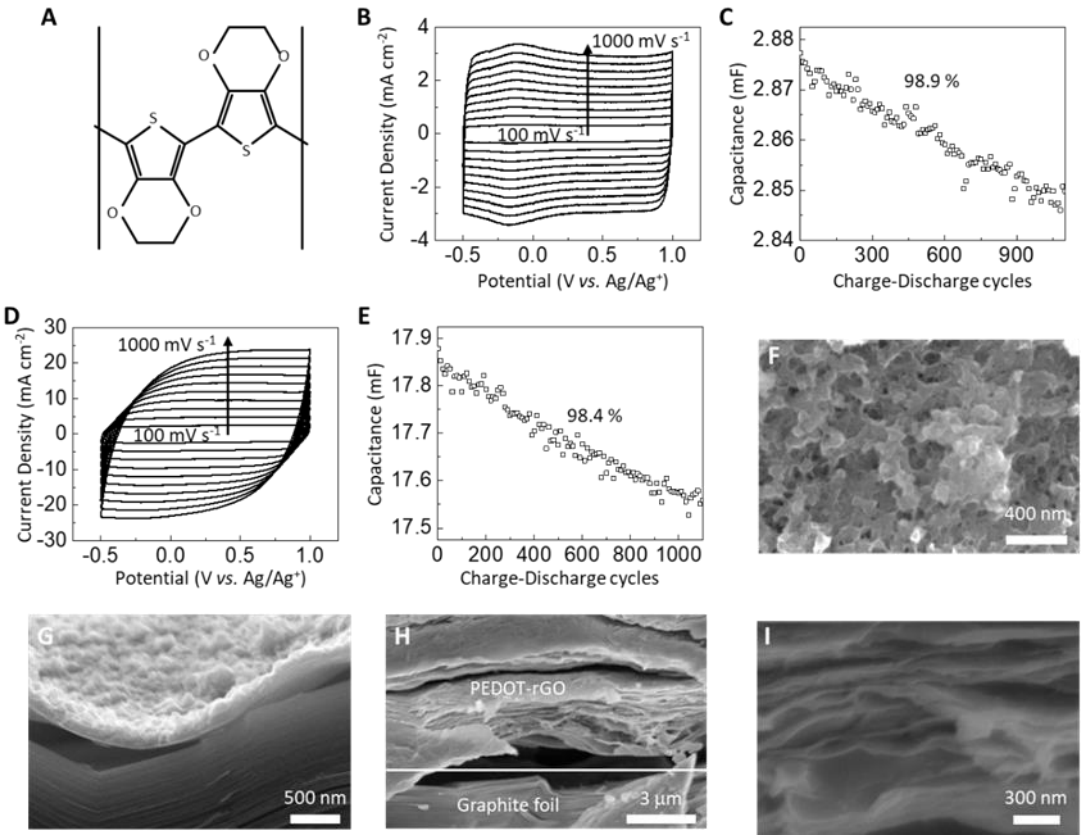

Figure 2.15. (a) Chemical structure of PEDOT. (b) CV curves with scan rate at 100 to 1000 mV s^{-1} in steps of 100 mV s^{-1} increment. (c) Stability of PEDOT electrode. (d) CV curves with scan rate at 100 to 1000 mV s^{-1} in steps of 100 mV s^{-1} increment. (e) Stability of PEDOT-rGO electrode. (f) Top view and (g) side view of PEDOT film. (h) and (i) side view of PEDOT-rGO composite electrodes.

2.4.2 Applications in AC line filter

An immediate need in power electronics is to identify a replacement for aluminum electrolytic capacitors (AECs)[80]. These bulky AECs are one of the most ubiquitous components in electronic devices and represent a major hurdle towards system miniaturization. Supercapacitors readily provide higher specific capacitance than AECs but are limited in their frequency response. A longstanding goal has been the identification of devices sufficient for rectifying 60 Hz AC line signals, which requires a cut-off frequency beyond 120 Hz. As the surface redox sites and open pore structures in our composite electrodes facilitated fast electrolyte ion movement, our supercapacitors could maintain capacitive behaviors to a few hundred Hz. The cut-off frequency,

defined as the frequency when the device phase angle dropped to –45°, was 720 Hz for the asymmetric cell (Figure 2.16), much higher than typical supercapacitors and batteries that operate at a few Hz. The resistor-capacitance time constant τ_{RC} obtained from the impedance measurement in Figure S9C was 0.43 ms for the asymmetric cell. Figure 2.16 compares the device capacitances at 120 Hz.When normalized to the packaged device volume (90 μm total thickness, in which the redox composite was 270 nm thick, 1.2 cm^2 in area), the asymmetric redox supercapacitor (516 μF/ 0.0108 cm^3 = 47.8 mF cm^{-3}) here demonstrated more than 75 times higher volumetric capacitance than a commercial AEC (380 μF/0.6 cm^3 = 0.63 mF cm^{-3}).

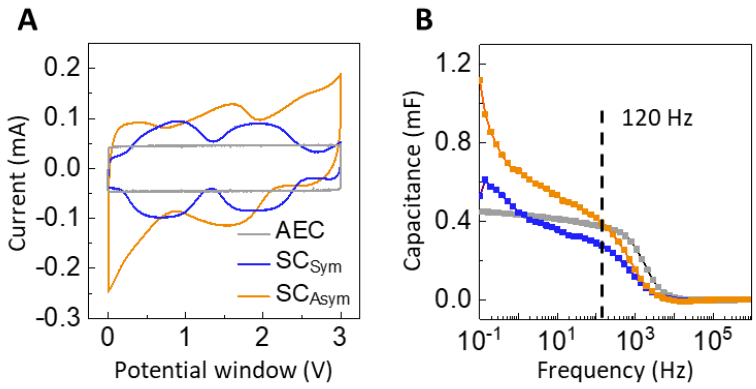

Figure 2.16. (a) Cyclic voltammetry scanned at 0.1 V s^{-1}. The AEC was from Nichicon (470 μF at 6.3 V). (b) Capacitance versus logarithm of frequency, at a bias potential of 3 V, with the corresponding device volumes.

Our supercapacitors were integrated in a rectifying circuit to demonstrate an AC line filtering application as shown in Figure 2.17. The input was a ±3 V sinusoidal signal at 60 Hz, to be rectified by the diode bridge to a 120 Hz wave and then low pass filtered by the capacitor into a direct current (dc) output. The dc output was smooth with a magnitude near 2 V; the 1 V drop from the sinusoidal 3V peak was due to the potential drop across the diodes. There was only 0.04 V negligible difference between using an AEC versus our redox supercapacitors, attributed to the smaller phase angle (75.5° at 120 Hz) in the supercapacitors (~8° smaller than AEC). While there

are prior supercapacitors with higher cut-off frequency, they are limited by a small potential window (0.8–1.6 V) [36,81–83].

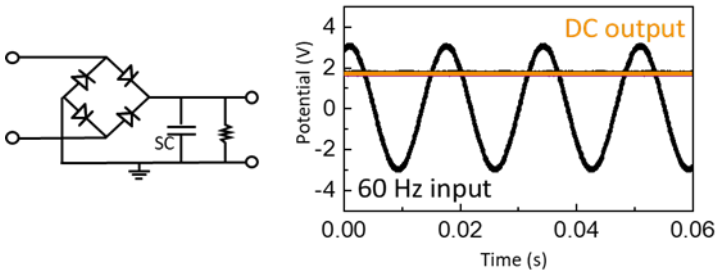

Figure 2.17. Rectifying circuit and the ac line filtering performance of our supercapacitors.

The supercapacitors in this work achieved a significantly higher potential window and energy density than prior electrochemical devices made for AC line filters, as seen in Figure 2.15. Compared to other fast supercapacitors that are limited in their voltage, the 3V operation range decreases the number of layers that need to be connected in series to reach a desired voltage rating. Consequently, the device stack will be considerably more compact with reduced series resistance for power applications.

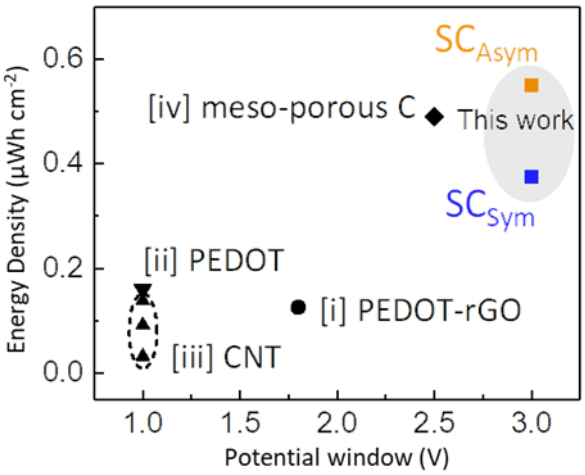

Figure 2.18. Energy densities and cell potentials of various supercapacitors operating at 120 Hz. The data are from [i] Ref. [81]; [ii] Ref. [82], [iii] Ref. [36], and [iv] Ref. [83].

2.4.3 Thick Electrodes Enabling Simultaneous High-power and High-energy Densities

The symmetric and asymmetric electrodes were fabricated with thicknesses of <200 nm to demonstrate their utility in 120 Hz applications. For other use cases such as energy storage buffers in power trains or power supplies for wireless sensors, thicker electrodes that provide increased energy capacities are required. As the electrode thickness was increased, the equivalent series resistance (ESR) became large, impeding operation at high rates. With the new redox composites detailed in this work, we examined the possibility of increasing the energy density while keeping ESR low through the conductive rGO networks. During the fabrication of thick electrodes (~1.6 to 3.2 μm), we annealed the films at 200 °C for 30 min midway through the deposition process, which resulted in improved film conductivity.

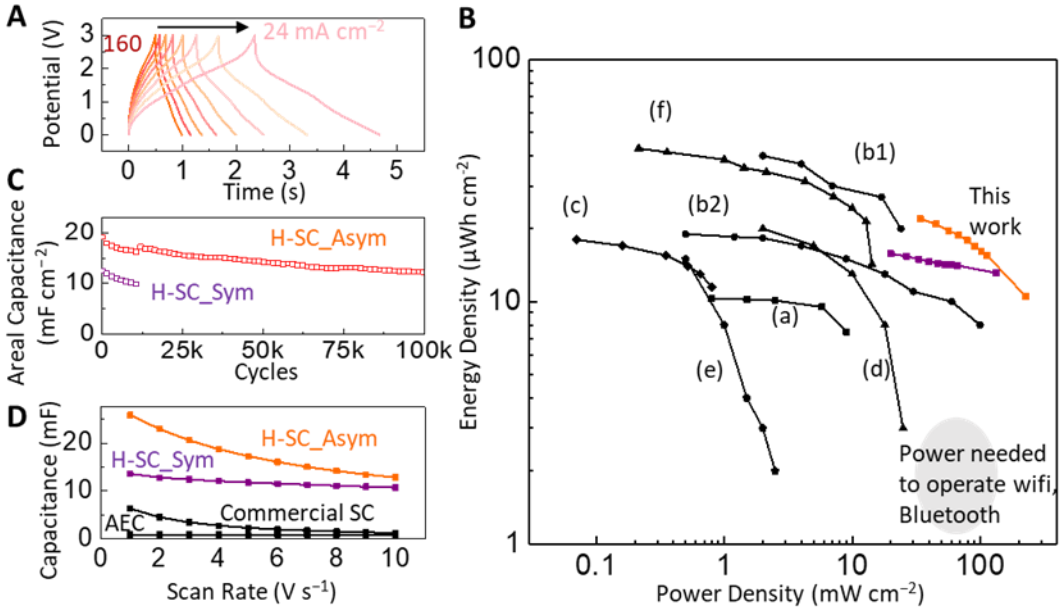

Figure 2.19. (a) GCD curves of the asymmetric supercapacitor, at current densities of 160 mA cm^{-2} and 80—24 mA cm^{-2} in decrements of 8 mA cm^{-2}. (b) Energy density versus power density of state-of-the-art supercapacitors: [a] Vanadium nitride, Ref.[84]; [b1, b2] carbide-derived carbon, Ref. [85]; [c] CuOH@FeOOH nanotubes, Ref. [86]; [d] onion-like carbon, Ref. [87]; [e] MoO_x, Ref.[88]; [f] MnO_2-Graphene, Ref. [58]. (c) Areal capacitance versus charge-discharge cycles. (d) Capacitance as a function of scan rate for our supercapacitors, an aluminum electrolytic capacitor (AEC: Nichicon B01DYJEH22), and a commercial activated carbon supercapacitor (SC: KEMET FG0H103ZF).

Table 2.2. Stability comparison of pseudocapacitive devices and (EDLC).

Electrode	Setup	Potential Window (V)	Retention (%)	Cycles	Charge/ discharge rate	Ref#
Pseudo capacitance materials						
QxTh-rGO/ PEDOT-rGO	2	3	84.1 (11k); 62.7 (100k)	11k; 100k	20 mA cm^{-2}	Our work
QxTh-rGO	3	1.5	92.4	11k	20 mA cm^{-2}	Our work
CuOH@FeOOH nanotubes	2	1.5	82	10k	0.2 mA cm^{-2}	Ref[86]
MoOx	2	1	86.7	2k	2 mA cm^{-2}	Ref[88]
LSG–MnO_2	2	2	96	10k	1 V s^{-1}	Ref[58]
RuO_2	2	1	80	10k	0.1 V s^{-1}	Ref[89]
PANI@rGO/ Mxenes	2	1	84	10k	not given	Ref[90]
MXene	2	0.6	100	10k	3 mA cm^{-2}	Ref[91]
MOF	2	1	94	10k	not given	Ref[92]
Polyaniline	2	0.8	77.1	10k	10 mA cm^{-2}	Ref[93]
PEDOT-MXene	2	0.6	97.5	10k	300 uA cm^{-2}	Ref[94]
MXene-BP	2	0.8	91.7	10k	10 A cm^{-3}	Ref[95]
Vanadium nitride	3	0.6	80	50k	0.05mV s^{-1}	Ref[96]
Vanadium nitride	3	0.6	80	10k	10 mA cm^{-2}	Ref[84]
EDLC materials						
Onion-like carbon	2	3	~100	10k	10 V s^{-1}	Ref[87]
Active carbon	2	3	80	3k	5 mA cm^{-2}	Ref[97]
Carbide-derived carbon	3	0.8	~100	10k	1 mA cm^{-2}	Ref[85]

For the asymmetric supercapacitor using PEDOT-rGO as the cathode and QxTh-rGO as the anode (Figure 2.19a), the GCD characteristics showed the device charging/discharging within 3 V at 160 mA cm^{-2}, which yielded a power density of 227 mW cm^{-2} (114.6 W cm^{-3}). Such a high-power delivery has not been achieved for any materials combination as depicted in the Ragone plot in Figure 2.19b. For comparison purposes, the next highest performing alternative is carbide-

derived carbon [85]. However, these devices show a lower energy density than the ones in this work when power delivery exceeds 30 mW cm^{-2} (15.2 W cm^{-3}). Previously reported organic supercapacitors result in performance that is an order of magnitude lower than demonstrated here.

Conventional electrochemical energy storage devices are slow and rely on bulky AEC buffers to facilitate sufficient power delivery. Our devices directly deliver high power without AECs for common applications such as radio frequency (RF) communication. The energy storage density reached 21.9 μWh cm^{-2} (11 mWh cm^{-3}) at a discharge power of 36 mW cm^{-2} (18.2 W cm^{-3}). This energy capacity meets the needs of a growing number of sensor electronics that are designed to consume low energy on the order of tens of μWh cm^{-2} [10]. This capacity allows these supercapacitors to serve as a stand-alone energy supply and offers an alternative to battery technologies limited by short cycle lifetime.

The devices were fully charged and discharged for 11,000 redox cycles as shown in Figure 19c, with a capacitance retention of 84.1% and 77.5% for the asymmetric and symmetric cells, respectively. The comparison of cycling stability among pseudocapacitive devices are shown in Table 2.2. Note that our cycling condition was across 3 V, and if the potential was decreased to 1.5 V, capacitance retention would improve to 92%. After 100,000 cycles of 3 V operation, the asymmetric device maintained 63% of its initial capacitance, and the reduced value would still be better than the initial volumetric capacitance of commercial devices in Table 2.3. Our symmetric cell showed a smaller areal capacitance and slightly reduced capacitance retention than the asymmetric device; however, the symmetric cell was less adversely affected by an increase in the scan rate from 1 V s^{-1} to 10 V s^{-1} (Figure 19d). The low dependence on scan rates indicates that the redox kinetics in QxTh-rGO composite materials are fast and do not limit the charge/discharge rate. For the asymmetric cell, the PEDOT-rGO cathode was more resistive than QxTh polymer-

rGO anode, leading to a larger drop in capacitance upon increasing the scan rates. On account of its high degree of charge delocalization, the open-shell QxTh polymer-rGO composite is shown to be an excellent anode that facilitates fast kinetics and high redox stability using a large potential window that has eluded other n-type Faradaic electrodes.

Table 2.3. Capacitance and energy density comparisons, including the volume of package materials.

	AEC (Nichicon B01DYJEH22)	Activated C SC (KEMET FG0H103ZF)	H-SC_Sym	H-SC_Asym
Capacitance (mF) at 1 V s^{-1}	0.94	6.35	13.6	25.8
Volume (cm^3)	0.60	0.39	0.023	0.023
Potential window (V)	6.3	12	3	3
Volumetric capacitance (mF cm^{-3})	1.5	16.3	591.3	1121.7
Volumetric energy density (μWh cm^{-3})	8.3	325.1	739	1402

2.5 Application of micro-supercapacitors in RF energy harvesting

The radar plot in Figure 2.20a compares our asymmetric device with three other state-of-the-art supercapacitors. The device in this work featured much higher power density and potential window than the others while showing similar values in terms of stability and energy density as listed in Table 2.5. The asymmetric device displayed better kinetics and a volumetric energy density 4.3-fold higher than commercial activated carbon supercapacitors (Table 2.4, Figure 2.20b). These results are consistent with high storage capacity, high power, and outstanding stability, offering a potential replacement for AECs or batteries within miniaturized and low-power electronics. Lastly, we integrated our symmetric supercapacitor with an RF energy harvesting board, in which the cell was the sole energy storage component used to power the wireless circuit. The resulting charge and discharge cycles of the supercapacitors were shown in Figure 2.20c,

demonstrating the potential of using our redox supercapacitors as energy storage solutions for wireless sensors.

Table 2.4. Table of the parameter values used to plot the comparison radar plot in Figure 2.20a.

	Ref (17)	Ref (20)	Ref (8)	This work
Stability (% at 10K cycles)	80	100	96	86
Potential Window (V)	0.6	0.8	1.6	3
Areal Power Density (mWh cm^{-2})	25	24	14.3	113.6
Areal Energy Density (μWh cm^{-2})	3	20	14.3	15.5

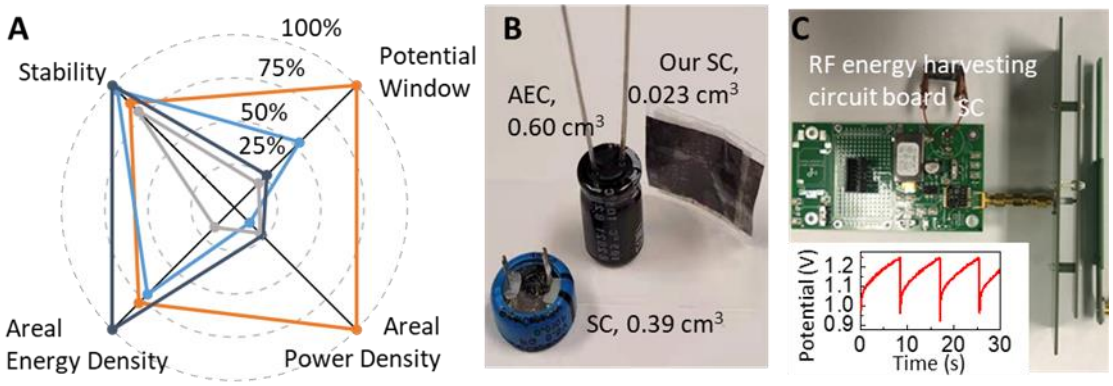

Figure 2.20. (a) Comparison between state-of-the-art devices and asymmetric device (orange data) in this work. Dark blue: Ref. [85]; Light blue: Ref. [58]; Gray: Ref. [84]. (b) Photograph of the devices. (c) Photograph of a radio-frequency energy harvesting circuit with our symmetric supercapacitor as the energy storage unit. The inset shows the charging and discharging cycles.

2.6 Conclusion

This work presents a new design that simultaneously advanced the three key metrics of power, energy, and stability in redox supercapacitors. This was accomplished through the synergistic combination of novel open-shell polymers that demonstrate enhanced delocalization in their redox states with rGO and the utilization of low-cost electro-deposition methodologies. The micron thick electrodes maintained fast kinetics through the conductive rGO framework and showed high energy density on account of the conjugated polymer, which enabled operation with a large

potential window of 3 V. Impedance analyses and modeling demonstrated that optimization of the polymer-to-rGO ratio improved interfacial charge-transfer resistance and diffusion-controlled resistance. With a high degree of electronic delocalization and mechanical flexibility in the composite electrodes, our supercapacitors exhibited exceptional capacitance retention of 84% in supercapacitors after 11,000 full redox cycles, offering the critical benefit of long cycle life to significantly reduce maintenance and replacement costs.

For use case studies, we successfully applied our redox supercapacitors in a 120 Hz filter circuit. The superior volumetric capacitance and energy density make them an attractive alternative to bulky AECs. As the active material loading was increased, the device response decreased below 120 Hz, but the power density remained outstanding. These devices demonstrated charge/discharge power of 227 mW cm^{-2} (114.6 W cm^{-3}) with an energy density of 10.5 μWh cm^{-2} (5.3 mWh cm^{-3}). At a power rate of 36 mW cm^{-2} (18.2 W cm^{-3}), the asymmetric device provided an energy density of 21.9 μWh cm^{-2} (11 mWh cm^{-3}). Such high-power and high-energy performance showcased the potential of this class of redox supercapacitors to serve as compact, fast charging power supplies, that are well-suited to meet the rising demands of wireless electronics.

Chapter 2, in part, is a reprint of the material as it appears in Cell Reports Physical Science. Jiaxi Liu, Naresh Eedugurala, Paramasivam Mahalingavelar, Daniel J Adams, Kaiping Wang, Kevin S Mayer, Jason D Azoulay, Tse Nga Ng. Ultrafast high-energy micro-supercapacitors based on open-shell polymer-graphene composites. The dissertation author was the primary investigator and first author of the paper.

CHAPTER 3 STRUCTURAL PSEUDOCAPACITORS WITH REINFORCED INTERFACES TO INCREASE MULTIFUNCTIONAL EFFICIENCY

3.1 Design of Structural Energy Storage Devices

Today's electrochemical storage devices are restricted in capacity, a key challenge that limits the operational time of wireless devices and invokes range anxiety in the electric transportation sector. To increase the storage capacity, one approach is to leverage structural volume to create structural batteries/supercapacitors,[50,51,98–103] in which energy storage is integrated with load-bearing functions and thus facilitates mass and weight savings. For example, carbon fibers used for structural reinforcements also exhibit good conductivity. So in multi-functional structures, the carbon fibers can serve as electrode scaffolds with surface modification or added active materials, and then the electrodes are stacked with separators and solid-state electrolytes to complete an electrochemical cell. This layered configuration is similar to high-strength laminates and incorporate both electrochemical and mechanical functions, attractive to aviation and maritime industries where structural composites are already prevalent.[104–106] However, when comparing the multi-functional composites to their mono-functional counterparts, there are additional challenges with conflicting requirements between electrochemical functions and mechanical properties.

In this chapter, we develop strategies based on interfacial engineering to decouple the trade-offs and concurrently improve energy storage and mechanical strength in structural supercapacitors. Supercapacitors offer much longer cycle life than batteries and are conducive to durable operation, which is advantageous in scenarios where the structures are integrated and not frequently replaced. Yet the energy and power densities of structural supercapacitors have been substantially lower than mono-functional devices due to shortcomings in the current implementation of structural electrodes and electrolytes.

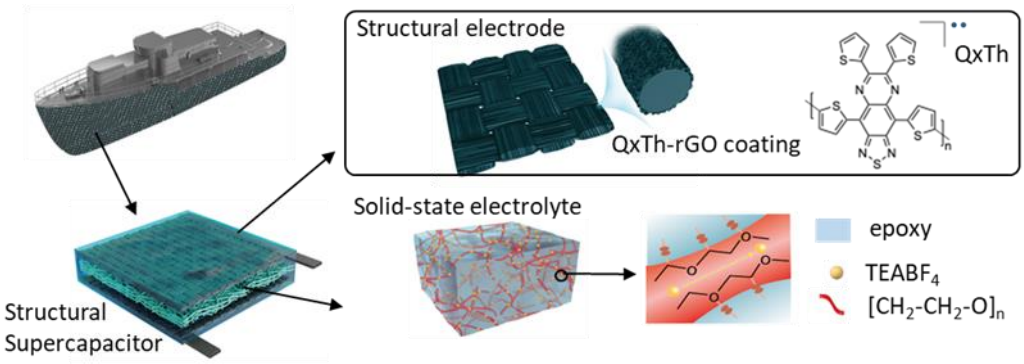

Figure 3.1. Schematics of our structural supercapacitor. The redox polymer coating QxTh-rGO on carbon fibers increases gravimetric capacitance of the electrodes. An ion-percolation network in the epoxy matrix offers high ionic conductivity and mechanical strength in the functionally graded electrolyte.

First, for structural electrodes, the limitation stems from the trade-off between mechanical strength and specific capacitance. To increase electric double layer capacitance, carbon fiber electrodes were treated by chemical activation processes at high temperature, but the treatment reduced structural strength due to damaged fibers.[107] Alternatively, the surface of carbon fibers were modified by carbon aerogel[108] or metal oxide,[109] though these electronic materials did not contribute to mechanical reinforcement.

Second, for the structural electrolyte, previous designs have suffered from low ionic conductivity that leads to loss of energy and power density as charge exchange sites were inaccessible. The ionic conductivity is typically inversely proportional to the mechanical modulus of the composite.[110,111] Cross-linked epoxy resins are one of the most widely used matrices for laminates and have been blended with ionic-liquid salts to form phase-segregated electrolytes,[112] although their mechanical moduli were drastically diminished due to disruptions to cross-linking. Meanwhile, epoxy matrices with low salt content showed better mechanical properties but low ionic conductivity. While silica or alumina fillers[113–115] were added to increase ion diffusion paths[116], the improvements were incremental and the low ionic conductivity was still severely

limiting the kinetics in structural supercapacitors, resulting in peak power that was an order of magnitude less than typical mono-functional devices.[51]

To overcome the bottlenecks in structural supercapacitors, this chapter focuses on the crucial interfaces of electrodes and electrolyte as illustrated in Figure 3.1. For the structural electrode, the carbon fibers are conformally coated with a stable conjugated redox polymer[33,117] that contributes Faradaic charge storage with a large 3 V potential window and raises the specific capacitance significantly compared to prior electrodes. In addition to favorable electronic properties, the redox polymer enhances mechanical moduli of the composite[118] on account of its sulfur-containing moieties that can form hydrogen bonds or react with cross-linkers in the electrolyte. The structural electrolyte is based on an epoxy matrix improved with polyethylene oxide (PEO),[119,120] which provides percolation conduits for ion transport while maintaining mechanical strength much better than ionic-liquid channels in prior phase-segregated electrolytes.

A key design in this work leverages a gradient composition in the electrolyte to increase the kinetics at the electrode-electrolyte interfaces and push up the power density considerably in structural supercapacitors to be on par with mono-functional devices. The new gradient electrolyte is tuned such that the regions immediately next to electrodes incorporate a higher concentration of ion-conducting PEO to increase access to electrolyte salts and promote fast kinetics, whereas the middle region contains a lower concentration of PEO in the epoxy matrix to better support load transfer while still maintaining ion percolation. The performance of structural supercapacitors with uniform or gradient electrolyte is assessed to investigate how the structural adjustments affect power and energy density, cycling stability, and overall mechanical properties including tensile and flexural stress under deformation. The combined electrochemical and mechanical performance

is evaluated through a metric of multi-functional efficiency for comparison with state-of-the-art devices.

Finally, as a feasibility study, a structural supercapacitor was fabricated to serve as the hull of a model boat. The boat is integrated with a solar panel for charging up the supercapacitor hull, which in turn powers up the boat motor to cruise across a pool. This demonstration shows the potential of structural supercapacitors to facilitate mass savings and increase the capacity for energy harvesting and storage in future electric systems.

3.2 Preparation and Characterization of Structural Electrode

3.2.1 Preparation of QxTh-rGO@CF structural electrode

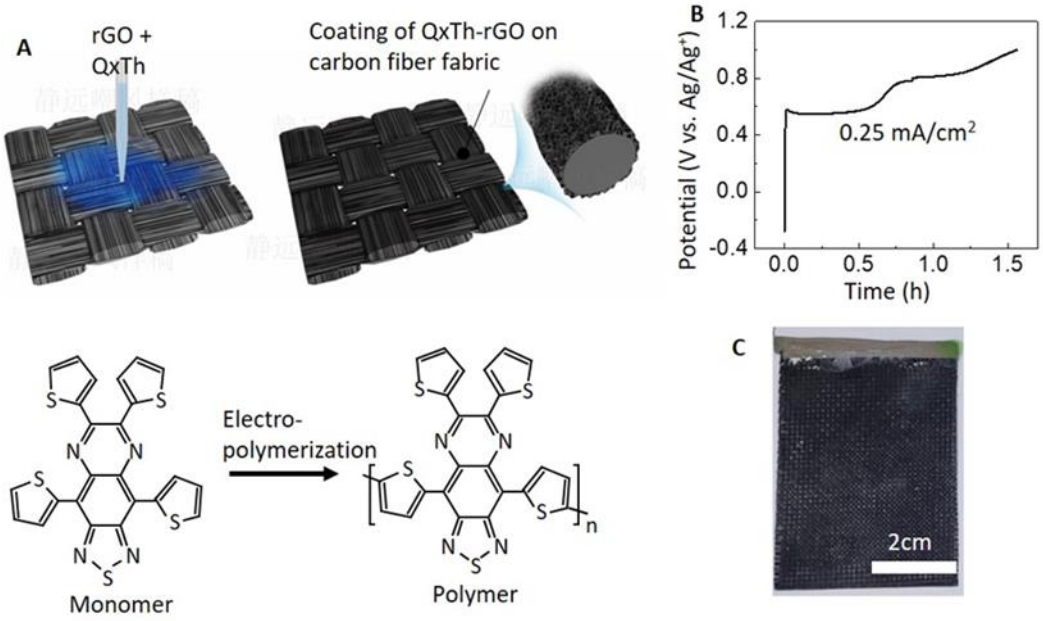

Figure 3.2. (a) Schematics of polymerization process on carbon fiber (CF). (b) The potential of the working CF electrode as a constant current of 0.25 mA cm^{-2} was applied in the cathodic electropolymerization process. (c) Photograph of a CF fabric coated with QxTh-rGO.

The structural electrodes were made from a carbon fiber (CF) fabric modified by a coating of open-shell conjugated redox polymer and reduced graphene oxide (rGO). The coating was prepared by electrodeposition, in which a solution mixture of rGO and monomer 4,6,7,9-

tetra(thiophen-2-yl)-[1,2,5]thiadiazolo[3,4-*g*]quinoxaline (QxTh) was drop-casted onto the CF fabric and reacted by cathodic electro-polymerization to form the pseudocapacitive coating. The redox polymer QxTh was selected because of its high specific capacitance (297.6 F g^{-1}) and stability over a wide potential window of 3 V due to its open-shell characteristics,[117] and rGO was incorporated to enhance the conductivity and porosity of the coating. As seen in the scanning electron microscopy (SEM) images, the surface of the pristine CF was smooth in Figure 3.2; then after the polymerization process, a porous QxTh-rGO coating was conformally deposited on the CF in Figure 3.3. The porosity was beneficial for the transport of counter ions and tolerant to dimensional changes upon redox cycling.

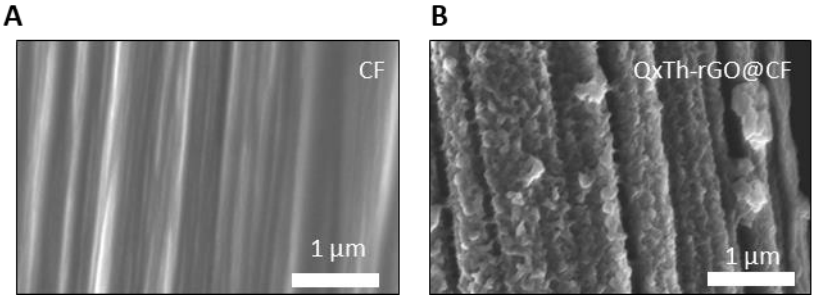

Figure 3.3. Characterization of structural electrodes. SEM images of (a) pristine carbon fibers and (b) carbon fibers coated with QxTh-rGO. MXene (MX)/ANF[121].

3.2.2 Electrochemical performance of QxTh-rGO@CF structural electrode

From cyclic voltammetry measurements, Figure 3.4a presents the gravimetric capacitance of the pristine and QxTh-rGO coated CF electrodes. Accounting for the weight of the CF (12.07 mg per 1 cm^2 electrode area), the pristine CF electrode showed a capacitance of 0.16 F g^{-1}, while the QxTh-rGO@CF electrode reached 65.2 F g^{-1} when characterized as an anode (in the voltage range of -0.5 V to -2 V vs Ag/Ag^+ reference), and 34.6 F g^{-1} as a cathode (-0.5 V to 1 V vs Ag/Ag^+) in Figure 3.4a. A coating of 3 mg QxTh-rGO on 9.93 mg CF increased the electrode gravimetric

capacitance by up to 400-fold compared to CF. The specific capacitance can be raised further by depositing more QxTh-rGO onto the CF surface.

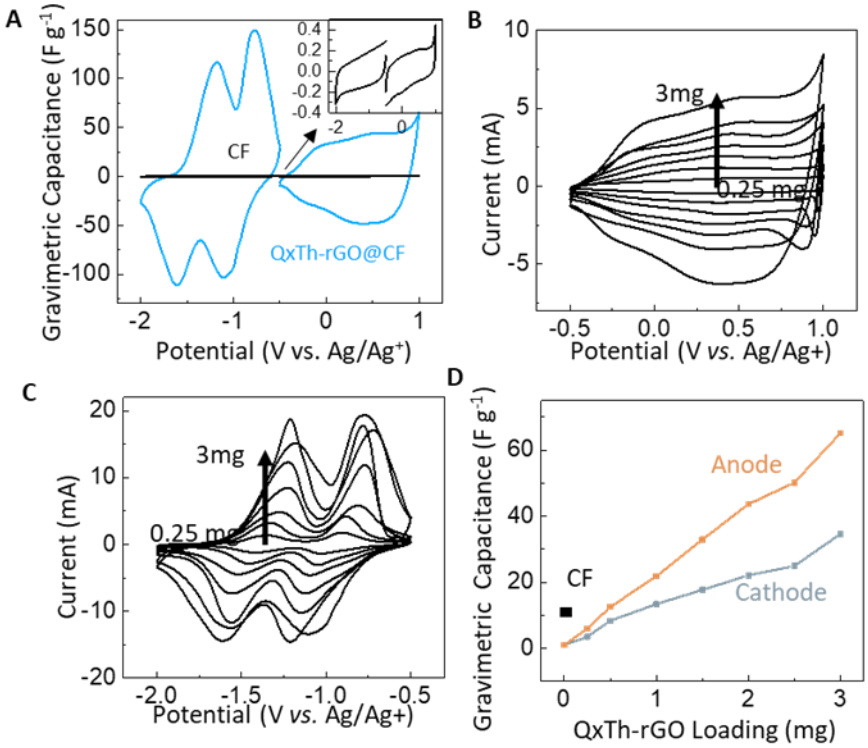

Figure 3.4. (a) Gravimetric capacitance extracted from cyclic voltammetry at a scan rate of 10 mV s^{-1}. The QxTh-rGO sample is at 3 mg cm^{-2} loading. The inset zooms in on the data for carbon fibers. CV curves at 10 mV s^{-1} for samples with different QxTh-rGO loading, from 0.25, 0.5, 1, 1.5, 2, 2.5, 3 mg, in the (b) cathode potential range of -0.5 V to 1 V and (c) anode potential range of -2 V to -0.5 V. (d) Gravimetric capacitance as a function of QxTh-rGO loading on the carbon fiber. The capacitance was calculated based on cyclic voltammetry data collected at 10 mV s^{-1} in a 0.5 M $TEABF_4$/PC electrolyte.

The energy storage mechanism of QxTh-rGO was also studied through Augustyn-Simon-Dunn analysis.[122] In this method, the current *i* and the scan rate υ of cyclic voltammetry (CV) is expressed as $i(V) = i_c + i_d = k_1 v + k_2 v^{0.5}$, or equivalently $i(V)/v^{0.5} = k_1 v^{0.5} + k_2$.[123,124] where k_1 is the capacitive constant (related to the electric double layer formation), k_2 is the diffusion-controlled constant (related to redox reactions), and v is the scan rate. A set of CV data measured at various scan rates were obtained and plotted as $i(V)/v^{0.5}$ versus $v^{0.5}$ in Supplemental Figure 3.5. In the

QxTh-rGO supercapacitor, the contribution of capacitive EDL storage was 50% at a slow scan rate of 1 mVs^{-1} and increased to 73% with a faster scan rate of 7 mVs^{-1}.

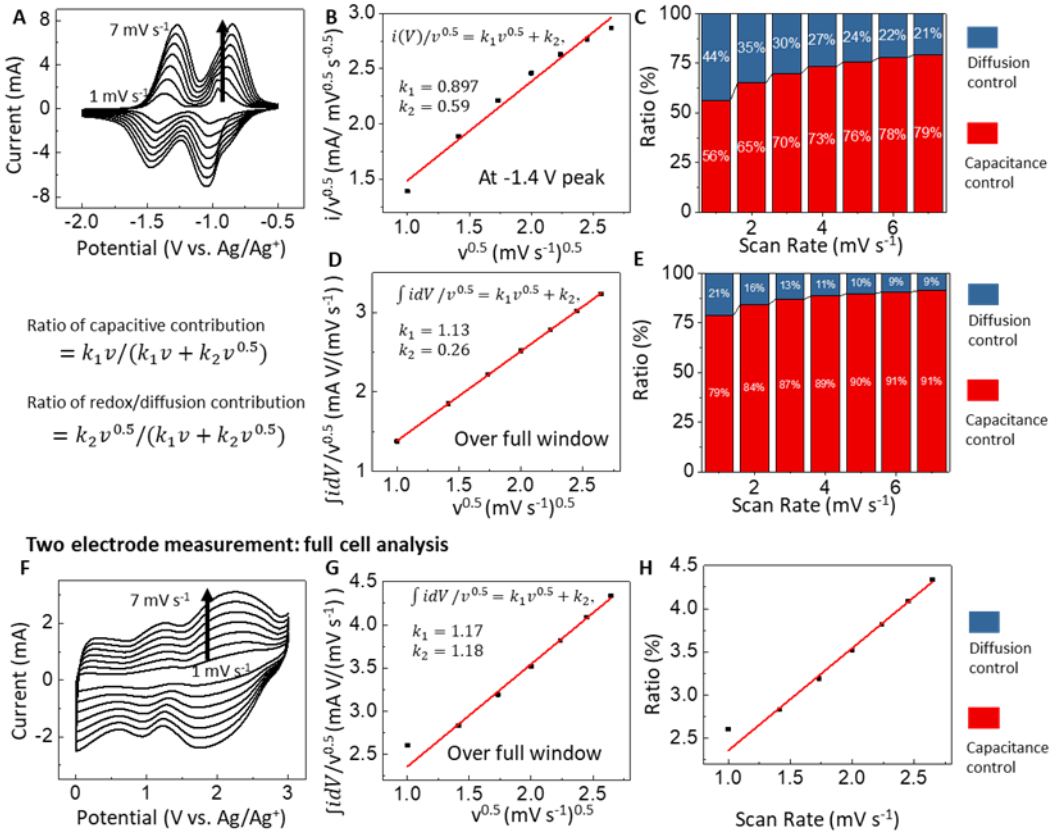

Figure 3.5. (a) CV curves from 1 mV s^{-1} to 7 mV s^{-1} of QxTh-rGO@CF electrode with 2 mg QxTh-rGO loading. (b) Current divided by scan rate at the oxidation peak of -1.4V as a function of scan rates (solid line is the fitting curve). (c) Ratio of current contribution from capacitive versus redox mechanism. The equations for ratio calculations are shown below part a. (d) Integrated area of each CV curve divided by the respective scan rate, as a function of scan rates. This was done to average over the full potential window, as opposed to only at one peak voltage as done in part b. (e) Ratio of capacitive versus redox mechanism calculated from part d. (f) CV curves from 1 mV s^{-1} to 7 mV s^{-1} of QxTh-rGO@CF on a supercapacitor with a liquid electrolyte of 0.5 M $TEABF_4$ in PC, as we are focusing on identifying charge storage mechanisms of electrodes and need to exclude diffusion resistance due to solid electrolyte. (g) Integrated area of each CV curve divided by the respective scan rate, as a function of scan rates. (h) Ratio of capacitive versus redox mechanism calculated from part g.

In galvanostatic charge-discharge tests, the QxTh-rGO@CF electrode exhibited capacity retention of 96.1% as an anode and 97.5% as a cathode after 10,000 full charge/discharge cycles (Supplemental Figure S4). This retention result indicates great redox stability of QxTh due to extended delocalization of charge density within this open-shell conjugated polymer.

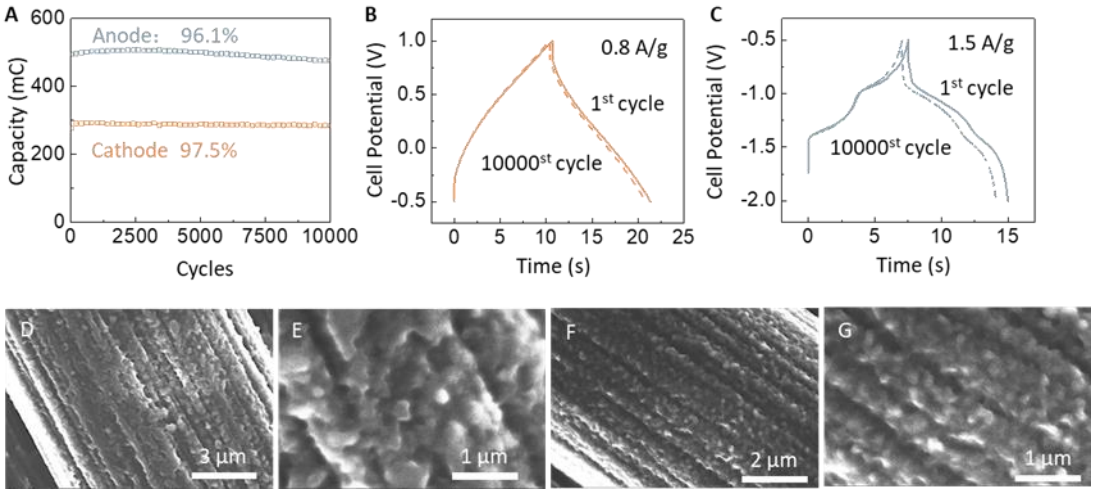

Figure 3.6. (a) Redox cycling performance of QxTh-rGO-CF electrodes in a 3-electrode setup with 0.5 M $TEABF_4$/PC electrolyte. The 1st and 10000st galvanostatic charge-discharge (GCD) characteristics of (b) the cathode and (c) the anode. Scanning electron microscopy (SEM) images of CF-QxTh-rGO before (d, e) and after (f, g) the 10000 charge-discharge cycles.

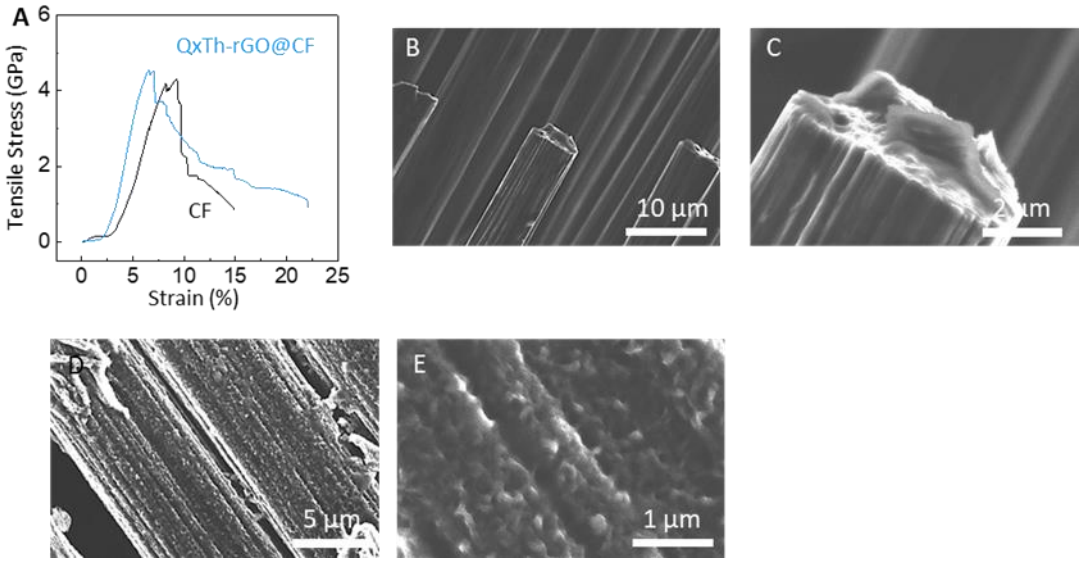

Figure 3.7. (a)Tensile stress versus applied strain for the pristine and modified carbon fiber samples. SEM images of (b, c) CF and (d, e) QxTh-rGO-CF after the tensile test.

In addition to the excellent electrochemical performance, the QxTh-rGO coating provided additional mechanical reinforcement to the structural electrode. In Figure 3.6, the maximum tensile strength (stress-to-failure point) was 4.5 GPa for QxTh-rGO@CF, slightly better than pristine CF at 4.3 GPa. The tensile modulus was 103 GPa for QxTh-rGO@CF, also higher than the CF

modulus of 84 GPa. This higher mechanical performance was attributed to the polymer acting as a binder for carbon fibers.[120] After tensile strain tests, SEM images showed that QxTh-rGO was still conformally coated on the strained fibers (Figure 3.7), confirming the strong adhesion of the polymer coating, superior to particulate pseudocapacitive materials[109] that had issues with long-term adhesion to CF.

Among state-of-the-art structural electrodes in Figure 3.8, QxTh-rGO@CF offered the highest tensile strength, as the facile processing at room temperature did not damage the CF and retained the inherent structural organization that imparted robust mechanical properties to CF weaves. While the specific capacitance of our electrodes was not the highest in the comparison chart of Figure 3.8, the other materials showed an order of magnitude lower tensile strength and moduli and were further limited in their operational voltage window *V*. As summarized in Supplemental Table 3.1, the composites of MXene or aramid nanofibers were limited to a potential window below 1 V compared to the stability window of 3 V in QxTh-rGO@CF. Since energy density *E* is proportional to $E = 0.5CV^2$, at a given capacitance *C*, the approach of expanding the potential window from 1 V to 3 V would offer a nine-fold increase in energy density.

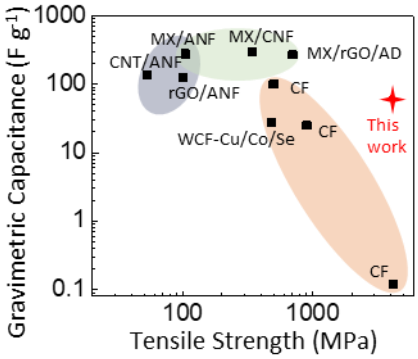

Figure 3.8. Comparison of gravimetric capacitance and tensile strength of structural electrodes: carbon fiber (CF)[107]; rGO/aramid nanofiber (ANF)[125]; carbon nanotube (CNT)/ANF[126]; MXene (MX)/ANF[121]; MX/cellulose nanofibrils (CNF)[127]; MX/rGO/AD[128]; Woven carbon fiber (WCF)-Cu/Co/Se.[129]

Table 3.1. Performance comparison of structural electrodes.

Electrode Materials, in reference [#]	Tensile strength (MPa)	Tensile Modulus (GPa)	Electrode capacitance (F g^{-1})	Potential Window (V)	Capacity retention after # of redox cycles
QxTh-rGO on CF (this work)	4500	103	65	3	96.1% at 10k
CF (measured in this work)	4300	84	0.16	3	not measured
MXene $Ti_3C_2T_x$/ANF [121]	104	1.42	278	0.8	91% at 10k
CNT/ANF[126]	53	5.4	135	0.8	98.4% at 5k
MXene/CNF[127]	341	20.2	298	0.9	~100% at 10k
Mxene/rGO/AD[128]	699	5.8	269	0.8	98% at 17k
rGO/ANF;[125]	101	14	125	1	93% at 1k
Cu-Co-Se on woven carbon fiber[129]	481	32.7	28	1	96.5% at 2k
Carbon Nanofibers [107]	900; 700	38.1; 15.9	25; 100	1; 1	80% at 4k; 91% at

3.3 Preparation and Characterization of Structural Electrolyte

3.3.1 Design of Structural Electrolyte

For multi-functional laminates, the solid-state electrolyte plays key roles in ions conduction and load bearing, to achieve inherently more resilient and safer devices than conventional liquid/gel electrolytes when subjected to mechanical loads. Here we chose epoxy resin as the base for our solid polymer electrolyte and adjusted its composition in terms of electrolyte salt concentration, ion percolation agent PEO, and functionally graded configuration[130] to maximize the electrochemical and mechanical performance of the composite. The epoxy provided cross-linked bonds at interfaces to strongly bind the electrode and separator components together for high strength. The addition of ion-conducting polymer PEO created diffusion channels as a percolation network through the epoxy matrix, allowing us to replace expensive ionic-liquid salts in previous

phase-segregated channel designs[112] with tetraethylammonium tetrafluoroborate ($TEABF_4$) salts that are less expensive compared to ionic liquids. More importantly, as a common binder,[119] PEO would crosslink with epoxy to maintain mechanical modulus and would certainly be stronger as a solid than ionic-liquid channels and unaffected by aggregation problems like mesoscopic inorganic fillers, while enhancing ionic conductivity of the solid polymer electrolyte.

3.3.2 Ionic Conductivity of Structural Electrolyte

The study of electrolyte composition is displayed in Figure 3.9, for which we categorized the results into four groups. The salt and PEO ratios (wt%) were calculated from the weight of the respective component divided by the total weight ($TEABF_4$ salt + PEO + epoxy resin). Electrochemical impedance data used to calculate the ionic conductivities are shown in Supplemental Table 3.2. For epoxy mixed with electrolyte salts only, the electrolyte ions were not able to diffuse in the cross-linked resin, and the ionic conductivity was very low >0.04 mS cm^{-1} [type (i) in gray color]. Upon adding PEO to the resin, ion diffusion along PEO improved transport and raised the ionic conductivity to 0.14 mS cm^{-1} [type (ii) in green]. If more salt was added per PEO amount, the ionic conductivity was increased further and reached up to 0.4 mS cm^{-1} [type (iii) in blue]. However, increasing the salt ratio beyond 20 wt% affected processing and mechanical performance, because the $TEABF_4$ salts were dissolved in a propylene carbonate solvent which slowed down the cross-linking reaction in the epoxy, and the residual solvent decreased the mechanical strength. Meanwhile, increasing the PEO ratio [type (iv) in orange] has a similar effect of reducing mechanical moduli because of the low rigidity of PEO. Then, for device fabrication, we used a combination of two electrolyte compositions, denoted by the blue (18 wt% salt, 9 wt% PEO) and green (5 wt% salt, 10 wt% PEO) open circles in Figure 3A, to construct a functionally graded electrolyte.

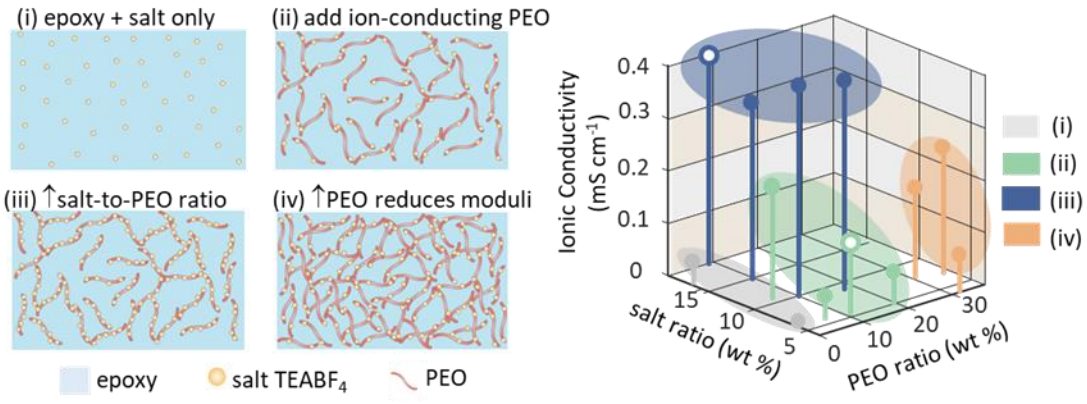

Figure 3.9. Schematics and measurements of ionic conductivity as the electrolyte composition was varied to different salt:PEO:epoxy ratios.

Table 3.2. Ionic conductivity of structural electrolytes with different PEO and salt ratios. Area of cathode and anode were 0.78 cm^2; the average thickness of the electrolytes was 70 µm.

PEO %	Salt %	Ionic conductivity (mS/cm)
0	6	0.01
0	16	0.04
19	5	0.06
6	6	0.05
10	5	0.14
5	10	0.21
10	10	0.35
18	9	0.37
10	14	0.33
10	18	0.4
31	7	0.17
35	7	0.24
32	4	0.06

3.3.3 Gradient Electrolyte Design for Structural Supercapacitors

In structural supercapacitors, the electrolyte was typically a uniform composite directed by vacuum infusion to flow through the electrodes and separator and then solidified together. The epoxy resin is essential to maintain rigidity for load support, but it is electrochemically inert and limits surface adsorption and interfacial redox reactions that dictate the cell capacitance and energy

storage capacity. Instead of a uniform electrolyte, we designed structural supercapacitors with a functionally graded electrolyte illustrated in Figure 3.10a to improve ion exchange at the electrolyte-electrode interfaces. For the functionally graded (namely, gradient) structure, the electrodes were coated with an electrolyte with a high salt ratio, more specifically, of the composition indicated by the blue open circle [type (iii) in Figure 3.9]. This choice facilitated ion access to electrode surfaces and was favorable for capacitance; however, the high salt ratio compromised the mechanical properties of the epoxy. Hence, to balance mechanical and electrochemical performance, the middle region of the electrolyte (where the separator was embedded) used the composition with a low salt ratio as indicated by the green open circle [type (ii)], which still retained sufficient ion percolation network while offering high mechanical strength. The different electrolytes were stencil-printed onto the electrodes or separator, partially cured, and then hot pressed together to complete curing. The solid polymer electrolyte penetrated into and enclosed the electrodes very well to ensure intimate contact, as seen in the SEM image in Figure 3.10b.

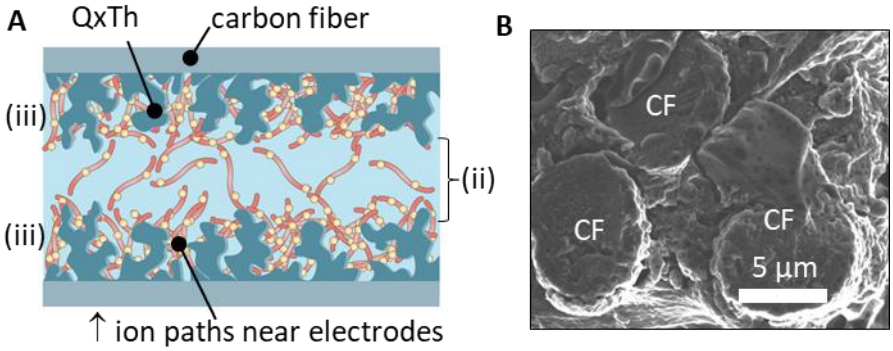

Figure 3.10. (a) A cross-sectional schematic of the electrolyte with a gradient composition in which regions near electrodes had higher concentration of salt and PEO than in the middle to improve device kinetics. (b) SEM image of the solid polymer electrolyte infiltrating around the carbon fiber electrode.

3.3.4 Tradeoff Problem Between Electrochemical Performance and Mechanical Performance of Structural Supercapacitors

Figure 3.11 compares the flexural properties of different electrolytes. The uniform type (ii) electrolyte showed a high flexural strength of 130 MPa, but its ionic conductivity was only 0.14 mS cm^{-1}. In contrast, the uniform type (iii) electrolyte was lower in flexural strength at 75 MPa while higher in ionic conductivity at 0.4 mS cm^{-1}. The gradient electrolyte combined the two compositions and attained a flexural strength of 91 MPa, while maintaining a high ionic conductivity of 0.4 mS cm^{-1}. Thus, the gradient design gained the benefits of increased mechanical strength without sacrificing electrochemical performance.

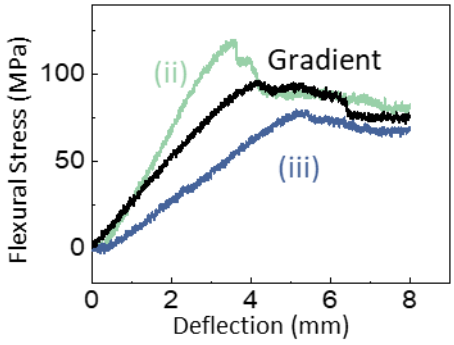

Figure 3.11. Flexural stress versus deflection on samples with uniform or gradient electrolyte. The uniform electrolyte composition corresponds to the open circles in Figure 3.9.

Figure 3.12a presents the electrochemical characteristics of three devices, comparing the above gradient electrolyte, a uniform electrolyte, and a non-structural PEO electrolyte without epoxy. The electrolyte with no epoxy and solely PEO (orange curve, salt:PEO at 33 wt.%) can be considered as an upper bound for the electrochemical performance in solid polymer electrolytes, but it is mono-functional and cannot support load-bearing functions because PEO will deform easily on account of its low mechanical moduli. The uniform electrolyte was comprised of a PEO-epoxy resin with a low salt ratio [composition at the green open circle, type (ii) in Figure 3.9]; the

associated device (green curve) exhibited the lowest specific capacitance among the three structures and only one redox peak in the cyclic voltammetry data as opposed to two peaks in the other devices, indicating slow kinetics due to low ionic conductivity. The gradient electrolyte (black curve) improved the interfacial kinetics and increased the device specific capacitance by ~10% across all scan rates when compared to the uniform electrolyte (Figure 3.12a).

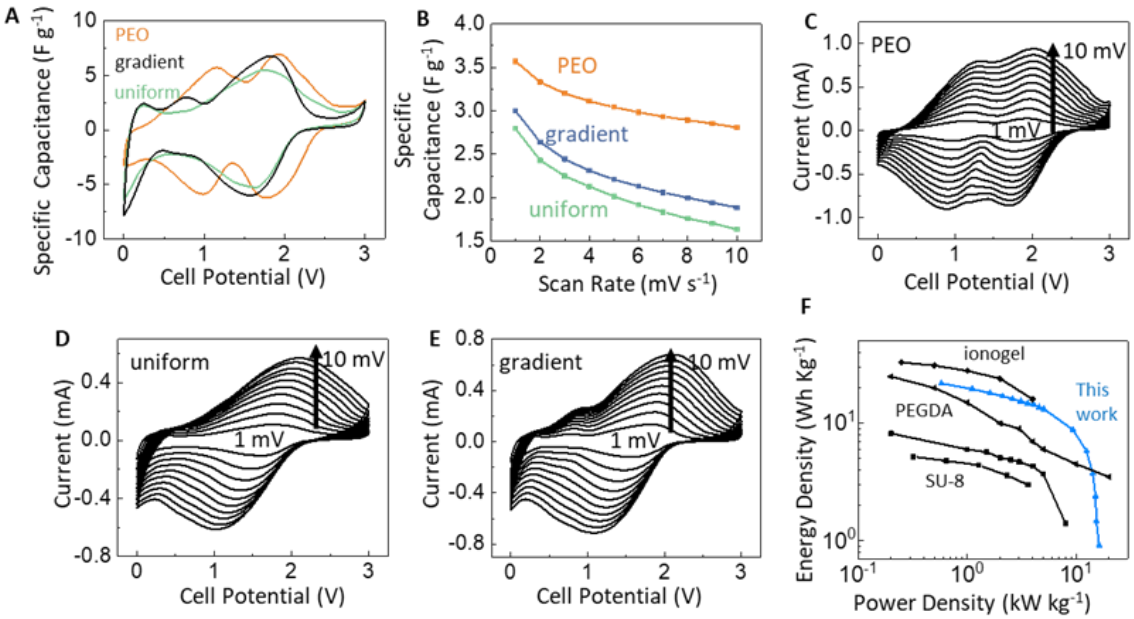

Figure 3.12. (a) Cyclic voltammetry at a scan rate of 1 mV s^{-1} on structural supercapacitors with different polymer electrolytes. (b) Specific capacitance versus scan rate of structural supercapacitors with different polymer electrolytes. (c) PEO only; (d) uniform structural electrolyte; (e) gradient structural electrolyte, scanned at 1-10 mV/s. (f) Comparison of energy and power densities in state-of-the-art supercapacitors using solid-state electrolytes: ionogel[131]; Polyethylene glycol diacrylate (PEGDA)[132]; PEO[133]; SU-8[84].

Overall, our multi-functional supercapacitor with the gradient electrolyte were comparable to devices with mono-functional gel electrolytes, providing power and energy densities in similar orders of magnitude in Figure 3.12f. One reason for the high performance is that our device used pseudocapacitive QxTh-rGO@CF electrodes that did not rely as much on interfacial porosity and ionic rearrangement as electric double layer (EDL) electrodes, making our design favorable for pairing with solid electrolytes. Our redox electrode working with the gradient electrolyte retained 83% of capacitance in comparison to when it was operated in a liquid electrolyte. In contrast, an

EDL activated-carbon device with a solid electrolyte retained only 15% of capacitance, as shown in Figure 3.13. Here the redox electrode and gradient electrolyte design promoted fast kinetics to achieve power densities on the level of typical mono-functional supercapacitors, and this is exciting for removing the major drawback of low power outputs in structural supercapacitors. The stability of the structural supercapacitor was excellent with > 99% Coulombic efficiency and 84% capacity retention after 10,000 full charge-discharge cycles over a wide potential window of 3 V (Figure 3.14).

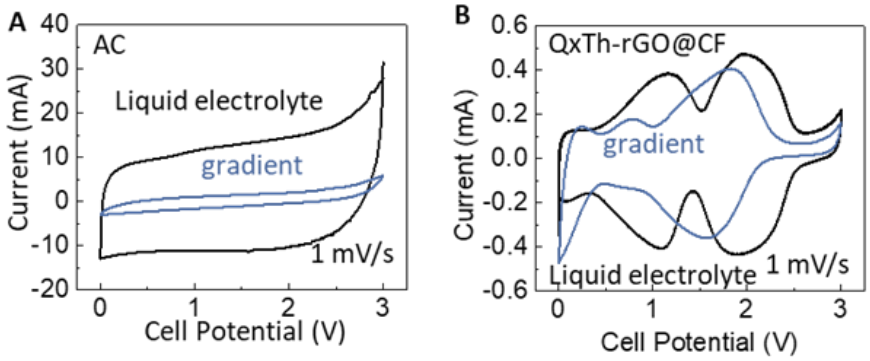

Figure 3.13. CV characteristics of supercapacitors with (a) activated carbon electrodes and (b) QxTh-rGO@CF electrodes in liquid electrolyte of 0.5 M $TEABF_4$ in PC (black) or our gradient solid-polymer electrolyte (blue).

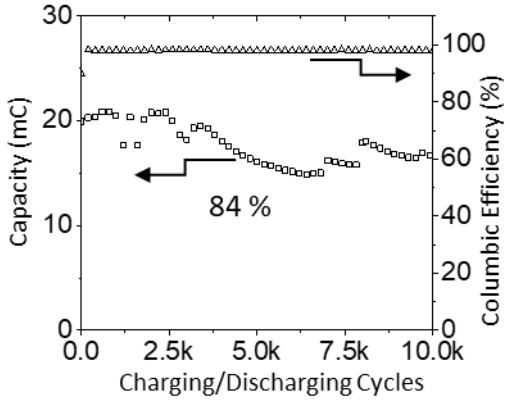

Figure 3.14. Capacitance retention and Coulombic efficiency of the structural supercapacitor with the gradient electrolyte under full charge-discharge cycles of 3 V at a current density of 2 mA cm^{-2}. Fluctuations near 7k and 8k cycles were due to the electrode contacts being re-secured.

3.3.5 Mechanical Properties of Structural Supercapacitors

The mechanical properties of the structural supercapacitor with the gradient electrolyte were compared to two mono-functional structures, in which one laminate was bonded by epoxy only (maximum mechanical strength but no electrochemical function) and the other was with PEO (maximum ionic conductivity but low structural rigidity). These samples had two layers of QxTh-rGO@CF fabric and a cellulose separator sandwiched in between. The weak binding strength of PEO led to separation of the layers at 2.1 MPa when the structure was placed under tensile strain. The gradient structural supercapacitor remained intact up to the tensile stress of 167 MPa, and the epoxy laminate sustained 255 MPa before failure, as seen in Figure 3.15a. The tensile modulus, namely the slope of tensile stress versus applied strain, was 10.2 GPa for the structural supercapacitor.

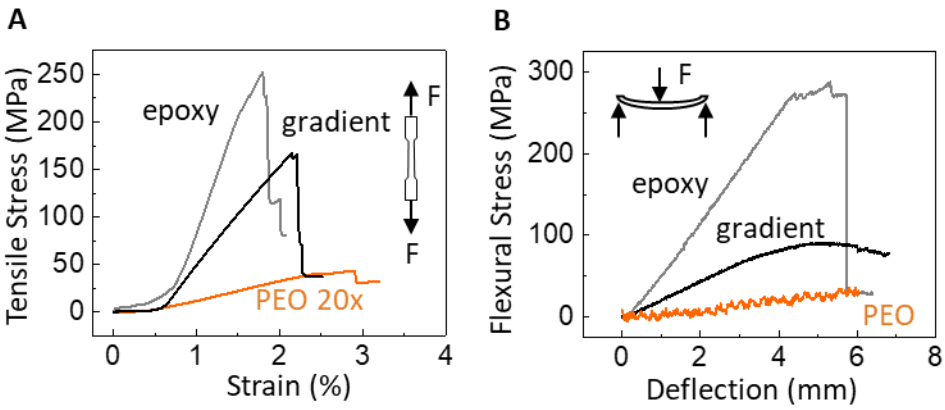

Figure 3.15. Mechanical properties of structural supercapacitors. (a) Tensile stress versus applied strain for laminates bonded by different polymers. For the stress measurement, the sample cross-sectional area was 0.58 mm × 2 cm and the length was 5 cm. (b) Flexural strength versus deflection distance. The device dimensions were 10 cm × 1 cm × 0.58 mm.

In Figure 3.15b, the flexural properties were measured by a three-point bending setup that applied deflection to determine stiffness. The PEO device was flexible and showed flexural stress < 20 MPa. In contrast, the flexural strength was 91 MPa for the gradient structural supercapacitor and 275 MPa for the epoxy laminate when the structures reached permanent deformation. This

high flexural strength is higher than the typical carbon fiber based structural supercapacitor[134], although slightly worse than the device with special honeycomb core separator design which is more difficult to fabricate.[135] For visual comparisons, the photographs in Figure 3.16 showed the stiffness of each sample with a thickness of 0.8 mm, where the PEO structure was severely bent under a 20 g weight, and the gradient electrolyte was able to support a 100 g weight, potentially strong enough as structural materials in electronic casings and internal parts of electric vehicles.[104–106] Since practical applications might require thick carbon-fiber reinforced composites, we have also measured the flexural stress of structural supercapacitors integrated with multiple layers of carbon fibers (8 electrodes with 7 separators) and observed that the flexural modulus was maintained (Figure 3.17). Therefore, it would be feasible to scale up and adapt the layered composites for different target thicknesses according to the desired use case.

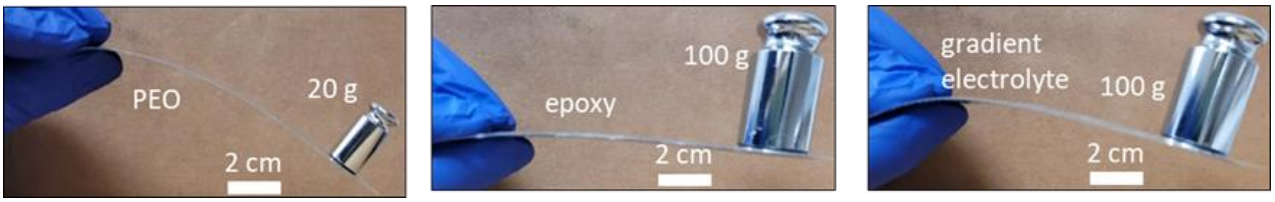

Figure 3.16. Photographs showing the deflection of laminates under weights. The film thickness was 0.8 mm including encapsulation PET films.

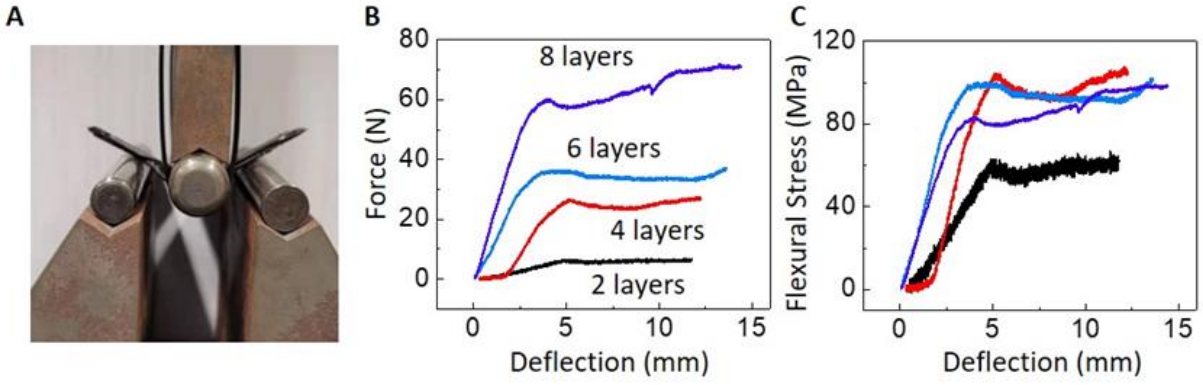

Figure 3.17. (a) Photograph of the flexural stress measurement. (b) Bending force vs deflection and (c) flexural stress vs deflection of structural supercapacitors with increasing layers of QxTh-rGO-CF electrodes.

Simultaneous monitoring of electrochemical and mechanical characteristics were carried out on the structural supercapacitor with the gradient electrolyte. An example was the cyclic voltammetry measurements as a function of applied deflection shown in Figure 3.18. From the current-voltage characteristics, the extracted capacitance was 47.1 mF in the initial flat state and 40 mF at 7 mm deflection, and thus the device retained 85% of its original capacitance even under large deformation. Figure 3.18b summarizes the series of in-situ measurements that concurrently tracked flexural stress and capacitance as the structural supercapacitor was subjected to increasing deflection. When the structural deflection was less than 3 mm, the device capacitance remained constant, and only when the deflection was 3 mm and beyond then the capacitance started to decrease, and leveling off to 85% of the initial capacitance as the structure reached its peak flexural stress after which it was irreversibly deformed. The characterization here indicated stable electrode-electrolyte interfaces in our structural supercapacitor to maintain electrochemical and mechanical performance as external mechanical loads were applied.

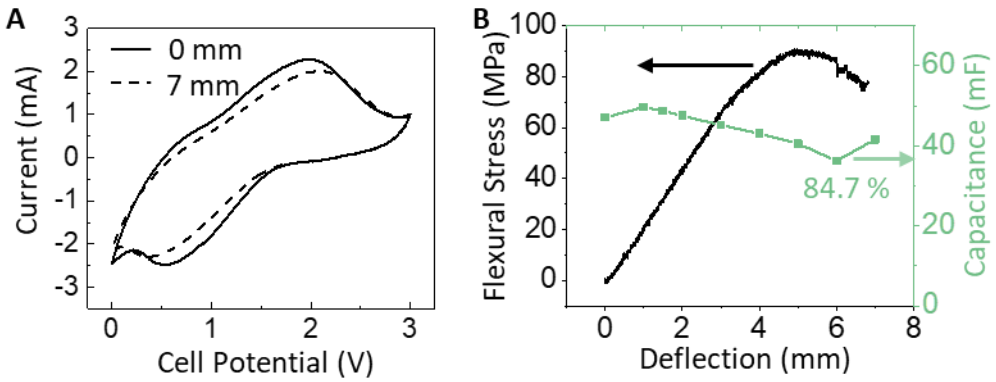

Figure 3.18. (a) Cyclic voltammetry at 20 mV s^{-1} of the structural supercapacitor with the gradient electrolyte, taken under the flexural deformation of 0 or 7 mm deflection. (b) Flexural stress and capacitance as a function of deflection distance, measured on the structural supercapacitor with the gradient electrolyte.

3.3.6 Multifunctional Efficiency of Structural Supercapacitors

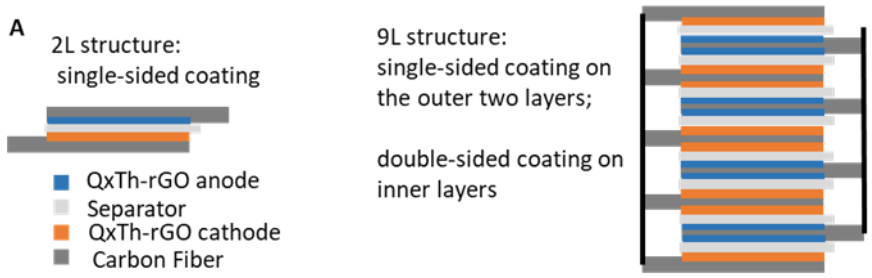

Figure 3.19. Structures of 2-layer (2L) and 9-layer (9L) supercapacitors.

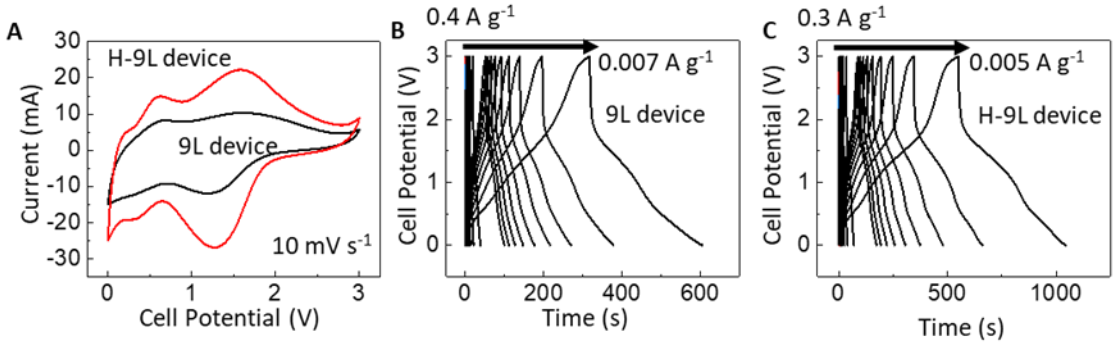

Figure 3.20. (a) CV characteristics of 9L and H-9L devices. The H-9L had twice the QxTh-rGO loading than the 9L device. (b) GCD curves from 0.007 A g^{-1} to 0.4 A g^{-1} of 9-layer structural supercapacitor with gradient electrolyte. (C) GCD curves from 0.005 A g-1 to 0.3 A g-1 of high-loading 9 layer structural supercapacitor with the gradient electrolyte.

For the fabrication of the 9L and H-9L structural supercapacitors, the electrodes included 2 single-sided cathodes, 3 double-sided cathodes, and 4 double side anodes (Figure 3.19). The total capacitances of the cathode and anode electrodes were made to match for balancing materials utilization. Before assembly, the electrodes were held at -0.5 V for 1 min to keep at a neutral state. The electrolytes were stencil printed on both sides of the electrodes (using type iii electrolyte in Figure 3.9) and the cellulose separators (with type ii electrolyte), then placed under vacuum to evaporate solvent and partially cured at 70°C for 1 hr. Then the device was assembled with following sequence: cathode-anode…cathode, where single-sided cathodes were used as the bottom and top layers of the device while double-sided electrodes were in between. Separators

were put between every pair of cathode-anode. In this stacking configuration, 8 pairs of cathode-anode were achieved with only 9 layers of carbon fibers, thus saving the mass and volume of 7 carbon-fiber layers compared to 8x 2L cells, which would use 16 layers of carbon fiber. The performance of the devices was showed in the Figure 3.20.

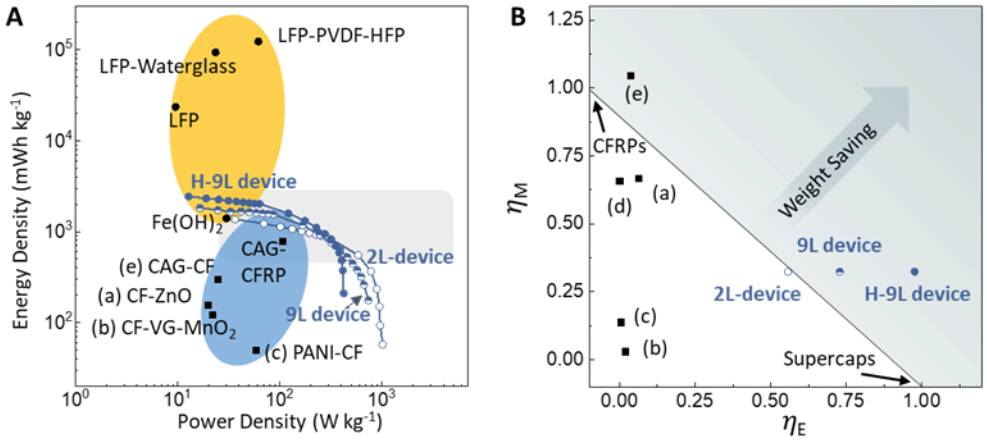

Figure 3.21. (A) Energy and power densities of structural energy storage devices. The shaded ovals categorize the devices into batteries (orange) and supercapacitors (blue). Our devices include a 2-layer (2L) structure, a 9-layer (9L) structure, and a high-loading (H-9L) structure. The light grey region represents the typical characteristics of mono-functional supercapacitors that cannot provide structural functions. Structural batteries: $Fe(OH)_2$[136]; $LiFePO_4$ (LFP)[112]; LPF-Waterglass[137]; LFP-PVDF-HFP[138]. Structural supercapacitors: (a) CF-ZnO[109]; (b) CF-vertical graphene (VG)-MnO_2[139]; (c) PANI-CF[140]; (d) graphene-CF[141] (0.07 mWh kg^{-1}, very small and thus not in the axis range); (e) carbon aerogel (CAG)-CF[142]. CAG-carbon fiber reinforced polymer (CFRP)[143], for which mechanical data is not available. (B) Multifunctional efficiency of state-of-the-art structural supercapacitors. Letter labels correspond to part A. Here η_E is the energy density ratio and η_M is the tensile strength ratio compared to mono-functional structures.

Figure 3.21 presents the energy and power densities of state-of-the-art structural supercapacitors and batteries in comparison to our devices. While batteries are generally expected to have higher energy density than supercapacitors, our structural supercapacitor exceeded the energy density of the $Fe(OH)_2$ structural battery[136] and achieved much larger power density than all the other structural energy storage devices. Our device metrics were calculated with the total device mass including electrodes, separator, and electrolyte. We fabricated three device structures: one with two electrode layers (2L), another with nine electrode layers (9L), and a third device with

nine electrode layers and a higher loading of QxTh-rGO (H-9L). The 2L device was a basic structure with QxTh-rGO deposited on a single side of each CF layer. It was able to provide 57.5 mWh kg^{-1} at 1019 W kg^{-1} power density. However, considering that the CF substrate contributed a large portion of the electrode mass but little capacitance, there was room to improve the device design by depositing the high-capacitance QxTh-rGO on both sides of each CF and stacking the anodes and cathodes as shown in Figure 20 to minimize the CF mass. This arrangement was used in the 9L device, which theoretically would have a charge-storage capacity equivalent to 8x 2L devices while eliminating the mass of 7 CF substrates. Thus the gravimetric energy density may increase by 1.78 fold (= 16/9) for the 9L device compared to the 2L device.

Indeed, the measurements in Figure 21a showed higher energy densities for the 9L device than the 2L one, although the power output was comparatively decreased for the 9L structure, probably due to a small resistance increase introduced by stacking electrode current collectors. For the third device labeled H-9L, we roughly doubled the QxTh-rGO loading on each CF substrate compared to the 9L device. The H-9L device showed a lower power density than 9L device because of the slower kinetics from the thicker QxTh-rGO coating. Nonetheless, the H-9L device still offered power density within the same order of magnitude as mono-functional supercapacitors.

To quantify the potential advantages of multi-functional structures over mono-functional counterparts, there have been different approaches[144–146] to combine the structural and electrochemical properties and tie them into a multi-functional efficiency metric η_{multi} defined as

$$\eta_{multi} \equiv \eta_E + \eta_M = \frac{E_{multi}}{E_{typ}} + \frac{M_{multi}}{M_{typ}} \quad \text{(Equation 3.1)},$$

where η_E and η_M are the electrochemical or mechanical efficiency, respectively, and each of them is computed by comparing the specific electrochemical properties E_{multi} (such as energy and power, etc.) or specific mechanical properties M_{multi} (such as strength, stiffness, toughness, etc.)

of the multi-functional laminate relative to baseline values E_{typ} or M_{typ} from typical mono-functional structures. If η_{multi} is greater than 1, it indicates weight savings over conventional systems of using independent mono-functional components. In the analysis in Table 3.3, we simplified Equation 3.1 to consider only energy density for η_E and only tensile modulus for η_M. One of the reasons we simplified Equation 1 to use only tensile modulus is because of limited mechanical data in other reports. While this may be over-simplifying, it provided a useful perspective for materials comparison. It is worth noting that Equation 3.1 as written assigns an equal weight (50% each) to the roles of structural support and energy storage. If in future systems those roles are not equally important, the multifunctional efficiency can be adjusted by assigning different scaling factors to each property.[145]

Table 3.3. Energy density and tensile modulus of state-of-the-art structural supercapacitors. The efficiency η_E was calculated with E_{typ}= 2.5 Wh kg^{-1} and η_M with M_{typ}= 31.5 GPa. The letter labels correspond to those in Figure 4B. VG: vertical graphene; PANI: polyaniline; CAG: carbon aerogel.

Electrode materials [reference #] (label)	Energy density (mWh kg^{-1})	Tensile modulus (GPa)	η_E	η_M	η_{multi}
2L QxTh-rGO-CF (this work)	1369	10.2	0.548	0.324	0.872
9L QxTh-rGO-CF (this work)	1823		0.729		1.053
H-9L QxTh-rGO-CF (this work)	2443		0.977		1.301
CF-ZnO [109] (a)	156.2	21	0.062	0.667	0.729
CF-VG-MnO_2 [139] (b)	12.2	4.313	0.0049	0.137	0.142
PANI-CF [140] (c)	49.4	0.907	0.020	0.0288	0.0485
Graphene-CF [141] (d)	0.0664	20.72	2.66×10^{-5}	0.658	0.658
CAG-CF [142] (e)	93	32.9	0.037	1.045	1.082

Regarding the benefit of multi-functionality, we compared our device to state-of-the-art structural supercapacitors listed in Table 3.3, where the efficiency metrics were calculated based on the baseline values of E_{typ}= 2.5 Wh kg^{-1} for energy density[51] and M_{typ}= 31.5 GPa for tensile

modulus[98] from mono-functional standards. Because η_E and η_M are ratios and by definition dependent on the denominator values and yet there are no consistent baseline values across publications, we normalized the prior works in Table 1 with the common baseline values chosen here to be fair in the analysis.

The η_E of our structural supercapacitors with gradient electrolyte was 0.548 for the 2L device, 0.729 for 9L, and reached 0.977 for the H-9L device, the highest among the structures in Table 1. This high η_E was attributed to the high gravimetric capacitance of our electrode, the good ionic conductivity from the gradient electrolyte, and the multi-layer stacking configuration for mass savings. Here the stacking configuration with double-sided coating for each current collector has been used in mono-functional batteries, which motivated us to try such designs for structural supercapacitors. The η_M of our devices was 0.324 with the epoxy-reinforced design. The tensile modulus was measured for the 2L device, and we assume it to remain the same for multi-layer configurations, as shown in Supplemental Figure S9. The total η_{multi} was found to be 1.053 for the 9L device and 1.301 for H-9L, meaning that our structural supercapacitors would offer a weight-saving advantage and provided the highest multifunctional efficiency to the best of our knowledge. Also note that in Figure 21b all the prior works were clustered in the region with very low electrochemical efficiency η_E. Our structural supercapacitor designs with η_E up to 0.977 were in the region with high electrochemical efficiency. Thus, while our devices would offer structural support with decent mechanical efficiency η_M, they contribute more heavily to electrochemical functions and η_E. This unique position would be complementary to prior structural supercapacitors and well-suited for applications in which energy capacity is very critical to their missions.

3.4 Prototype Based on the Structural Supercapacitor: Electric Boat Powered by an Energy-Harvesting System

3.4.1 Fabrication of Prototype structural supercapacitor boat

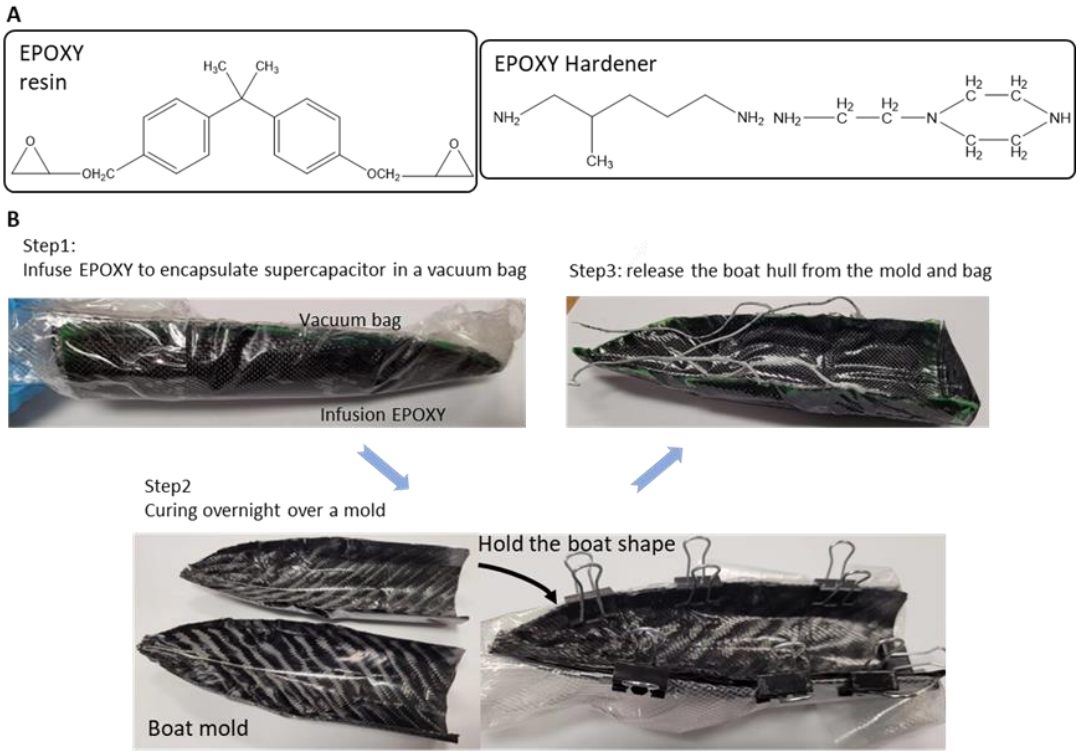

Figure 3.22. (a) The chemical structures of infusion epoxy for sealing the structural supercapacitor boat hull. (B) Sealing process to encapsulate the structural supercapacitor. After curing overnight at room temperature, boat hull was released from the mold and vacuum bag.

For the model boat prototype, the boat hull was fabricated from a laminate of partially cured structural supercapacitor, prepared by pressing together the electrodes and cellulose separator coated with electrolyte resins for bonding. The partially cured laminate was pressed against a mold to shape the workpiece into a hull form, and it was left in vacuum overnight to remove residual solvents. Afterwards, it was annealed at 70°C for another two hours, and the fully cured structural supercapacitor hull was released from the mold. The hull was encapsulated by sandwiching it between two pieces of CFRP and bonded to the hull by a layer of epoxy (Figure 3.22). The boat hull was connected to the leads of the control circuit by copper wires attached with silver

conductive tape. The control circuit was soldered to a solar cell (3V 20 mA output, Sundance Solar Products) and a DC coreless motor (3.7 V, 30000 rpm, XYDA0015N, Augiimor Inc.). The circuit components were placed inside the boat hull, while the motor shaft was mounted to the bottom of the boat on the CFRP encapsulation for driving the propeller outside the boat hull.

3.4.2 Control Circuit Design for the Self-powered Boat

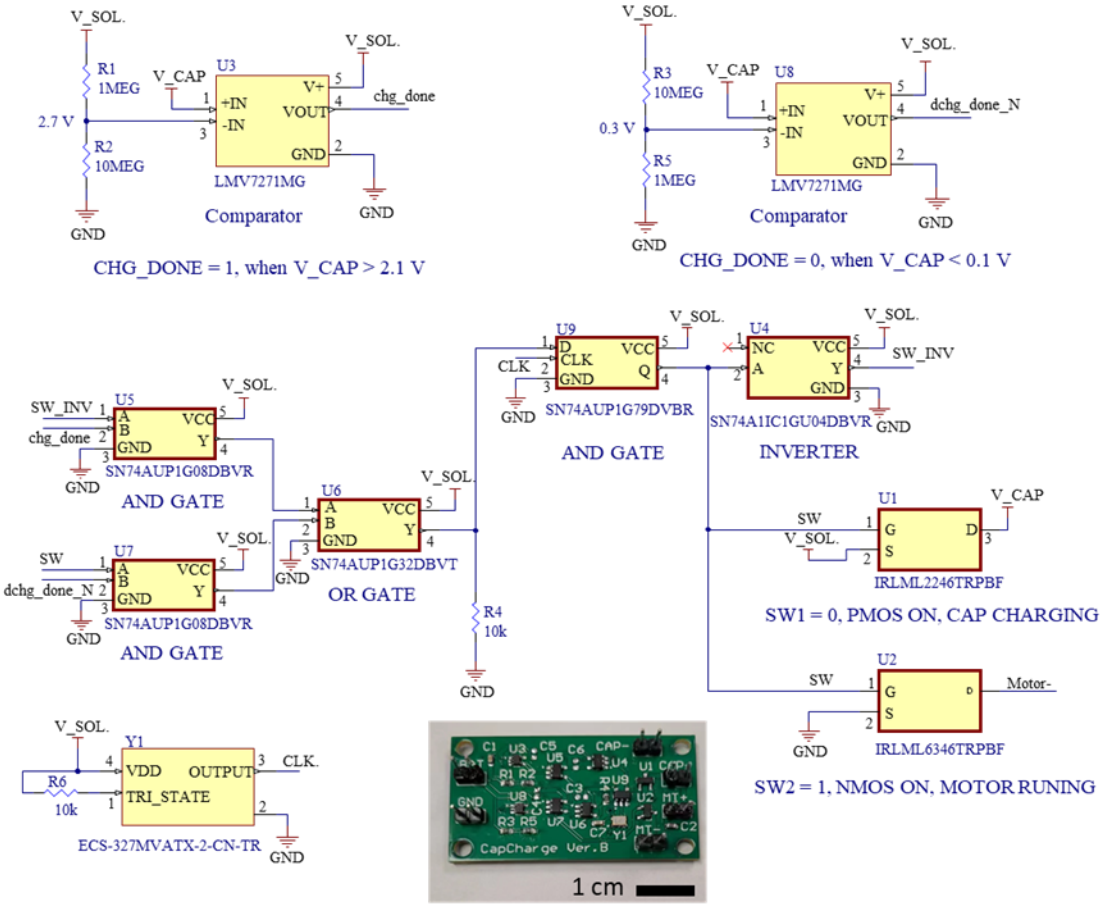

Figure 3.23. Diagram and photograph of the control circuit for the boat demonstration. Power consumption was 200 uW for the whole circuit.

A finite-state-machine (FSM) circuit was designed to control the logic of the system. The FSM had two states: 0-charging and 1-discharging. The FSM was implemented using simple discrete logic gates and flip-flops (Supplemental Figures S12 and S13). A 32.768 kHz crystal oscillator

(ECS-327) was used to provide clock for the digital circuit. Upon power-on, the circuit initialized with state-0, the transistor PMOS U1 (IRLML2246) between the solar panel and the supercapacitor was turned on, and the charging process began. A comparator (LMV7271) was used to compare the supercapacitor voltage *v_cap* with the charging threshold voltage *v_high* and sent a *charge-done* signal when *v_cap* > *v_high*. When *charge-done* signal was high, the circuit switches to state-1 upon the next rising edge of the clock. Consequently, the transistor NMOS U2 (IRLML6346) between the supercapacitor and the motor was turned on, U1 was turned off, and the discharging process began. Similarly, another comparator compared the *v_cap* with the discharging threshold *v_low* and sent a *discharge-done* signal when *v_cap* < *v_low*. The circuit would switch back to state-0 in the next clock cycle, and the process continued so on and so forth unless the circuit was switched off.

3.4.3 Operation and Performance of Self-powered Boat

After device characterization, our structural supercapacitor design was applied in a proof-of-concept demonstration. Motivated by the pervasive use of carbon-fiber laminates in boat building, we fabricated a model boat for which the entire hull was consisted of structural supercapacitors serving dual functions of structural support and energy storage for powering the boat motor in Figure 3.24a.

The boat-hull supercapacitor was integrated into an energy-harvesting system with a solar cell that was as the sole energy input for the boat. A control circuit automatically toggled the connections of the supercapacitor to be charged by the solar cell or to be discharged to power the boat motor. Upon power-on, the control circuit would be in the charging mode until the supercapacitor reached the threshold voltage of 2.1 V. Once the supercapacitor voltage exceeded the set threshold, the control circuit switched to the discharging mode, in which the supercapacitor

sent current to turn on the motor, and the boat cruised over water as seen in the Supplemental Video SV1. When the supercapacitor voltage dropped to 0.1 V, the control circuit switched back to be in charging mode, and the charging/discharging process would repeat as seen in Figure 3.24b till the circuit was turned off. The capacitance of the boat-hull supercapacitor was 2.72 F; it allowed 1.9 minutes of motor run time after 4.8 minutes of charging under the mid-afternoon sun. For the operational voltage between 0.1 V and 2.1 V, the structural supercapacitor was tested for 35,000 charge-discharge cycles and retained 83% of its initial capacity, demonstrating excellent stability and long cycle life. This demonstration shows the supercapacitor capable of meeting the structural and energy storage requirements of an autonomous energy harvesting system operating in aquatic environments.

Figure 3.24. (a) A schematic and photograph of a boat model, in which the entire boat hull is a structural supercapacitor. The structural supercapacitor was charged by solar cells to power the boat motor. (b) Charging/discharging voltage at the supercapacitor terminals versus time when operating within the energy harvesting system to drive the boat motor.

3.5 Conclusion

This work presents a new design for structural supercapacitors to overcome the bottlenecks at electrode and electrolyte interfaces. The electrode coating of pseudocapacitive QxTh-rGO with a wide potential window of 3 V substantially raised the gravimetric energy and power densities, and the conjugated polymer strengthened the electrode tensile properties better than particulate materials with weaker adhesion to carbon fibers. The electrolyte was reinforced by solid PEO to

maintain ion percolation without resorting to liquid ion channels, and the epoxy-PEO-$TEABF_4$ resin was optimized to be functionally graded from the electrode to the separator interfaces, transitioning from a composition with high ionic conductivity near the electrodes to one with high mechanical strength at the separator for load transfer. This gradient configuration would be useful for others working on non-flammable solid electrolytes to enhance the device performance and safety.

Here the structural supercapacitors were shown to achieve state-of-the-art performance with an energy density of 2.443 Wh kg^{-1} at the power output of 12.8 W kg^{-1} and a tensile modulus of 10.2 GPa. The gradient design pushed the maximum power density (1019 W kg^{-1}) into the same range as mono-functional supercapacitors, an important milestone for structural energy storage devices. The in-situ mechanical-electromechanical measurements established the device durability under mechanical loads, as the structure retained 85% capacitance at 80 MPa flexural stress. The flexural strength of 91 MPa and tensile strength of 167 MPa are sufficient for many electronic housings. After 10,000 full charge-discharge cycles over 3 V, the capacity retention was 84%, and such long cycle life ensures that structural parts would not need to be replaced frequently.

Lastly, this work demonstrated the feasibility and benefits of using structural supercapacitors in a prototype boat. The structural supercapacitors were molded as a boat hull that realized weight and space savings and carried the entire energy-harvesting system. The hull stored the energy harvested by the on-board solar cell and in turn powered the boat motor. This autonomous system showed the utility of structural supercapacitors to serve as energy reservoirs for renewable energy sources. Here the high-performance structural supercapacitors can extend the energy capacity to make electrified vehicles more compact and extend the operational time of electronics, adding a promising approach towards the goal of energy sustainability.

Chapter 3, in part, is a reprint of the material as it appears in Science Advances. Kai Zheng, Nandu Koripally, Naresh Eedugurala, Jason D Azoulay, Xinyu Zhang, Tse Nga Ng. Structural pseudocapacitors with reinforced interfaces to increase multifunctional efficiency. The dissertation author was the primary investigator and first author of the paper.

CHAPTER 4: ION-EXCHANGE SEPARATOR SUPPRESSING SELF-DISCHARGE IN POLYMERIC SUPERCAPACITOR

4.1 Introduction of Self-discharge Problem of Supercapacitor

Energy storage devices are critical components that provide stable power for wireless electronics. While batteries are the dominant form of energy storage, supercapacitors offer superior cycle life and high power densities[123,147–150] and are being explored as alternatives to batteries, especially in settings that only require short-term energy storage, for example when integrated with environmental energy harvester. However, the self-discharge processes[151] in supercapacitors have caused large potential decay and leakage current (Figure 4.1), resulting in loss of stored energy and low charging efficiency. Thus, it is crucial to understand and mitigate self-discharge phenomena in supercapacitors in order to take advantage of their potential as energy reservoirs with ultra-long cycle life.[64]

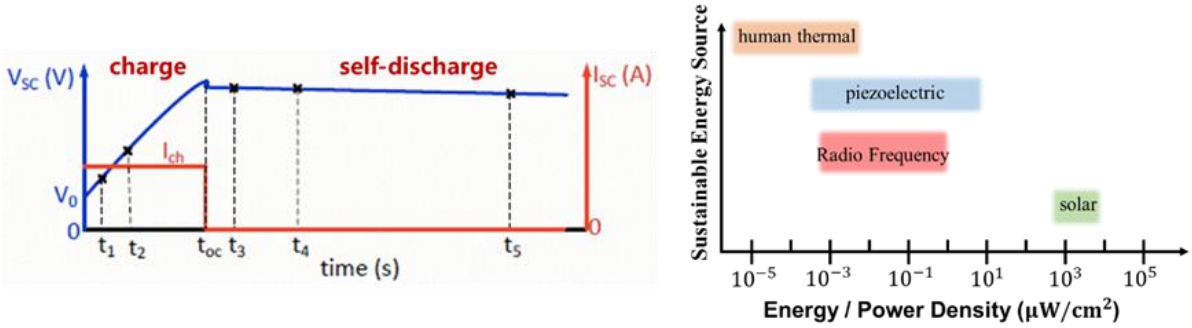

Figure 4.1. Scheme of typical self-discharge process of supercapacitors.[152]

When charged, a supercapacitor is in the high energy state, and thermodynamically the device would discharge to a lower energy state whenever there is a pathway. The self-discharge pathways are categorized into three types: charge redistribution, ohmic leakage, and Faradaic reactions.[153] Ohmic leakage and charge redistribution (Figure 4.2) have been well studied[151,154] and are now sufficiently suppressed to be a minor contributor to self-discharge processes, but the Faradaic reaction mechanism (Figure 4.3) remains a challenging issue because of the difficulty in

pinpointing side reactions, which could vary between electrode materials, electrolyte ions, and unintentional impurities from different sources.

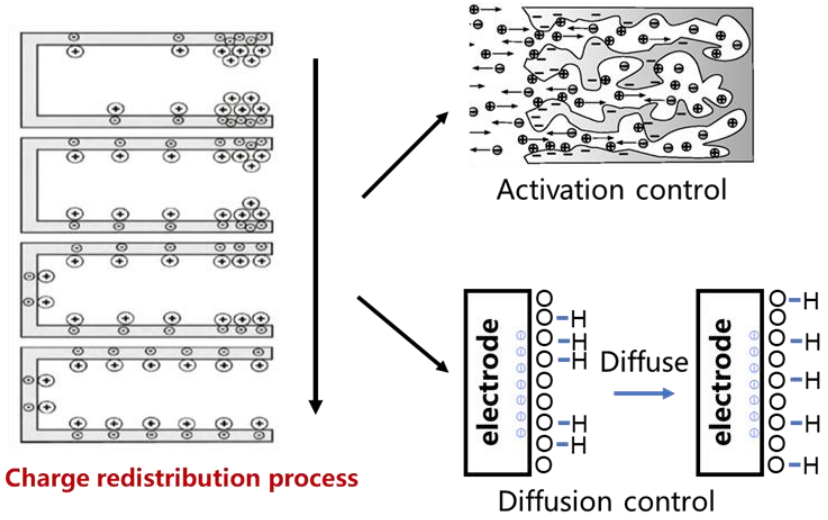

Figure 4.2. Scheme of charge redistribution mechanism of self-discharge process.[155]

Recent research to minimize Faradaic self-discharge include modifying the electrode surface with a blocking layer,[156] and using liquid crystal additives in the electrolyte to impede the diffusion of redox species near the electrodes.[157] However, these approaches are not selective between electrolyte ions and redox impurities, and so the reduced self-discharge from limiting diffusion comes at a cost of lower rate performance and capacitance decrease. Alternatively, the use of a proton exchange separator[158] or a novel solid-state electrolyte[159] to confine cations have suppressed self-discharge, but these designs are specific for their material systems.

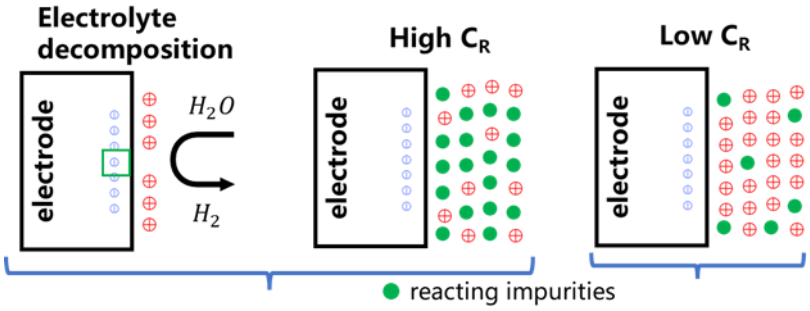

Figure 4.3. Scheme of Faradic reaction self-discharging mechanism of supercapacitors.

Building on the concept of trapping impurities to minimize Faradaic reactions, this chapter demonstrate a versatile separator design that is generally applicable to aqueous and organic electrolytes while maintaining the device capacitance and rate performance. In the modified separator, we incorporated a cation-exchange resin that is typically used for waste water treatment to remove transition metal ions. For our purpose, the resin suppressed the movement of redox impurities in the electrolyte by binding them to the polymer matrix, and in exchange releasing an equivalent number of the resin cations back to electrolyte. In this way the impurities are collected in the separator without impeding electrolyte diffusion to keep up the device performance. The temperature dependence of the potential decline is monitored over 10 hours and fitted to self-discharge models, to understand the self-discharge kinetics and compare thermal activation energies in devices with different separators.

4.2 Ion-exchange Separator Fabrication and Characterization

Three types of separators were inserted between the electrodes to study how separator materials influence the supercapacitor performance and self-discharge characteristics. Figure. 4.4 shows the molecular structures of separator materials as denoted by their commercial brand names. Celgard^{TM} is a porous film made of polypropylene (PP), designed to block electron transport but allow ionic diffusion. Nafion^{TM} is a fluoropolymer backbonewith sulfonate groups (sPTFE) that allow high proton conductivity. PP and sPTFE are routinely used as separators in energy storage devices including batteries, supercapacitors, and fuel cells. Purolite^{TM} is a polystyrene resin with sulfonate end groups (sPS), which show the highest cation adsorption capacity among ion-exchange functional groups (capacity of adsorbing 12 mg of ions per gram of sPS resin),[160–162] and is mainly used to separate heavy metal ions in water treatment. Here we repurposed it for retarding redox impurities in the separator to minimize unwanted reactions in supercapacitors.

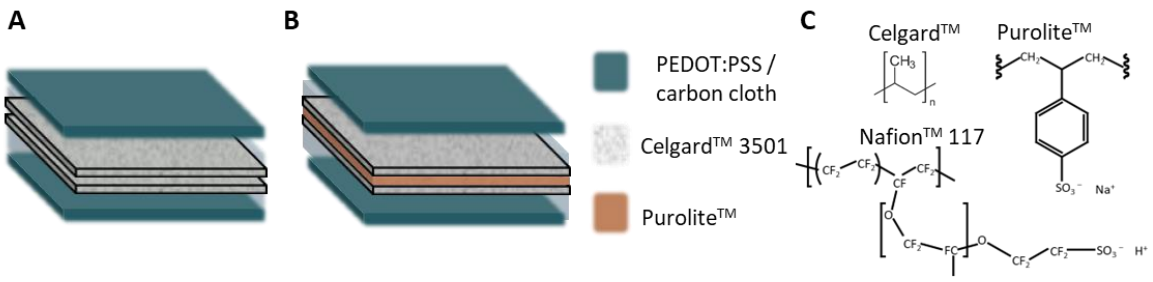

Figure 4.4. Molecular structures of separator materials. Schematics of supercapacitor structures with separators consisting of sPS+PP.

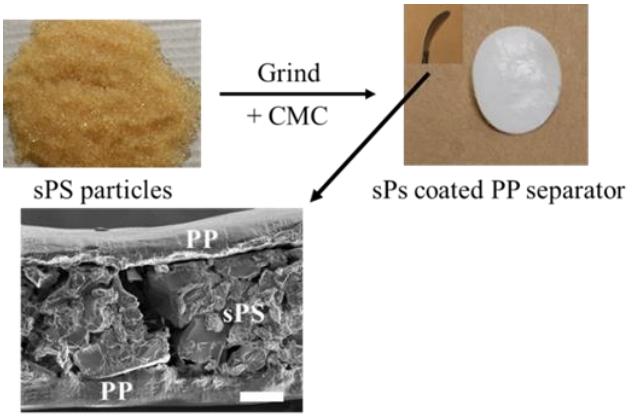

Figure 4.5. (a) sPS+PP: Purolite™ sandwiched between two Celgard™ films and (b) PP: only two Celgard™ films.

Celgard™ 3501 (Porosity 55%, pore size 65 nm) and Nafion™ 117 (Chemours) were used as purchased and were 25 μm and 183 μm in thickness, respectively. The films were cut into circular pieces with 0.5 cm diameter by using a hole puncher. To prepare the separator with Purolite™ CE100, a solution of the Purolite™ resin, sodium carboxymethyl cellulose (CMC) (Sigma, molecular weight: ~9000), and deionized (DI) water was put together at a weight ratio of 1.8:0.2:8, and the mixture was then grinded into a slurry in an agate mortar. A 100 μL aliquot (~18 mg Purolite) of this slurry was drop-cast on a 1.3 cm^2 piece of Celgard™ film. Then another piece of Celgard™ film was placed on top and dried at 60℃ for 10 min. The CMC acted as a binder to glue the two films together to form a separator stack (sPS+PP) as shown in Figure 4.5a. In the

future, the sPS layer can be tuned to a lower thickness if desired, by reducing the Purolite particle size and amount in the slurry. For comparison, the other separator stacks in this work were a single sPTFE film (183 μm in thickness) or two PP films (each 25 μm in thickness) without the sPS layer (Figure 4.5b).

Figure 4.6. A photograph of a supercapacitor pouch cell.

Supercapacitors with different separators were made into pouch cells (Figure 4.6). The supercapacitors were fabricated using the redox-active polymer poly(3,4-ethylenedioxy-thiophene) (PEDOT) on carbon cloth current collectors. PEDOT is a mixed ionic and electronic conductor[17–21] with high stability[22] in supercapacitors. All the materials in our supercapacitor designs are flexible and compatible with low-cost printing fabrication for IoT and wearable applications.[15,23–26]

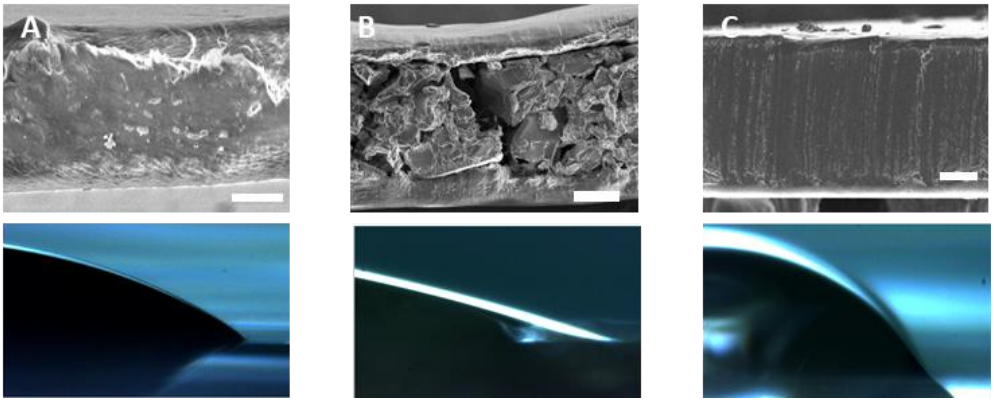

Figure 4.7. For (a) PP, (b) sPS and (c) sPTFE, the top row shows SEM images of the film cross-sections. Scale bars: (a) 5 μm; (b) 50 μm; (c) 50 μm. The bottom row displays photographs of water contact angle measurements on the surface of the corresponding separator materials.

The water contact angle measurements in Figure 4.7 shows the hydrophobicity of the separator materials, with sPTFE (56°) > PP (34°) > sPS (21°). The molecular structure of sPS has a high volume ratio of hydrophilic functional groups to the polymer backbone, thus increasing hydrophilicity and contact with aqueous electrolytes. The scanning electron microscopy (SEM) image in Figure. 4.7a displays that the sPS layer was roughly packed. For the separator stack in Figure 4.5a, the dense columnar structures in PP films (Figure 4.8) encased the sPS layer to form an electrical insulator with pathways for ionic diffusion. The next two sections compare the supercapacitor characteristics as a function of time and temperature, to determine the self-discharge mechanisms and kinetics in these devices with different separators.

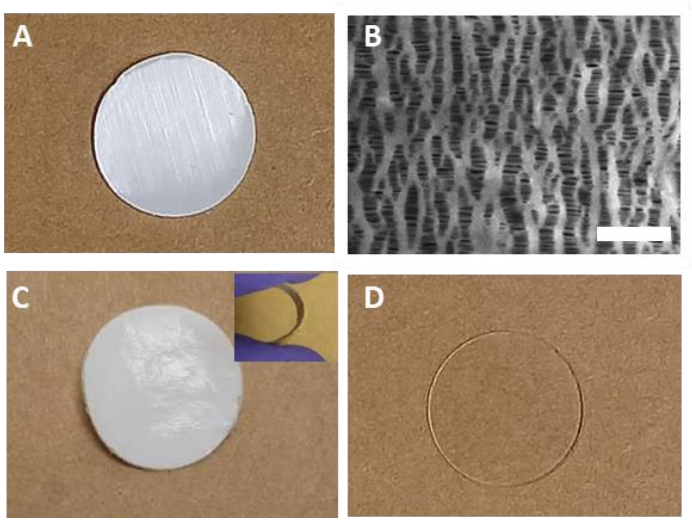

Figure 4.8. (a) Optical photograph of the commercial polypropylene (PP) separator (Celgard™ 3501). (b) SEM image of the PP film surface. Scale bar: 2 um. c) Optical photograph of the sPS+PP separator. The inset shows the separator being bendable. d) Optical photograph of the Nafion™ 117 separator. The diameter of each sample is 1.3 cm.

4.3 Electrochemical Performance of Fabricated Supercapacitor

Given that the electrodes and electrolyte were the same across the devices, the differences in cell performance are attributed to the separators. The cyclic voltammograms in Figure 4.9 indicate similar current-voltage characteristics in supercapacitors with PP and sPS+PP separators, and these devices showed higher current than the one with sPTFE. In Figure 4.10, the equivalent series

resistance (ESR) was worst in the device using sPTFE, followed by sPS+PP and then PP, although the ESR difference in devices with or without sPS was only 0.5 Ω. The PS layer did not affect the device performance at low charge/discharge rate.

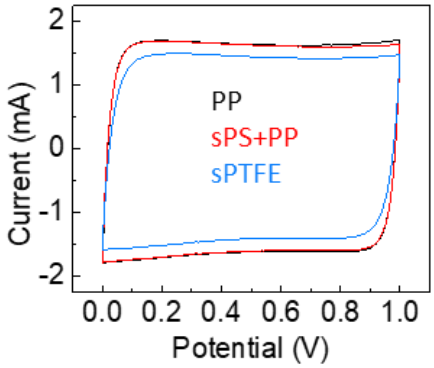

Figure 4.9. Performance comparison of supercapacitors with different separators: PP (black), sPS+PP (red) and (f) sPTFE (blue). Current versus voltage, at a scan rate of 50 mV/s.

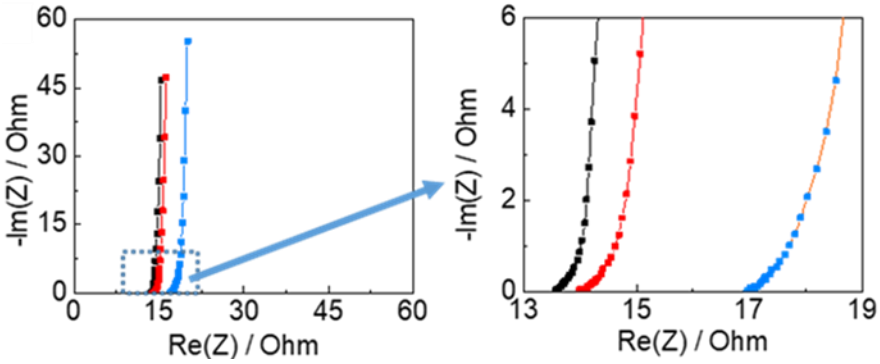

Figure 4.10. Performance comparison of supercapacitors with different separators: PP (black), sPS+PP (red) and sPTFE (blue). Imaginary versus real impedance. The right plot zooms in on the high-frequency region.

For instance, in Figure 4.11a at a current density of 0.125 A/g, the galvanostatic charge-discharge (GCD) curves were found to be the same for the supercapacitors with PP only and with sPS+PP. As the charge/discharge current density was increased to 5 A/g in Figure 4.11b, larger IR drops were observed and correlated to the ESR trend. GCD curves in Supplemental Figure 4.12 were used to calculate the capacitance in Figure 4.11c by the relation $C = I/(dV/dt)$, where I is the discharge current, and dV/dt is the voltage change measured per recording time interval. The device

with sPS+PP showed as much as 1.5 times higher capacitance than the one with sPTFE. When compared to the control device with PP only, the device with sPS+PP demonstrated similar capacitance, with at most 10% decrease as the charge/discharge current density was raised to 0.5 A/g. Thus, the rate performance of supercapacitors was not significantly impacted by incorporating a sPS layer.

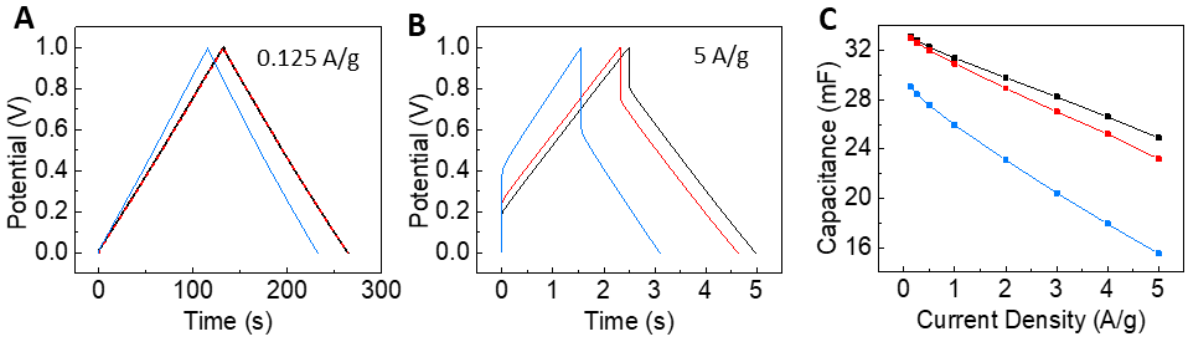

Figure 4.11. Performance comparison of supercapacitors with different separators: PP (black), sPS+PP (red) and sPTFE (blue). (a) Galvanostatic charge-discharge characteristics with constant current at (a) 0.125 A/g, (b) 5 A/g. (c) Capacitance versus charging current density.

In typical use cases, supercapacitors are charged by a current input, and when the desired voltage is reached, the charging current is switched off. Then the device is placed in the open-circuit condition to hold its energy, to be discharged only as needed. However, self-discharge processes may occur within the cell, leading to a reduction in the device potential. From the time at which charging was stopped (denoted as t_{oc} in Figure 4.13), the potential of the supercapacitor was periodically measured, and the cell voltage was shown to decay over time in Figure 4.14a. The potential decay increased as the charging current density was raised from 0.125 A/g to 0.5 A/g (Figure 4.15). The potential retention was the best in the device with sPS+PP, with its voltage maintained at 91% of the initial value after 30 min; the voltage in devices with PP and sPTFE decreased to 86% and 84%, respectively.

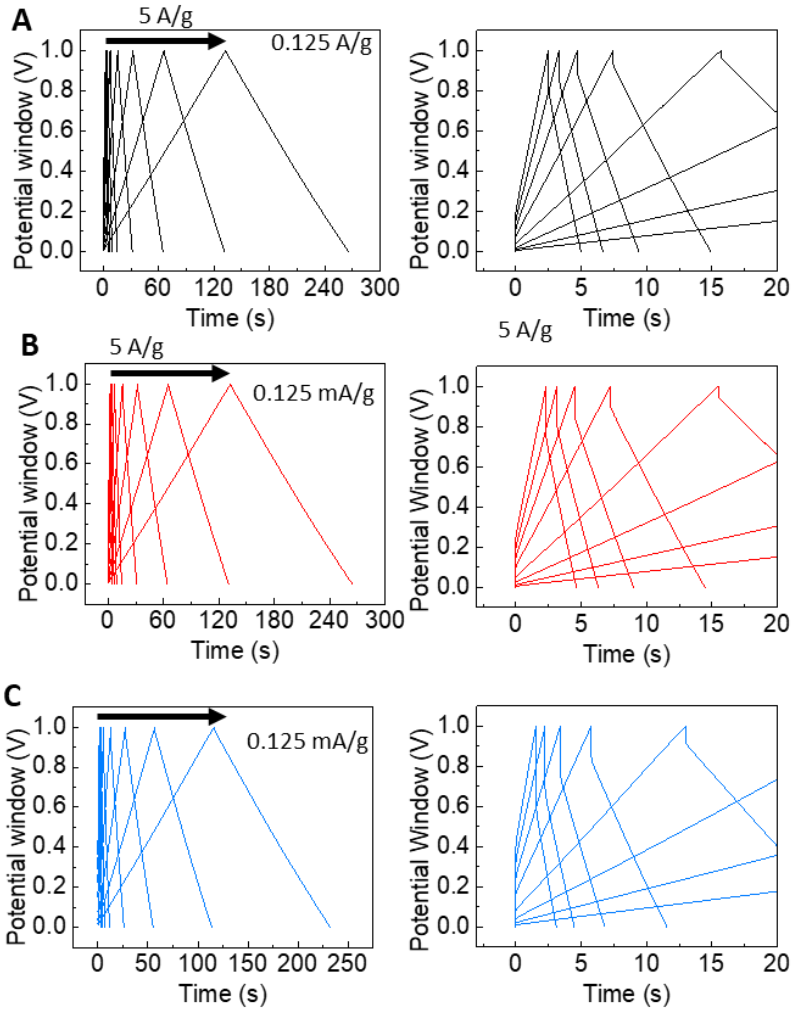

Figure 4.12. Galvanostatic charge-discharge curves of devices with the separator of (a) PP, (b) sPS+PP, and (c) sPTFE. The current inputs are 0.125, 0.25, 0.5, 1, 2, 3, 4, and 5 A/g. The right column are zoomed in views of the curves at high current density (from 5 A/g to 1 A/g).

The potential decay due to self-discharge affects the device energy densities. Figure. 4.14b reveals that initially the supercapacitor with the PP separator was the most energy dense, owing to its ESR being the lowest among the devices. But after 30 min of holding in open circuit, the retained energy of the device with sPS+PP surpassed the one with PP only. The additional sPS layer was essential in suppressing energy dissipation due to self-discharge.

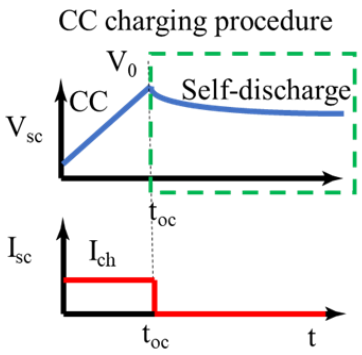

Figure 4.13. Schematic of the self-discharge measurement, in which a constant current (CC) is applied to reach the end potential V0 and subsequently the change in voltage due to self-discharge is monitored starting at time toc.

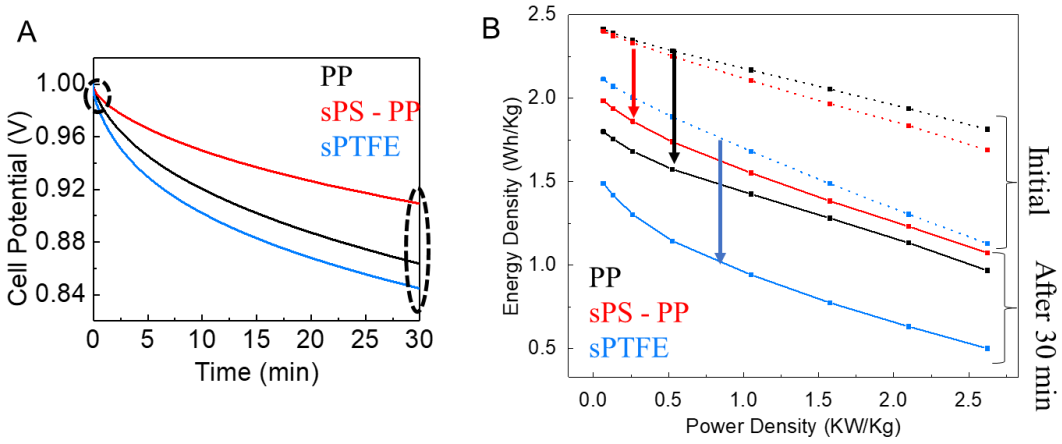

Figure 4.14. (a) Self-discharge characteristics versus time, after charging at a constant current density of 0.5 A/g to a terminal potential of 1 V. The electrolyte was 1M KCl in deionized water. (b) Energy densities versus power densities, before and after 30 min of self-discharge.

The energy densities reported in Figure 4.14b are comparable to prior works[166,167] using PEDOT as Faradaic electrodes (Figure 4.15). The notable point here is that the voltage decay was greatly reduced by modifying the separator. Because the device with sPTFE showed the lowest energy density and rate performance, and its voltage also degraded the most during the open-circuit interval, sPTFE was not included in further analysis.

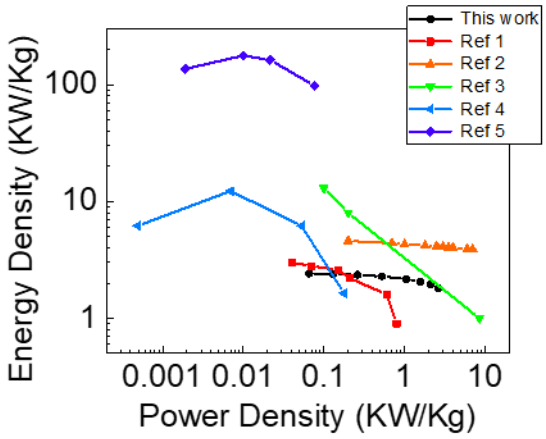

Figure 4.15. Energy density versus power density in previously reported PEDOT composite supercapacitors and in this work (black markers). Ref 1 (red): PEDOT:PSS/CNT[163]; Ref 2 (green): PEDOT[164]. Ref 3 (light blue): Commercial double-layer supercapacitor.[165] Ref 4 (dark blue): Li-ion battery.[165]

4.4 Self-discharge Mechanisms in Ion-exchange Separator

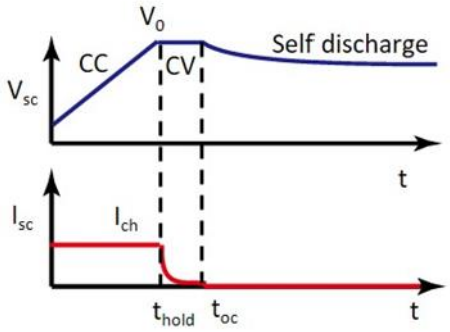

Figure 4.16. Schematic of the self-discharge measurement with a constant potential hold before self-discharge is monitored starting at time t_{oc}.

To understand how the sPS layer improved voltage retention, we recorded the change in cell voltage over time at various temperatures and test the data against self-discharge models.[153,168] Here the charging method included a hold at the terminal voltage, as seen in Figure 4.16. This constant voltage (CV) segment was introduced to eliminate self-discharge due to charge redistribution. Charge redistribution occurs when there is a charge gradient from the surface to the bulk of the electrode materials;[155] but by applying a 1-hr CV hold, charge inhomogeneity in electrodes would have sufficient time to equilibrate and become negligible. In this way we

excluded effects of charge redistribution and focused on self-discharge mechanisms due to Faradaic reactions.

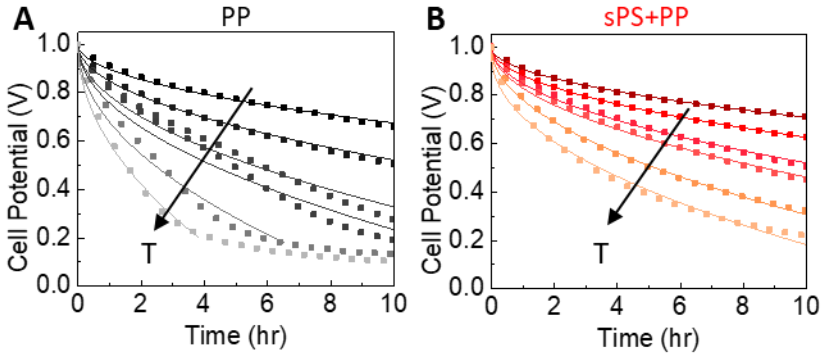

Figure 4.17. Comparison of self-discharge mechanisms in supercapacitors using PP (black) and sPS+PP (red) separators. (a, b) Self-discharge characteristics at different temperatures (T = 0, 22, 30, 40, 50, or 60 °C). The solid lines represent fitting results to Equation 4.1.

Figure 4.17a and Figure 4.17b display the change in voltage over ten hours in devices with PP and sPS+PP separators, after they were charged to 1 V and held at this terminal voltage for one hour. The data are fitted to the equation below, which was derived in Reference [153] to relate the potential change to activation-control or diffusion-control Faradaic reactions (Figure 4.18):

$$V(t) = V_0 - a\ln(t+b) - m\sqrt{t}\ , \text{(Equation 4.1)}$$

where t is time, V_0 is the initial voltage at the start of the open-circuit condition, the term $a\ln(t+b)$ is due to overpotential activation of decomposition reactions that discharge electrodes, and the term $m\sqrt{t}$ is related to diffusion-limited side reactions caused by a low concentration of redox impurities.[153] Based on Equation 4.1, if the origin of self-discharge is dominantly activation-controlled reactions, there would a linear relationship between V and ln t. On the other hand, if the self-discharge mechanism is diffusion-controlled, the plot of V versus $\sqrt{t}$ would be linear.

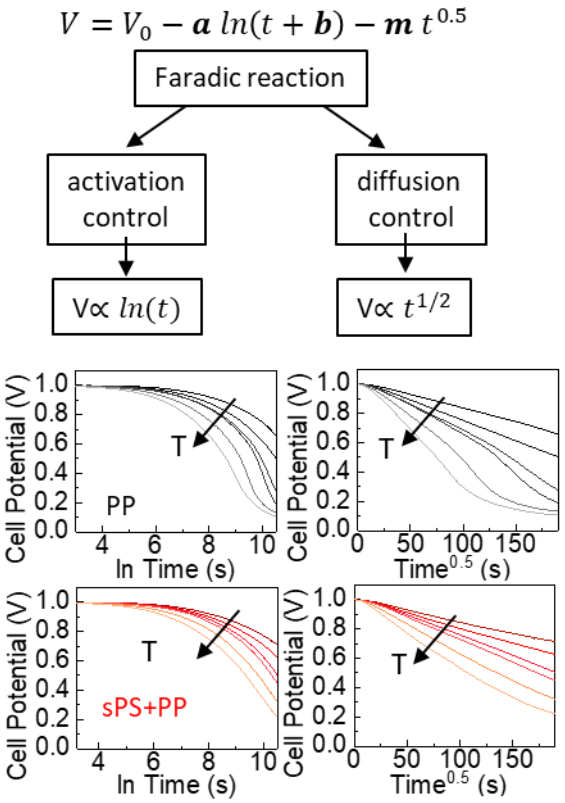

Figure 4.18. Comparison of self-discharge mechanisms in supercapacitors using PP (black) and sPS+PP (red) separators. Relationship of potential versus time, as a function of ln t or $t^{0.5}$.

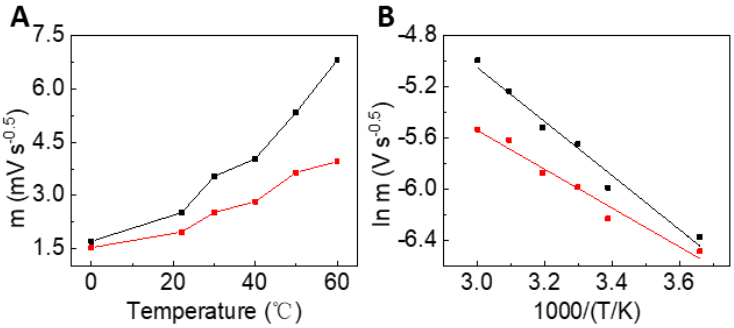

Figure 4.19. Comparison of self-discharge mechanisms in supercapacitors using PP (black) and sPS+PP (red) separators. The fit values of m versus temperature, shown in (a) a linear scale and (b) a natural logarithmic scale for determining thermal activation energies.

From Figure 4.18, for both PP and sPS+PP separators, the device characteristics follow a linear relationship when plotted as V versus $\sqrt{t}$, indicating that diffusion-limited reactions were the determining factor in self-discharge processes. In fact, in simplifying Equation 1 and eliminating

the activation term, the values of *m* obtained from fitting data to $V(t) = V_0 - m\sqrt{t}$ are essentially the same as fitting to the full Equation 1 (Table 4.1 and Table 4.2); results from either fit approach differ by less than 1%.

Table 4.1. The fit values for the device with a PP separator under different temperature, taken after cycle 5. The error in fitting is less than 5%.

Fitting equation	$V=V_0-a*\ln(t+b)-m*t^{0.5}$			$V=V_0-m*t^{0.5}$
T (°C)	a (V s^{-1})	b (s)	m (V $s^{-0.5}$)	m (V $s^{-0.5}$)
0	1.1E-4	3.3E-8	0.00171	0.00172
22	1.4E-4	3.6E-8	0.00251	0.00252
30	3E-14	3.2	0.00353	0.00354
40	9.1E-6	3.7E-12	0.00403	0.00404
50	1.11E-4	3.2E-08	0.00534	0.00525
60	8.9E-12	2.2E-14	0.00681	0.00681

Table 4.2. The fit values for the device with a sPS+PP separator under different temperature, taken after cycle 5. The error in fitting is less than 5%.

Fitting equation	$V=V_0-a*\ln(t+b)-m*t^{0.5}$			$V=V_0-m*t^{0.5}$
T (°C)	a (V s^{-1})	b (s)	m (V $s^{-0.5}$)	m (V $s^{-0.5}$)
0	1.9E-9	3.6E-7	0.00153	0.00153
22	7.7E-9	6E-8	0.00197	0.00197
30	0.00018	3.6E-8	0.00252	0.00253
40	0.00024	3E-8	0.00283	0.00283
50	0.000178	3.5E-8	0.00365	0.00365
60	0.015	0.64	0.00396	0.00440

In Figure. 4.19a, the fit values of *m* show temperature dependence, reflecting the trend that the potential decay was larger as temperature was increased from 0°C to 60°C. In the diffusion-control model, the variable *m* is expressed in physical parameters[151,153,169] as $m = 2zFAc_r\sqrt{D}/(C\sqrt{\pi})$, where *z* is the stoichiometric number of electrons in the reaction, *F* is Faraday's constant, *A* is electrode area, c_r is the initial concentration of reacting species, *D* is the diffusion coefficient, and *C* is the device capacitance. The parameters *z, F, A, C* are the same between the supercapacitors,

and thus any difference in m is due to concentration c_r or diffusion rate D of impurities. Across the temperature range, the m value was smaller in the supercapacitor with sPS than the one without it, showing that the sPS layer minimized impurity concentration and/or diffusion better than conventional PP separators.

In Figure 4.19b, the temperature dependence of m was further analyzed by using the Arrhenius equation: $\ln(m) = \ln(m_0) - E_a/RT$, where E_a is the thermal activation energy, T is the temperature, R is the ideal gas constant, and m_0 is the pre-exponential factor. The extracted values are E_a = 17.5 kJ mol^{-1}, m_0 = 3.58 mV s$^{-0.5}$ for the device with PP and E_a = 12.6 kJ mol^{-1}, m_0 = 0.34 mV s$^{-0.5}$ for the other with PS+PP. The m_0 factor is temperature independent and proportional to the impurity concentration, with the lower value indicating the sPS+PP based system showed a low impurity concentration. Meanwhile, because diffusion is thermally activated, it is influenced by E_a. A low E_a value implied that the change in diffusion rate with temperature is small. As such, the potential decay in the supercapacitors using sPS+PP separator is less severe with rising temperature, compared to the device with only PP.

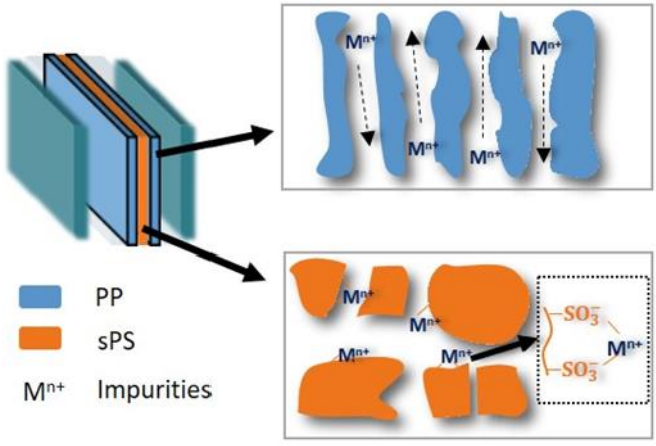

Figure 4.20. Schematic illustrating the capture of cationic impurities by sulfonate functional groups.

Thus, the above analyses suggest that the sulfonate groups in sPS can suppress self-discharge through two mechanisms, by decreasing the concentration of redox impurities through ion-exchange adsorption and by slowing down the diffusion of impurities. The impurities that cause self-discharge reactions are likely transition metal ions, for example Fe^{2+}/Fe^{3+} found in carbon electrodes.[170] Figure 4.20 illustrates the different interactions between transition metal ions M^{n+} and the separator material. Whereas PP films contain porous, columnar conduits for all ions to pass through, sPS is a strong cationic exchange resin and preferentially retain impurity ions M^{n+} over electrolyte cations (K^+ or H^+), as the impurities are in high oxidation states and strongly bound to the sulfonate groups on the separator.

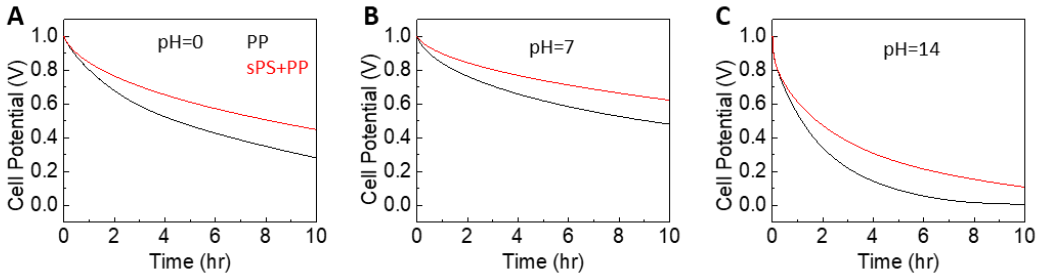

Figure 4.21. Potential change of supercapacitors with different separators and under different pH, using an electrolyte of (a) 0.5 M H_2SO_4 (pH=0), (b) 1 M KCl (pH=7), and (c) 1 M KOH (pH=14).

In addition to the aqueous KCl electrolyte with neutral pH =7, a highly acidic (0.5 M H_2SO_4, pH= 0) or alkaline (1M KOH, pH= 14) electrolyte was used for the supercapacitors to study the effect of pH on potential decay. The decay was the most severe with the alkaline electrolyte, then the acidic one, and least with the neutral electrolyte (Figure 4.21)[171]. The PEDOT electrodes are known to be more stable in acidic than alkaline environment. The rate of self-discharge in acidic electrolyte was slightly worse than in neutral, because of a higher concentration of H^+ that competes with the exchange of impurity ions, resulting in less effective adsorption of the impurities. Nonetheless, regardless of pH, the sPS+PP separator consistently reduced the cell

potential decay better than PP alone, implying that the ion-exchange function is maintained over the entire pH range.

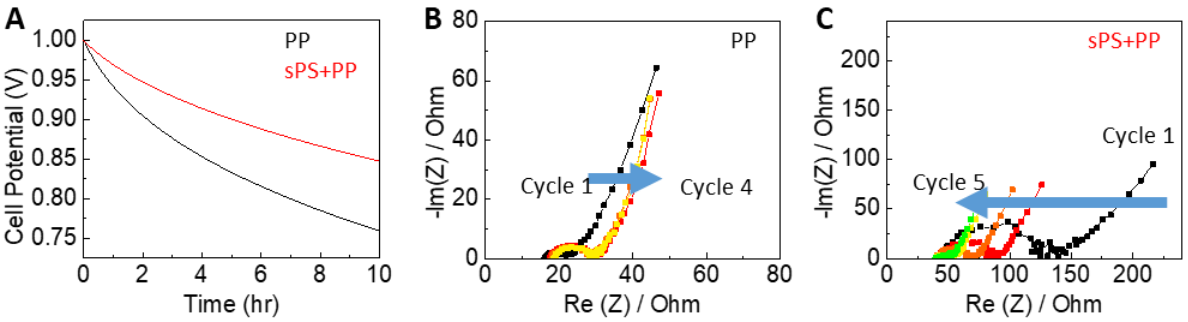

Figure 4.22. (a) Potential change of supercapacitors with different separators using an organic electrolyte of 0.5 M $TEABF_4$/PC. Imaginary vs real impedance as a function of charge-discharge cycles, for the device with a separator of (b) PP or (c) sPS+PP. The impedance settled to the same values after cycle 5.

Besides aqueous electrolytes, organic electrolyte (0.5 M tetraethylammonium tetrafluoroborate $TEABF_4$ in propylene carbonate PC) was also used in the supercapacitors, and again the sPS+PP separator was beneficial to suppress potential decay in these cells, with only 15% loss in potential after an open-circuit period of 10 hours, compared to the 25% loss in the device with only PP (Figure 4.22). Overall, the sPS+PP separator shows its wide applicability to reduce impurity side reactions in various aqueous and organic electrolyte systems.

4.5 Applications in Wireless RF Energy Harvesting

As we have clarified the role of sPS in mitigating self-discharge in our supercapacitors, we proceeded to integrate our devices with a demonstration circuit that would harvest RF energy and store it in the supercapacitor, which then can serve as the power source for numerous electronic applications. Since environmental energy harvesting is intermittent by its nature, the storage supercapacitor in the energy harvesting circuit serves an important role as a continuously available energy reservoir. While the intricacies of power management, such as the duty cycle, peak and quiescent power, *etc.*, in RF energy harvesting circuits are discussed in prior work such as

References [172,173], here we are mainly concerned about the key issue of leakage current[174,175] which must be mitigated, in order to use supercapacitors in energy harvesting circuits.

Leakage current of the storage devices must be less than the input current, otherwise charge will be draining faster than coming in, and device will never reach the desired terminal voltage. While near-field RF density is permitted[173] to be up to 1 mW/cm^2, environmental RF radiation power typically varies between 1—200 μW/cm^2, and so we assume that to charge a supercapacitor to reach 1 V, the charging current will be on the order of μA. Leakage current of supercapacitors are often in μA range, originating from charge redistribution and the same side reactions causing self-discharge and potential decay. We recorded the leakage current of our supercapacitors with different separators by monitoring the current flow needed to maintain the cell at a constant voltage (the segment between t_{hold} and t_{oc} in Figure. 4.16). The leakage current is ~3 μA in the device with PP and ~ 1μA in the one with sPS+PP, for the condition of 1 V bias in Figure. 4.23a.

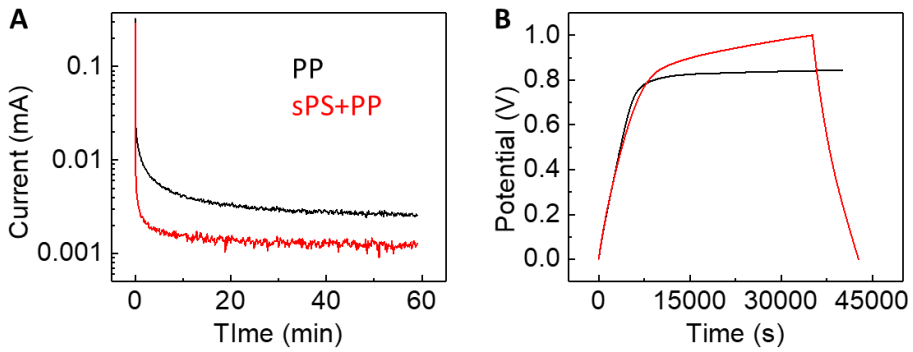

Figure 4.23. (a) Leakage current in supercapacitors with different separators in 1M KCl electrolyte. (b) Galvanostatic charge-discharge characteristics at a constant current input of 1 μA (current density = 0.5 mA/g). The device with PP was not discharged because it did not reach the terminal voltage of 1 V.

We note that leakage is dependent on the cell potential;[155] that is, if the potential is decreased, the driving force for spontaneous discharge reactions also decreases, resulting in a smaller leakage current. This voltage dependence leads to the characteristics in Figure. 4.23b, where initially the devices were able to accumulate the input charge and showed increasing cell voltage when the

leakage is small at low potential. However, as the potential reached above 0.7 V, the corresponding leakage current increased, making it more difficult to accrue incoming charge and hence the rise in voltage slowed down. The supercapacitor with the PP separator was not able to get to the terminal voltage of 1 V when the input current was at 1 μA. Meanwhile, the device with sPS+PP reached the target of 1 V, indicating that its leakage current was ≤ 1 μA for the whole potential range.

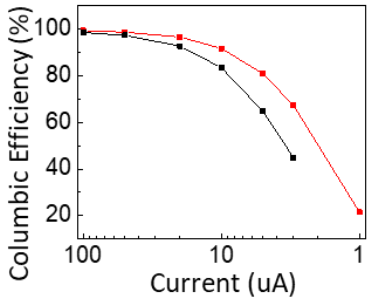

Figure 4.24. Coulombic efficiency for supercapacitors at various current levels.

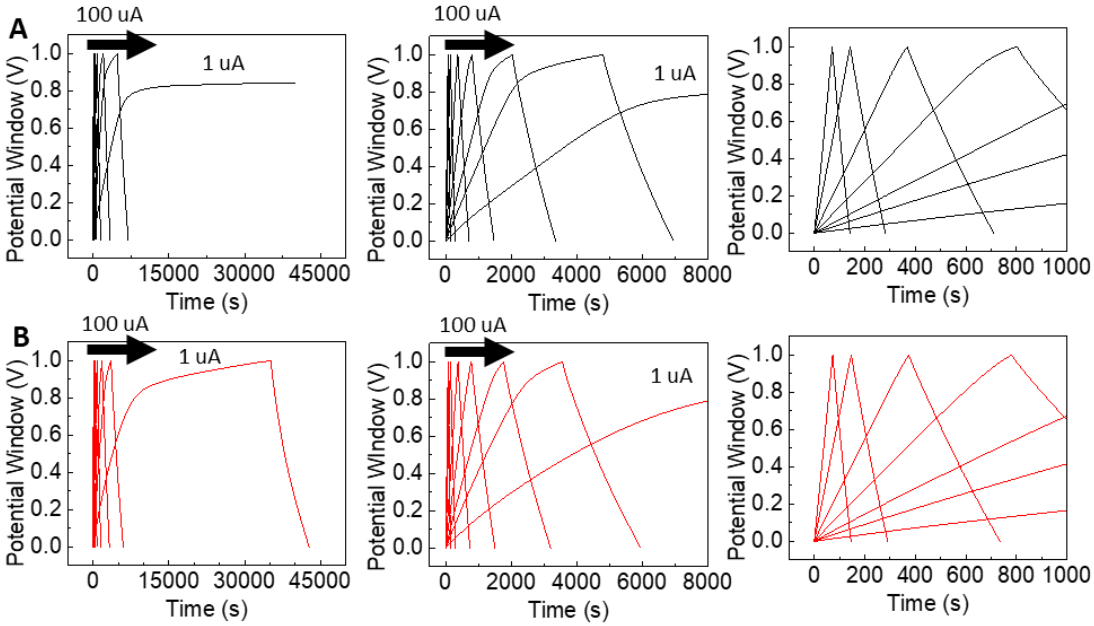

Figure 4.25. Galvanostatic charging versus time, for the device with (a) a PP or (b) a sPS+PP separator. The charging current is 100 uA, 50 uA, 20 uA, 10 uA, 5 uA, 3 uA, and 1 uA. The right side is the extended figure of 100 uA to 3 uA.

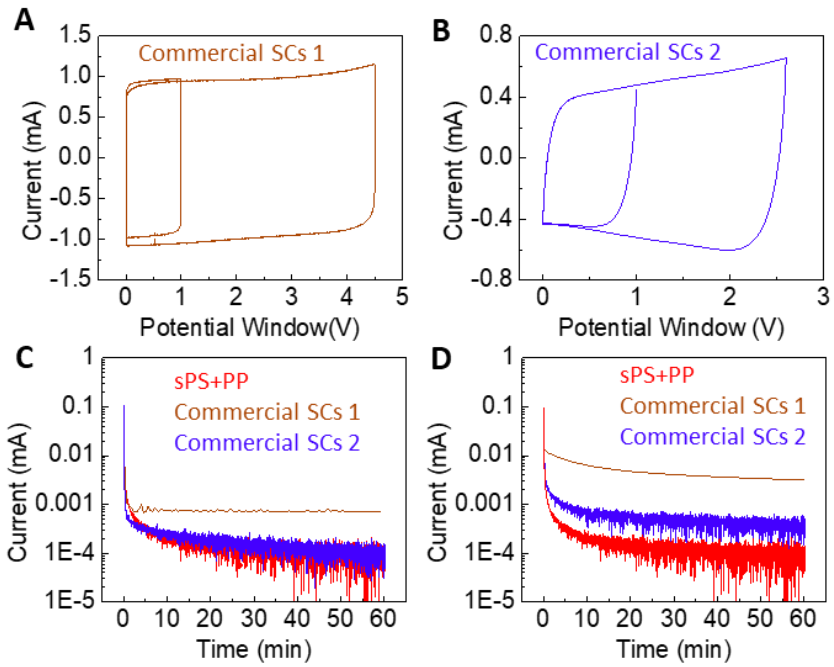

Figure 4.26. Cyclic voltammetry at 50 mV/s of (a) commercial SCs 1 (AVX Corporation, BZ054B223ZSB) and (b) commercial SCs 2 (Seiko Instruments, CPM3225A-2K). (c) Leakage current comparison of our supercapacitor with sPs-PP separator in organic electrolyte ($TEABF_4$ in PC), commercial SCs 1, and commercial SCs 2 at 1 V. (d) Leakage current of sPs-PP based SCs with organic electrolyte at 1 V, commercial SCs 1 at 4.5V and commercial SCs at 2.6 V.

Figure 4.24 shows the coulombic efficiencies of our devices as a function of the input current level, to compare the ratio of the output charge to the input charge in a charge–discharge cycle. Coulombic efficiencies are calculated from GCD curves (Figure 4.25) and typically used to evaluate the extent of side reactions, and we can also interpret it in the context of leakage problems. For charging current above 20 μA (equivalent to a current density of 10 mA/g), the efficiency is near 100% for the device with sPS+PP separator, meaning that there is no loss in storage and all the input energy are completely returned during output delivery. With lower charging current, the difference between charging time and discharging time become larger (Figure 4.23b), and the coulombic efficiency is gradually reduced, down to 22% when the current was at 1 μA. The supercapacitors can become inefficient at charge storage and delivery in low-power systems. Nonetheless, on an encouraging note, Figure 4.25 points out that the devices are well suited for

charging current above 20 μA, which is easily met by the input from energy-harvesting photovoltaic cells. Moreover, the sPS+PP separator enables reduction of the device leakage current, superior to that of standard commercial supercapacitors (comparisons in Figure 4.26); it helps the retention of energy density when the cell is at open-circuit state, as well as increases the efficiency of the charging/discharging process.

To test if our supercapacitor with the sPS+PP separator can work in RF energy-harvesting applications, we connected the pouch cell to the commercially available circuit board Powercast P2110, which converted 915 MHz RF signals to supply direct current to the storage device (Figure 4.27a). This board converted RF energy into DC power, and we disconnected the on-board storage capacitor and replaced it with our own pouch cell. The RF transmitting and receiving was done with a 915 MHz PCB dipole antenna and a 915 MHz PCB patch antenna, respectively. This wireless energy harvester worked in near field, with working distance up to 6 cm. The transmitting signal was generated by a RF signal generator (Fluke 6062A). The voltage of the supercapacitor was monitored on an oscilloscope (Tektronix TDS 40A) as the circuit charged and discharged.

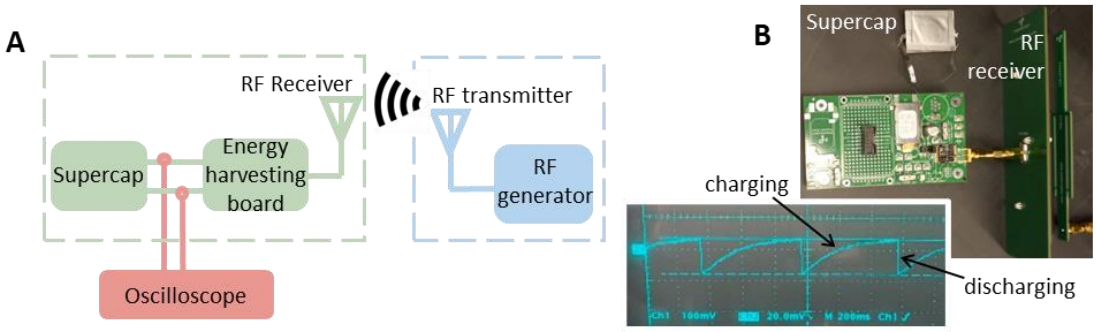

Figure 4.27. (a) Schematic and b) photograph of the RF energy harvesting circuit connected to a supercapacitor pouch cell. The photograph of the oscilloscope screen shows voltage changes with charging and discharging of the supercapacitor. For this near-field transmission setup, the charging power was 178 μW.

The voltage rails for this demonstration were set at 1.02 V and 1.25 V. That is, when the supercapacitor was at 1.02 V, the harvester circuit initiated the charging process to bring up the

supercapacitor voltage to 1.25 V. Upon reaching 1.02 V, the harvester circuit was programmed to discharge the supercapacitor, which supplied current to light up a light-emitting diode. Then when the voltage dropped back to 1.02 V, charging re-started, and the cycles of charging and discharging are repeated. Such voltage cycles are shown in the photograph of Figure. 4.27b, and the charging time was 6 second at an input power of 178 μW. This demonstration has achieved wireless charging of our low-leakage supercapacitor and revealed the potential of our device in RF energy harvesting applications.

4.6 Conclusion

In conclusion, this work has successfully incorporated a sulfonate ion-exchange resin in separators to trap impurities and thereby suppress self-discharge reactions in supercapacitors with PEDOT as redox electrodes. The cation exchange mechanism in the sPS-modified separator was universally effective with organic and aqueous electrolytes and in pH range from 0 to 14. After 10 hours in open circuit, the device with a sPS+PP separator was shown to retain 70% of its terminal voltage in the aqueous electrolyte (KCl in DI water) and 85% in the organic one ($TEABF_4$ in PC) at room temperature. The supercapacitors with sPS+PP separators maintained its potential better than the ones with conventional sPTFE or PP films, without sacrificing the rate performance or specific capacitance.

The temperature-dependent characteristics of potential decay were found to match the diffusion-limited self-discharge model, indicating that reduction of redox impurity concentration and diffusion was key to improve potential retention. For the device with a sPS+PP separator, the leakage current was sufficiently low, and the supercapacitor was demonstrated to work with RF energy harvesting circuits. The coulombic efficiency of our pouch cell was improved by the sPS+PP separator, to serve as an energy reservoir in systems with low charging current. Lastly,

beyond supercapacitors, this work may be applicable to separator designs in other storage devices such as batteries and fuel cells, to mitigate deleterious effects from diffusion of transition metal contaminants between electrodes.

Chapter 4, in part, is a reprint of the material as it appears in ACS Energy Letters. Kaiping Wang, Lulu Yao, Mehran Jahon, Jiaxi Liu, Matthew Gonzalez, Ping Liu, Vincent Leung, Xinyu Zhang, Tse Nga Ng. Ion-exchange separators suppressing self-discharge in polymeric supercapacitors. The dissertation author was the primary investigator and co-first author of the paper.

CHAPTER 5: SUMMARY AND FUTURE WORK

In summary, supercapacitors with high energy density and low leakage current were developed for the self-powered electronics. From electrode materials side, the composite electrode with open-shell conjugated polymer and reduced graphene oxide achieves electrodes with capacitance up to 186 mF cm^{-2} (372 F cm^{-3}) and ultrafast kinetics. From configurations ide, novel gradient electrolyte design ensures the structural supercapacitor both high electrochemical performance and mechanical properties, providing a new strategy to add additional energy to the energy storage system. Furthermore, thorough self-discharge analysis has been conducted to effectively reduce the leakage current in supercapacitors, thereby preserving stored energy and boosting charging efficiency with a smaller charging current. The practical applications of these advanced energy storage devices are demonstrated in solar panel-powered structural boats and RF energy-powered LEDs, highlighting their potential in a range of self-powered electronic applications.

Of course, more works are needed to further enhance the performance of the energy storage unit for the self-powered electronics. Metal ion capacitors, which combine a battery-type cathode with a supercapacitor-type anode, capitalize on the strengths of both components. However, their application is constrained by specific configurations and the selection of electrode materials. For example, Zn ion capacitors can achieve higher energy densities compared to typical supercapacitor materials. Yet issues such as Zn dendrite formation and corrosive interactions with the electrolyte limit their efficiency, making thick Zn foils the most common choice for anodes and consequently restricting the device's overall energy density. Innovations in designing dendrite-free anodes and anode-free devices are essential to attain higher energy densities.

In the realm of structural supercapacitors, most research has been focused on the development of organic-based electrolytes. However, the widely used electrochemical supercapacitors electrode

materials like MnO_2, PANI, PEDOT, *etc*. reach their peak specific capacitance in aqueous electrolytes. Therefore, developing aqueous-based structural electrolytes is crucial to unlock the full potential of structural supercapacitors. Advancements in these areas will significantly enhance the energy density of storage units in self-powered electronics, thereby extending the operational duration of sensors and signal processors.

REFERENCES

(1) Farhan, L.; Shukur, S. T.; Alissa, A. E.; Alrweg, M.; Raza, U.; Kharel, R. A Survey on the Challenges and Opportunities of the Internet of Things (IoT). In *2017 Eleventh International Conference on Sensing Technology (ICST)*; 2017; pp 1–5. https://doi.org/10.1109/ICSensT.2017.8304465.

(2) Niyato, D.; Kim, D. I.; Maso, M.; Han, Z. Wireless Powered Communication Networks: Research Directions and Technological Approaches. *IEEE Wirel. Commun.* **2017**, *24* (6), 88–97. https://doi.org/10.1109/MWC.2017.1600116.

(3) Raj, A.; Steingart, D. Review—Power Sources for the Internet of Things. *J. Electrochem. Soc.* **2018**, *165* (8), B3130–B3136. https://doi.org/10.1149/2.0181808jes.

(4) Liu, L.; Guo, X.; Lee, C. Promoting Smart Cities into the 5G Era with Multi-Field Internet of Things (IoT) Applications Powered with Advanced Mechanical Energy Harvesters. *Nano Energy* **2021**, *88*, 106304. https://doi.org/https://doi.org/10.1016/j.nanoen.2021.106304.

(5) Fan, F. R.; Tang, W.; Wang, Z. L. Flexible Nanogenerators for Energy Harvesting and Self-Powered Electronics. *Adv. Mater.* **2016**, *28* (22), 4283–4305. https://doi.org/https://doi.org/10.1002/adma.201504299.

(6) Ahmed, A.; Hassan, I.; El-Kady, M. F.; Radhi, A.; Jeong, C. K.; Selvaganapathy, P. R.; Zu, J.; Ren, S.; Wang, Q.; Kaner, R. B. Integrated Triboelectric Nanogenerators in the Era of the Internet of Things. *Adv. Sci.* **2019**, *6* (24), 1802230. https://doi.org/https://doi.org/10.1002/advs.201802230.

(7) Luo, M.; Feng, Y.; Wang, T.; Guan, J. Micro-/Nanorobots at Work in Active Drug Delivery. *Adv. Funct. Mater.* **2018**, *28* (25), 1706100. https://doi.org/https://doi.org/10.1002/adfm.201706100.

(8) Zeng, X.; Peng, R.; Fan, Z.; Lin, Y. Self-Powered and Wearable Biosensors for Healthcare. *Mater. Today Energy* **2022**, *23*, 100900. https://doi.org/https://doi.org/10.1016/j.mtener.2021.100900.

(9) Zhang, C.; Chen, J.; Xuan, W.; Huang, S.; You, B.; Li, W.; Sun, L.; Jin, H.; Wang, X.; Dong, S.; Luo, J.; Flewitt, A. J.; Wang, Z. L. Conjunction of Triboelectric Nanogenerator with Induction Coils as Wireless Power Sources and Self-Powered Wireless Sensors. *Nat. Commun.* **2020**, *11* (1), 58. https://doi.org/10.1038/s41467-019-13653-w.

(10) Shen, C.; Xu, S.; Xie, Y.; Sanghadasa, M.; Wang, X.; Lin, L. A Review of On-Chip Micro Supercapacitors for Integrated Self-Powering Systems. *J. Microelectromechanical Syst.* **2017**, *26* (5), 949–965. https://doi.org/10.1109/JMEMS.2017.2723018.

(11) Lethien, C.; Le Bideau, J.; Brousse, T. Challenges and Prospects of 3D Micro-Supercapacitors for Powering the Internet of Things. *Energy Environ. Sci.* **2019**, *12* (1), 96–115. https://doi.org/10.1039/C8EE02029A.

(12) Guo, R.; Chen, J.; Yang, B.; Liu, L.; Su, L.; Shen, B.; Yan, X. In-Plane Micro-Supercapacitors for an Integrated Device on One Piece of Paper. *Adv. Funct. Mater.* **2017**, *27* (43), 1702394. https://doi.org/https://doi.org/10.1002/adfm.201702394.

(13) Ye, J.; Tan, H.; Wu, S.; Ni, K.; Pan, F.; Liu, J.; Tao, Z.; Qu, Y.; Ji, H.; Simon, P.; Zhu, Y. Direct Laser Writing of Graphene Made from Chemical Vapor Deposition for Flexible, Integratable Micro-Supercapacitors with Ultrahigh Power Output. *Adv. Mater.* **2018**, *30* (27), 1801384. https://doi.org/https://doi.org/10.1002/adma.201801384.

(14) Hu, Y.; Zhang, Y.; Xu, C.; Lin, L.; Snyder, R. L.; Wang, Z. L. Self-Powered System with Wireless Data Transmission. *Nano Lett.* **2011**, *11* (6), 2572–2577. https://doi.org/10.1021/nl201505c.

(15) Liu, J.; Wang, J.; Xu, C.; Jiang, H.; Li, C.; Zhang, L.; Lin, J.; Shen, Z. X. Advanced Energy Storage Devices: Basic Principles, Analytical Methods, and Rational Materials Design. *Adv. Sci.* **2018**, *5* (1), 1700322. https://doi.org/https://doi.org/10.1002/advs.201700322.

(16) Olabi, A. G.; Onumaegbu, C.; Wilberforce, T.; Ramadan, M.; Abdelkareem, M. A.; Al – Alami, A. H. Critical Review of Energy Storage Systems. *Energy* **2021**, *214*, 118987. https://doi.org/https://doi.org/10.1016/j.energy.2020.118987.

(17) Xie, J.; Yang, P.; Wang, Y.; Qi, T.; Lei, Y.; Li, C. M. Puzzles and Confusions in Supercapacitor and Battery: Theory and Solutions. *J. Power Sources* **2018**, *401*, 213–223.

(18) Winter, M.; Brodd, R. J. What Are Batteries, Fuel Cells, and Supercapacitors? *Chem. Rev.* **2004**, *104* (10), 4245–4270. https://doi.org/10.1021/cr020730k.

(19) Shao, Y.; El-Kady, M. F.; Sun, J.; Li, Y.; Zhang, Q.; Zhu, M.; Wang, H.; Dunn, B.; Kaner, R. B. Design and Mechanisms of Asymmetric Supercapacitors. *Chem. Rev.* **2018**, *118* (18), 9233–9280. https://doi.org/10.1021/acs.chemrev.8b00252.

(20) Wu, Y.; Cao, C. The Way to Improve the Energy Density of Supercapacitors: Progress and Perspective. *Sci. China Mater* **2018**, *61* (12), 1517–1526.

(21) Noori, A.; El-Kady, M. F.; Rahmanifar, M. S.; Kaner, R. B.; Mousavi, M. F. Towards Establishing Standard Performance Metrics for Batteries, Supercapacitors and Beyond. *Chem. Soc. Rev.* **2019**, *48* (5), 1272–1341. https://doi.org/10.1039/C8CS00581H.

(22) Wu, J. Understanding the Electric Double-Layer Structure, Capacitance, and Charging Dynamics. *Chem. Rev.* **2022**, *122* (12), 10821–10859. https://doi.org/10.1021/acs.chemrev.2c00097.

(23) Yang, I.; Kwon, D.; Kim, M.-S.; Jung, J. C. A Comparative Study of Activated Carbon Aerogel and Commercial Activated Carbons as Electrode Materials for Organic Electric

Double-Layer Capacitors. *Carbon N. Y.* **2018**, *132*, 503–511. https://doi.org/https://doi.org/10.1016/j.carbon.2018.02.076.

(24) Manisha, V.; Tonya, P.; Li, J. Supercapacitors: Review of Materials and Fabrication Methods. *J. Energy Eng.* **2013**, *139* (2), 72–79. https://doi.org/10.1061/(ASCE)EY.1943-7897.0000102.

(25) Vangari, M.; Pryor, T.; Jiang, L. Supercapacitors: Review of Materials and Fabrication Methods. *J. energy Eng.* **2013**, *139* (2), 72–79.

(26) Fleischmann, S.; Mitchell, J. B.; Wang, R.; Zhan, C.; Jiang, D.; Presser, V.; Augustyn, V. Pseudocapacitance: From Fundamental Understanding to High Power Energy Storage Materials. *Chem. Rev.* **2020**, *120* (14), 6738–6782. https://doi.org/10.1021/acs.chemrev.0c00170.

(27) Choi, C.; Ashby, D. S.; Butts, D. M.; DeBlock, R. H.; Wei, Q.; Lau, J.; Dunn, B. Achieving High Energy Density and High Power Density with Pseudocapacitive Materials. *Nat. Rev. Mater.* **2020**, *5* (1), 5–19. https://doi.org/10.1038/s41578-019-0142-z.

(28) Jiang, Y.; Liu, J. Definitions of Pseudocapacitive Materials: A Brief Review. *ENERGY Environ. Mater.* **2019**, *2* (1), 30–37. https://doi.org/https://doi.org/10.1002/eem2.12028.

(29) Bryan, A. M.; Santino, L. M.; Lu, Y.; Acharya, S.; D'Arcy, J. M. Conducting Polymers for Pseudocapacitive Energy Storage. *Chem. Mater.* **2016**, *28* (17), 5989–5998. https://doi.org/10.1021/acs.chemmater.6b01762.

(30) Zhang, M.-Y.; Song, Y.; Yang, D.; Qin, Z.; Guo, D.; Bian, L.-J.; Sang, X.-G.; Sun, X.; Liu, X.-X. Redox Poly-Counterion Doped Conducting Polymers for Pseudocapacitive Energy Storage. *Adv. Funct. Mater.* **2021**, *31* (1), 2006203. https://doi.org/https://doi.org/10.1002/adfm.202006203.

(31) Hashemi, D.; Ma, X.; Ansari, R.; Kim, J.; Kieffer, J. Design Principles for the Energy Level Tuning in Donor/Acceptor Conjugated Polymers. *Phys. Chem. Chem. Phys.* **2019**, *21* (2), 789–799. https://doi.org/10.1039/C8CP03341B.

(32) Wu, J.-S.; Cheng, S.-W.; Cheng, Y.-J.; Hsu, C.-S. Donor–Acceptor Conjugated Polymers Based on Multifused Ladder-Type Arenes for Organic Solar Cells. *Chem. Soc. Rev.* **2015**, *44* (5), 1113–1154. https://doi.org/10.1039/C4CS00250D.

(33) Wang, K.; Huang, L.; Eedugurala, N.; Zhang, S.; Sabuj, M. A.; Rai, N.; Gu, X.; Azoulay, J. D.; Ng, T. N. Wide Potential Window Supercapacitors Using Open-Shell Donor–Acceptor Conjugated Polymers with Stable N-Doped States. *Adv. Energy Mater.* **2019**, 1902806. https://doi.org/10.1002/aenm.201902806.

(34) Pati, P. B. Benzazole (B, N, O, S, Se and Te) Based D-A-D Type Oligomers: Switch from Electropolymerization to Structural Aspect. *Org. Electron.* **2016**, *38*, 97–106. https://doi.org/https://doi.org/10.1016/j.orgel.2016.07.035.

(35) Yaseen, M.; Khattak, M. A.; Humayun, M.; Usman, M.; Shah, S. S.; Bibi, S.; Hasnain, B. S.; Ahmad, S. M.; Khan, A.; Shah, N.; Tahir, A. A.; Ullah, H. A Review of Supercapacitors: Materials Design, Modification, and Applications. *Energies*. 2021. https://doi.org/10.3390/en14227779.

(36) Rangom, Y.; Tang, X. (Shirley); Nazar, L. F. Carbon Nanotube-Based Supercapacitors with Excellent Ac Line Filtering and Rate Capability via Improved Interfacial Impedance. *ACS Nano* **2015**, *9* (7), 7248–7255. https://doi.org/10.1021/acsnano.5b02075.

(37) Liu, C.; Yan, X.; Hu, F.; Gao, G.; Wu, G.; Yang, X. Toward Superior Capacitive Energy Storage: Recent Advances in Pore Engineering for Dense Electrodes. *Adv. Mater.* **2018**, *30* (17), 1705713. https://doi.org/https://doi.org/10.1002/adma.201705713.

(38) Fong, K. D.; Wang, T.; Smoukov, S. K. Multidimensional Performance Optimization of Conducting Polymer-Based Supercapacitor Electrodes. *Sustain. Energy Fuels* **2017**, *1* (9), 1857–1874. https://doi.org/10.1039/C7SE00339K.

(39) Simon, P.; Gogotsi, Y. Materials for Electrochemical Capacitors. *Nat. Mater.* **2008**, *7*, 845.

(40) Yu, M.; Lu, Y.; Zheng, H.; Lu, X. New Insights into the Operating Voltage of Aqueous Supercapacitors. *Chem. Eur. J.* **2018**, *24* (15), 3639–3649.

(41) Tian, X.; Zhu, Q.; Xu, B. "Water-in-Salt" Electrolytes for Supercapacitors: A Review. *ChemSusChem* **2021**, *14* (12), 2501–2515. https://doi.org/https://doi.org/10.1002/cssc.202100230.

(42) Suo, L.; Borodin, O.; Gao, T.; Olguin, M.; Ho, J.; Fan, X.; Luo, C.; Wang, C.; Xu, K. "Water-in-Salt" Electrolyte Enables High-Voltage Aqueous Lithium-Ion Chemistries. *Science (80-.).* **2015**, *350* (6263), 938–943. https://doi.org/10.1126/science.aab1595.

(43) Zhong, C.; Deng, Y.; Hu, W.; Qiao, J.; Zhang, L.; Zhang, J. A Review of Electrolyte Materials and Compositions for Electrochemical Supercapacitors. *Chem. Soc. Rev.* **2015**, *44* (21), 7484–7539. https://doi.org/10.1039/C5CS00303B.

(44) Simon, P.; Gogotsi, Y. Perspectives for Electrochemical Capacitors and Related Devices. *Nat. Mater.* **2020**, *19* (11), 1151–1163. https://doi.org/10.1038/s41563-020-0747-z.

(45) Lee, J. A.; Shin, M. K.; Kim, S. H.; Kim, S. J.; Spinks, G. M.; Wallace, G. G.; Ovalle-Robles, R.; Lima, M. D.; Kozlov, M. E.; Baughman, R. H. Hybrid Nanomembranes for High Power and High Energy Density Supercapacitors and Their Yarn Application. *ACS Nano* **2012**, *6* (1), 327–334. https://doi.org/10.1021/nn203640a.

(46) Li, X.; Li, H.; Fan, X.; Shi, X.; Liang, J. 3D-Printed Stretchable Micro-Supercapacitor with Remarkable Areal Performance. *Adv. Energy Mater.* **2020**, *10* (14), 1903794.

https://doi.org/https://doi.org/10.1002/aenm.201903794.

(47) Wu, Z.-S.; Parvez, K.; Li, S.; Yang, S.; Liu, Z.; Liu, S.; Feng, X.; Müllen, K. Alternating Stacked Graphene-Conducting Polymer Compact Films with Ultrahigh Areal and Volumetric Capacitances for High-Energy Micro-Supercapacitors. *Adv. Mater.* **2015**, *27* (27), 4054–4061. https://doi.org/https://doi.org/10.1002/adma.201501643.

(48) Ferris, A.; Garbarino, S.; Guay, D.; Pech, D. 3D RuO2 Microsupercapacitors with Remarkable Areal Energy. *Adv. Mater.* **2015**, *27* (42), 6625–6629. https://doi.org/https://doi.org/10.1002/adma.201503054.

(49) Yue, Y.; Liu, N.; Ma, Y.; Wang, S.; Liu, W.; Luo, C.; Zhang, H.; Cheng, F.; Rao, J.; Hu, X.; Su, J.; Gao, Y. Highly Self-Healable 3D Microsupercapacitor with MXene–Graphene Composite Aerogel. *ACS Nano* **2018**, *12* (5), 4224–4232. https://doi.org/10.1021/acsnano.7b07528.

(50) Zhou, Y.; Qi, H.; Yang, J.; Bo, Z.; Huang, F.; Islam, M. S.; Lu, X.; Dai, L.; Amal, R.; Wang, C. H.; Han, Z. Two-Birds-One-Stone: Multifunctional Supercapacitors beyond Traditional Energy Storage. *Energy Environ. Sci.* **2021**, *14* (4), 1854–1896. https://doi.org/10.1039/D0EE03167D.

(51) Xu, Y.; Lu, W.; Xu, G.; Chou, T.-W. Structural Supercapacitor Composites: A Review. *Compos. Sci. Technol.* **2021**, *204*, 108636. https://doi.org/https://doi.org/10.1016/j.compscitech.2020.108636.

(52) González, C.; Vilatela, J. J.; Molina-Aldareguía, J. M.; Lopes, C. S.; LLorca, J. Structural Composites for Multifunctional Applications: Current Challenges and Future Trends. *Prog. Mater. Sci.* **2017**, *89*, 194–251. https://doi.org/https://doi.org/10.1016/j.pmatsci.2017.04.005.

(53) Yang, P.; Sun, P.; Mai, W. Electrochromic Energy Storage Devices. *Mater. Today* **2016**, *19* (7), 394–402. https://doi.org/https://doi.org/10.1016/j.mattod.2015.11.007.

(54) Cai, G.; Wang, J.; Lee, P. S. Next-Generation Multifunctional Electrochromic Devices. *Acc. Chem. Res.* **2016**, *49* (8), 1469–1476. https://doi.org/10.1021/acs.accounts.6b00183.

(55) Fan, Z.; Islam, N.; Bayne, S. B. Towards Kilohertz Electrochemical Capacitors for Filtering and Pulse Energy Harvesting. *Nano Energy* **2017**, *39*, 306–320. https://doi.org/https://doi.org/10.1016/j.nanoen.2017.06.048.

(56) Miller, J. R.; Outlaw, R. A.; Holloway, B. C. Graphene Double-Layer Capacitor with Ac Line-Filtering Performance. *Science (80-.).* **2010**, *329* (5999), 1637–1639. https://doi.org/10.1126/science.1194372.

(57) Adu-Manu, K. S.; Adam, N.; Tapparello, C.; Ayatollahi, H.; Heinzelman, W. Energy-Harvesting Wireless Sensor Networks (EH-WSNs): A Review. *ACM Trans. Sen. Netw.* **2018**, *14* (2). https://doi.org/10.1145/3183338.

(58) El-Kady, M. F.; Ihns, M.; Li, M.; Hwang, J. Y.; Mousavi, M. F.; Chaney, L.; Lech, A. T.; Kaner, R. B. Engineering Three-Dimensional Hybrid Supercapacitors and Microsupercapacitors for High-Performance Integrated Energy Storage. *Proc. Natl. Acad. Sci.* **2015**, *112* (14), 4233–4238. https://doi.org/10.1073/pnas.1420398112.

(59) Nomura, K.; Nishihara, H.; Kobayashi, N.; Asada, T.; Kyotani, T. 4.4 V Supercapacitors Based on Super-Stable Mesoporous Carbon Sheet Made of Edge-Free Graphene Walls. *Energy Environ. Sci.* **2019**, *12*, 1542–1549. https://doi.org/10.1039/c8ee03184c.

(60) Jiang, H.; Lee, P. S.; Li, C. 3D Carbon Based Nanostructures for Advanced Supercapacitors. *Energy Environ. Sci.* **2013**, *6* (1), 41–53. https://doi.org/10.1039/c2ee23284g.

(61) Xia, Y.; Mathis, T. S.; Zhao, M.; Anasori, B.; Dang, A.; Zhou, Z.; Cho, H.; Gogotsi, Y.;

Yang, S. Thickness-Independent Capacitance of Vertically Aligned Liquid-Crystalline MXenes. *Nature* **2018**, *6* (557), 409–412.

(62) Liang, J.; Mondal, A. K.; Wang, D.-W.; Iacopi, F. Graphene-Based Planar Microsupercapacitors: Recent Advances and Future Challenges. *Adv. Mater. Technol.* **2019**, *4* (1), 1800200. https://doi.org/https://doi.org/10.1002/admt.201800200.

(63) Li, Z.; Gadipelli, S.; Li, H.; Howard, C. A.; Brett, D. J. L.; Shearing, P. R.; Guo, Z.; Parkin, I. P.; Li, F. Tuning the Interlayer Spacing of Graphene Laminate Films for Efficient Pore Utilization towards Compact Capacitive Energy Storage. *Nat. Energy* **2020**, *5* (2), 160–168. https://doi.org/10.1038/s41560-020-0560-6.

(64) Kamboj, N.; Purkait, T.; Das, M.; Sarkar, S.; Hazra, K. S.; Dey, R. S. Ultralong Cycle Life and Outstanding Capacitive Performance of a 10.8 v Metal Free Micro-Supercapacitor with Highly Conducting and Robust Laser-Irradiated Graphene for an Integrated Storage Device. *Energy Environ. Sci.* **2019**, *12* (8), 2507–2517. https://doi.org/10.1039/c9ee01458f.

(65) Muench, S.; Wild, A.; Friebe, C.; Häupler, B.; Janoschka, T.; Schubert, U. S. Polymer-Based Organic Batteries. *Chem. Rev.* **2016**, *116* (16), 9438–9484. https://doi.org/10.1021/acs.chemrev.6b00070.

(66) Lu, Y.; Chen, J. Prospects of Organic Electrode Materials for Practical Lithium Batteries. *Nat. Rev. Chem.* **2020**, *4* (3), 127–142. https://doi.org/10.1038/s41570-020-0160-9.

(67) Huang, L.; Eedugurala, N.; Benasco, A.; Zhang, S.; Mayer, K. S.; Adams, D. J.; Fowler, B.; Lockart, M. M.; Saghayezhian, M.; Tahir, H.; King, E. R.; Morgan, S.; Bowman, M. K.; Gu, X.; Azoulay, J. D. Open-Shell Donor–Acceptor Conjugated Polymers with High Electrical Conductivity. *Adv. Funct. Mater.* **2020**, *30* (24), 1909805. https://doi.org/10.1002/adfm.201909805.

(68) Eftekhari, A. The Mechanism of Ultrafast Supercapacitors. *J. Mater. Chem. A* **2018**, *6* (7), 2866–2876. https://doi.org/10.1039/c7ta10013b.

(69) Toor, A.; Wen, A.; Maksimovic, F.; Gaikwad, A. M.; Pister, K. S. J.; Arias, A. C. Stencil-Printed Lithium-Ion Micro Batteries for IoT Applications. *Nano Energy* **2021**, *82* (October 2020), 105666. https://doi.org/10.1016/j.nanoen.2020.105666.

(70) Zhang, H.; Yao, M.; Wei, J.; Zhang, Y.; Zhang, S.; Gao, Y.; Li, J.; Lu, P.; Yang, B.; Ma, Y. Stable p/n-Dopable Conducting Redox Polymers for High-Voltage Pseudocapacitor Electrode Materials: Structure–Performance Relationship and Detailed Investigation into Charge-Trapping Effect. *Adv. Energy Mater.* **2017**, *7* (21), 1701063. https://doi.org/10.1002/aenm.201701063.

(71) Liang, Y.; Chen, Z.; Jing, Y.; Rong, Y.; Facchetti, A.; Yao, Y. Heavily N-Dopable π-Conjugated Redox Polymers with Ultrafast Energy Storage Capability. *J. Am. Chem. Soc.* **2015**, *137* (15), 4956–4959. https://doi.org/10.1021/jacs.5b02290.

(72) Wang, S.; Li, F.; Easley, A. D.; Lutkenhaus, J. L. Real-Time Insight into the Doping Mechanism of Redox-Active Organic Radical Polymers. *Nat. Mater.* **2019**, *18* (1), 69–75. https://doi.org/10.1038/s41563-018-0215-1.

(73) Sung, S. H.; Savoie, B. M.; Boudouris, B. W.; Joo, Y.; Agarkar, V. A Nonconjugated Radical Polymer Glass with High Electrical Conductivity. *Science (80-.).* **2018**, *359* (6382), 1391–1395. https://doi.org/10.1126/science.aao7287.

(74) Zhang, M.; Wang, Y.; Huang, L.; Xu, Z.; Li, C.; Shi, G. Multifunctional Pristine Chemically Modified Graphene Films as Strong as Stainless Steel. *Adv. Mater.* **2015**, *27* (42), 6708–6713. https://doi.org/https://doi.org/10.1002/adma.201503045.

(75) Schon, T. B.; McAllister, B. T.; Li, P. F.; Seferos, D. S. The Rise of Organic Electrode

Materials for Energy Storage. *Chem. Soc. Rev.* **2016**, *45* (22), 6345–6404. https://doi.org/10.1039/c6cs00173d.

(76) Ji, H.; Zhao, X.; Qiao, Z.; Jung, J.; Zhu, Y.; Lu, Y.; Zhang, L. L.; MacDonald, A. H.; Ruoff, R. S. Capacitance of Carbon-Based Electrical Double-Layer Capacitors. *Nat. Commun.* **2014**, *5*, 3317. https://doi.org/10.1038/ncomms4317.

(77) McAllister, B. T.; Schon, T. B.; DiCarmine, P. M.; Seferos, D. S. A Study of Fused-Ring Thieno[3,4-: E] Pyrazine Polymers as n-Type Materials for Organic Supercapacitors. *Polym. Chem.* **2017**, *8* (34), 5194–5202. https://doi.org/10.1039/c7py00512a.

(78) Schon, T. B.; Dicarmine, P. M.; Seferos, D. S. Polyfullerene Electrodes for High Power Supercapacitors. *Adv. Energy Mater.* **2014**, *4* (7), 1–6. https://doi.org/10.1002/aenm.201301509.

(79) Zhang, H.; Tang, X.; Zhao, D.; Zheng, N.; Huang, L.; Sun, T.; Gu, C.; Ma, Y. Suppressing Charge Trapping Effect in Ambipolar Conducting Polymer with Vertically Standing Graphene as the Composite Electrode for High Performance Supercapacitor. *Energy Storage Mater.* **2020**, *29*, 281–286. https://doi.org/https://doi.org/10.1016/j.ensm.2020.04.024.

(80) Gund, G. S.; Park, J. H.; Harpalsinh, R.; Kota, M.; Shin, J. H.; Kim, T. il; Gogotsi, Y.; Park, H. S. MXene/Polymer Hybrid Materials for Flexible AC-Filtering Electrochemical Capacitors. *Joule* **2019**, *3* (1), 164–176. https://doi.org/10.1016/j.joule.2018.10.017.

(81) Wu, M.; Chi, F.; Geng, H.; Ma, H.; Zhang, M.; Gao, T.; Li, C.; Qu, L. Arbitrary Waveform AC Line Filtering Applicable to Hundreds of Volts Based on Aqueous Electrochemical Capacitors. *Nat. Commun.* **2019**, *10* (1), 2855. https://doi.org/10.1038/s41467-019-10886-7.

(82) Zhang, M.; Zhou, Q.; Chen, J.; Yu, X.; Huang, L.; Li, Y.; Li, C.; Shi, G. An Ultrahigh-Rate Electrochemical Capacitor Based on Solution-Processed Highly Conductive PEDOT:PSS Films for AC Line-Filtering. *Energy Environ. Sci.* **2016**, *9* (6), 2005–2010. https://doi.org/10.1039/c6ee00615a.

(83) Yoo, Y.; Kim, M.-S.; Kim, J.-K.; Kim, Y. S.; Kim, W. Fast-Response Supercapacitors with Graphitic Ordered Mesoporous Carbons and Carbon Nanotubes for AC Line Filtering. *J. Mater. Chem. A* **2016**, *4* (14), 5062–5068. https://doi.org/10.1039/C6TA00921B.

(84) Choi, C.; Robert, K.; Whang, G.; Roussel, P.; Lethien, C.; Dunn, B. Photopatternable Hydroxide Ion Electrolyte for Solid-State Micro-Supercapacitors. *Joule* **2021**, *5* (9), 2466–2478. https://doi.org/https://doi.org/10.1016/j.joule.2021.07.003.

(85) Huang, P.; Lethien, C.; Pinaud, S.; Brousse, K.; Laloo, R.; Turq, V.; Respaud, M.; Demortière, A.; Daffos, B.; Taberna, P. L.; Chaudret, B.; Gogotsi, Y.; Simon, P. On-Chip and Freestanding Elastic Carbon Films for Micro-Supercapacitors. *Science (80-.).* **2016**, *351* (6274), 691–695. https://doi.org/10.1126/science.aad3345.

(86) Xie, J.-Q.; Ji, Y.-Q.; Kang, J.-H.; Sheng, J.-L.; Mao, D.-S.; Fu, X.-Z.; Sun, R.; Wong, C.-P. In Situ Growth of Cu(OH)2@FeOOH Nanotube Arrays on Catalytically Deposited Cu Current Collector Patterns for High-Performance Flexible in-Plane Micro-Sized Energy Storage Devices. *Energy Environ. Sci.* **2019**, *12* (1), 194–205. https://doi.org/10.1039/C8EE01979G.

(87) Pech, D.; Brunet, M.; Durou, H.; Huang, P.; Mochalin, V.; Gogotsi, Y.; Taberna, P.-L.; Simon, P. Ultrahigh-Power Micrometre-Sized Supercapacitors Based on Onion-like Carbon. *Nat. Nanotechnol.* **2010**, *5* (9), 651–654. https://doi.org/10.1038/nnano.2010.162.

(88) Hongwei, S.; Jingjing, Z.; Bo, L.; Yuhang, H.; Xuetao, Z.; Jie, L.; Jinyuan, Z.; Qing, S.;

Erqing, X.; Wei, L.; Kairong, W.; Cunjiang, Y. A Thin, Deformable, High-Performance Supercapacitor Implant That Can Be Biodegraded and Bioabsorbed within an Animal Body. *Sci. Adv.* **2021**, *7* (2), eabe3097. https://doi.org/10.1126/sciadv.abe3097.

(89) Brousse, K.; Pinaud, S.; Nguyen, S.; Fazzini, P.-F.; Makarem, R.; Josse, C.; Thimont, Y.; Chaudret, B.; Taberna, P.-L.; Respaud, M.; Simon, P. Facile and Scalable Preparation of Ruthenium Oxide-Based Flexible Micro-Supercapacitors. *Adv. Energy Mater.* **2020**, *10* (6), 1903136. https://doi.org/https://doi.org/10.1002/aenm.201903136.

(90) Liu, Y.; Zhou, H.; Zhou, W.; Meng, S.; Qi, C.; Liu, Z.; Kong, T. Biocompatible, High-Performance, Wet-Adhesive, Stretchable All-Hydrogel Supercapacitor Implant Based on PANI@rGO/Mxenes Electrode and Hydrogel Electrolyte. *Adv. Energy Mater.* **2021**, *11* (30), 2101329. https://doi.org/https://doi.org/10.1002/aenm.202101329.

(91) Zheng, S.; Wang, H.; Das, P.; Zhang, Y.; Cao, Y.; Ma, J.; Liu, S. (Frank); Wu, Z.-S. Multitasking MXene Inks Enable High-Performance Printable Microelectrochemical Energy Storage Devices for All-Flexible Self-Powered Integrated Systems. *Adv. Mater.* **2021**, *33* (10), 2005449. https://doi.org/https://doi.org/10.1002/adma.202005449.

(92) Zhang, W.; Li, R.; Zheng, H.; Bao, J.; Tang, Y.; Zhou, K. Laser-Assisted Printing of Electrodes Using Metal–Organic Frameworks for Micro-Supercapacitors. *Adv. Funct. Mater.* **2021**, *31* (14), 2009057. https://doi.org/https://doi.org/10.1002/adfm.202009057.

(93) Chu, X.; Chen, G.; Xiao, X.; Wang, Z.; Yang, T.; Xu, Z.; Huang, H.; Wang, Y.; Yan, C.; Chen, N.; Zhang, H.; Yang, W.; Chen, J. Air-Stable Conductive Polymer Ink for Printed Wearable Micro-Supercapacitors. *Small* **2021**, *17* (25), 2100956. https://doi.org/https://doi.org/10.1002/smll.202100956.

(94) Ma, J.; Zheng, S.; Cao, Y.; Zhu, Y.; Das, P.; Wang, H.; Liu, Y.; Wang, J.; Chi, L.; Liu, S.

(Frank); Wu, Z.-S. Aqueous MXene/PH1000 Hybrid Inks for Inkjet-Printing Micro-Supercapacitors with Unprecedented Volumetric Capacitance and Modular Self-Powered Microelectronics. *Adv. Energy Mater.* **2021**, *11* (23), 2100746. https://doi.org/https://doi.org/10.1002/aenm.202100746.

(95) Zhang, Y.; Wang, L.; Zhao, L.; Wang, K.; Zheng, Y.; Yuan, Z.; Wang, D.; Fu, X.; Shen, G.; Han, W. Flexible Self-Powered Integrated Sensing System with 3D Periodic Ordered Black Phosphorus@MXene Thin-Films. *Adv. Mater.* **2021**, *33* (22), 2007890. https://doi.org/https://doi.org/10.1002/adma.202007890.

(96) Robert, K.; Stiévenard, D.; Deresmes, D.; Douard, C.; Iadecola, A.; Troadec, D.; Simon, P.; Nuns, N.; Marinova, M.; Huvé, M.; Roussel, P.; Brousse, T.; Lethien, C. Novel Insights into the Charge Storage Mechanism in Pseudocapacitive Vanadium Nitride Thick Films for High-Performance on-Chip Micro-Supercapacitors. *Energy Environ. Sci.* **2020**, *13* (3), 949–957. https://doi.org/10.1039/C9EE03787J.

(97) Gao, C.; Huang, J.; Xiao, Y.; Zhang, G.; Dai, C.; Li, Z.; Zhao, Y.; Jiang, L.; Qu, L. A Seamlessly Integrated Device of Micro-Supercapacitor and Wireless Charging with Ultrahigh Energy Density and Capacitance. *Nat. Commun.* **2021**, *12* (1), 2647. https://doi.org/10.1038/s41467-021-22912-8.

(98) Zhou, H.; Li, H.; Li, L.; Liu, T.; Chen, G.; Zhu, Y.; Zhou, L.; Huang, H. Structural Composite Energy Storage Devices — a Review. *Mater. Today Energy* **2022**, *24*, 100924. https://doi.org/https://doi.org/10.1016/j.mtener.2021.100924.

(99) Asp, L. E.; Johansson, M.; Lindbergh, G.; Xu, J.; Zenkert, D. Structural Battery Composites: A Review. *Funct. Compos. Struct.* **2019**, *1* (4), 042001. https://doi.org/10.1088/2631-6331/ab5571.

(100) Lutkenhaus, J. L.; Flouda, P. Structural Batteries Take a Load Off. *Sci. Robot.* **2020**, *5* (45), eabd7026. https://doi.org/10.1126/scirobotics.abd7026.

(101) Hopkins, B. J.; Long, J. W.; Rolison, D. R.; Parker, J. F. High-Performance Structural Batteries. *Joule* **2020**, *4* (11), 2240–2243. https://doi.org/10.1016/j.joule.2020.07.027.

(102) Wang, H.; Diao, Y.; Lu, Y.; Yang, H.; Zhou, Q.; Chrulski, K.; D'Arcy, J. M. Energy Storing Bricks for Stationary PEDOT Supercapacitors. *Nat. Commun.* **2020**, *11* (1), 3882. https://doi.org/10.1038/s41467-020-17708-1.

(103) Johannisson, W.; Zenkert, D.; Lindbergh, G. Model of a Structural Battery and Its Potential for System Level Mass Savings. *Multifunct. Mater.* **2019**, *2* (3), 35002. https://doi.org/10.1088/2399-7532/ab3bdd.

(104) Jones, C. E.; Norman, P. J.; Burt, G. M.; Hill, C.; Allegri, G.; Yon, J. M.; Hamerton, I.; Trask, R. S. A Route to Sustainable Aviation: A Roadmap for the Realization of Aircraft Components With Electrical and Structural Multifunctionality. *IEEE Trans. Transp. Electrif.* **2021**, *7* (4), 3032–3049. https://doi.org/10.1109/TTE.2021.3078118.

(105) Deka, B. K.; Hazarika, A.; Kim, J.; Park, Y.-B.; Park, H. W. Recent Development and Challenges of Multifunctional Structural Supercapacitors for Automotive Industries. *Int. J. Energy Res.* **2017**, *41* (10), 1397–1411. https://doi.org/https://doi.org/10.1002/er.3707.

(106) Rubino, F.; Nisticò, A.; Tucci, F.; Carlone, P. Marine Application of Fiber Reinforced Composites: A Review. *Journal of Marine Science and Engineering* . 2020. https://doi.org/10.3390/jmse8010026.

(107) Chen, Y.; Amiri, A.; Boyd, J. G.; Naraghi, M. Promising Trade-Offs Between Energy Storage and Load Bearing in Carbon Nanofibers as Structural Energy Storage Devices. *Adv. Funct. Mater.* **2019**, *29* (33), 1901425.

https://doi.org/https://doi.org/10.1002/adfm.201901425.

(108) Qian, H.; Kucernak, A. R.; Greenhalgh, E. S.; Bismarck, A.; Shaffer, M. S. P. Multifunctional Structural Supercapacitor Composites Based on Carbon Aerogel Modified High Performance Carbon Fiber Fabric. *ACS Appl. Mater. Interfaces* **2013**, *5* (13), 6113–6122. https://doi.org/10.1021/am400947j.

(109) Deka, B. K.; Hazarika, A.; Kwon, Ob.; Kim, D.; Park, Y.-B.; Park, H. W. Multifunctional Enhancement of Woven Carbon Fiber/ZnO Nanotube-Based Structural Supercapacitor and Polyester Resin-Domain Solid-Polymer Electrolytes. *Chem. Eng. J.* **2017**, *325*, 672–680. https://doi.org/https://doi.org/10.1016/j.cej.2017.05.093.

(110) Lee, K.; Shang, Y.; Bobrin, V. A.; Kuchel, R.; Kundu, D.; Corrigan, N.; Boyer, C. 3D Printing Nanostructured Solid Polymer Electrolytes with High Modulus and Conductivity. *Adv. Mater.* **2022**, *n/a* (n/a), 2204816. https://doi.org/https://doi.org/10.1002/adma.202204816.

(111) Reece, R.; Lekakou, C.; Smith, P. A. A Structural Supercapacitor Based on Activated Carbon Fabric and a Solid Electrolyte. *Mater. Sci. Technol.* **2019**, *35* (3), 368–375. https://doi.org/10.1080/02670836.2018.1560536.

(112) Asp, L. E.; Bouton, K.; Carlstedt, D.; Duan, S.; Harnden, R.; Johannisson, W.; Johansen, M.; Johansson, M. K. G.; Lindbergh, G.; Liu, F.; Peuvot, K.; Schneider, L. M.; Xu, J.; Zenkert, D. A Structural Battery and Its Multifunctional Performance. *Adv. Energy Sustain. Res.* **2021**, *2* (3), 2000093. https://doi.org/https://doi.org/10.1002/aesr.202000093.

(113) Javaid, A.; Ho, K. K. C.; Bismarck, A.; Steinke, J. H. G.; Shaffer, M. S. P.; Greenhalgh, E. S. Improving the Multifunctional Behaviour of Structural Supercapacitors by Incorporating Chemically Activated Carbon Fibres and Mesoporous Silica Particles as Reinforcement. *J.*

Compos. Mater. **2018**, *52* (22), 3085–3097.

(114) Kwon, S. J.; Kim, T.; Jung, B. M.; Lee, S. B.; Choi, U. H. Multifunctional Epoxy-Based Solid Polymer Electrolytes for Solid-State Supercapacitors. *ACS Appl. Mater. Interfaces* **2018**, *10* (41), 35108–35117. https://doi.org/10.1021/acsami.8b11016.

(115) Fan, L.-Z.; He, H.; Nan, C.-W. Tailoring Inorganic–Polymer Composites for the Mass Production of Solid-State Batteries. *Nat. Rev. Mater.* **2021**, *6* (11), 1003–1019. https://doi.org/10.1038/s41578-021-00320-0.

(116) Zheng, Y.; Yao, Y.; Ou, J.; Li, M.; Luo, D.; Dou, H.; Li, Z.; Amine, K.; Yu, A.; Chen, Z. A Review of Composite Solid-State Electrolytes for Lithium Batteries: Fundamentals, Key Materials and Advanced Structures. *Chem. Soc. Rev.* **2020**, *49* (23), 8790–8839. https://doi.org/10.1039/D0CS00305K.

(117) Yao, L.; Liu, J.; Eedugurala, N.; Mahalingavelar, P.; Adams, D. J.; Wang, K.; Mayer, K. S.; Azoulay, J. D.; Ng, T. N. Ultrafast High-Energy Micro-Supercapacitors Based on Open-Shell Polymer-Graphene Composites. *Cell Reports Phys. Sci.* **2022**, *3* (3), 100792. https://doi.org/https://doi.org/10.1016/j.xcrp.2022.100792.

(118) Root, S. E.; Savagatrup, S.; Printz, A. D.; Rodriquez, D.; Lipomi, D. J. Mechanical Properties of Organic Semiconductors for Stretchable, Highly Flexible, and Mechanically Robust Electronics. *Chem. Rev.* **2017**, *117* (9), 6467–6499. https://doi.org/10.1021/acs.chemrev.7b00003.

(119) Zhao, Q.; Stalin, S.; Zhao, C.-Z.; Archer, L. A. Designing Solid-State Electrolytes for Safe, Energy-Dense Batteries. *Nat. Rev. Mater.* **2020**, *5* (3), 229–252. https://doi.org/10.1038/s41578-019-0165-5.

(120) Chen, H.; Ling, M.; Hencz, L.; Ling, H. Y.; Li, G.; Lin, Z.; Liu, G.; Zhang, S. Exploring

Chemical, Mechanical, and Electrical Functionalities of Binders for Advanced Energy-Storage Devices. *Chem. Rev.* **2018**, *118* (18), 8936–8982. https://doi.org/10.1021/acs.chemrev.8b00241.

(121) Liu, Q.; Zhao, A.; He, X.; Li, Q.; Sun, J.; Lei, Z.; Liu, Z. H. Full-Temperature All-Solid-State Ti3C2Tx/Aramid Fiber Supercapacitor with Optimal Balance of Capacitive Performance and Flexibility. *Adv. Funct. Mater.* **2021**, *31* (22), 2010944. https://doi.org/10.1002/adfm.202010944.

(122) Augustyn, V.; Simon, P.; Dunn, B. Pseudocapacitive Oxide Materials for High-Rate Electrochemical Energy Storage. *Energy Environ. Sci.* **2014**, *7* (5), 1597–1614. https://doi.org/10.1039/C3EE44164D.

(123) Simon, P.; Gogotsi, Y.; Dunn, B. Where Do Batteries End and Supercapacitors Begin? *Science (80-.).* **2014**, *343* (6176), 1210 LP – 1211. https://doi.org/10.1126/science.1249625.

(124) Brousse, T.; Bélanger, D.; Long, J. W. To Be or Not To Be Pseudocapacitive? *J. Electrochem. Soc.* **2015**, *162* (5), A5185. https://doi.org/10.1149/2.0201505jes.

(125) Kwon, S. R.; Harris, J.; Zhou, T.; Loufakis, D.; Boyd, J. G.; Lutkenhaus, J. L. Mechanically Strong Graphene/Aramid Nanofiber Composite Electrodes for Structural Energy and Power. *ACS Nano* **2017**, *11* (7), 6682–6690. https://doi.org/10.1021/acsnano.7b00790.

(126) Yin, Q.; Jia, H.; Liu, G.; Ji, Q. Tailoring the Mechanical Performance of Carbon Nanotubes Buckypaper by Aramid Nanofibers towards Robust and Compact Supercapacitor Electrode. *Adv. Funct. Mater.* **2022**, *32* (19), 2111177. https://doi.org/https://doi.org/10.1002/adfm.202111177.

(127) Tian, W.; VahidMohammadi, A.; Reid, M. S.; Wang, Z.; Ouyang, L.; Erlandsson, J.;

Pettersson, T.; Wågberg, L.; Beidaghi, M.; Hamedi, M. M. Multifunctional Nanocomposites with High Strength and Capacitance Using 2D MXene and 1D Nanocellulose. *Adv. Mater.* **2019**, *31* (41), 1902977. https://doi.org/https://doi.org/10.1002/adma.201902977.

(128) Zhou, T.; Wu, C.; Wang, Y.; Tomsia, A. P.; Li, M.; Saiz, E.; Fang, S.; Baughman, R. H.; Jiang, L.; Cheng, Q. Super-Tough MXene-Functionalized Graphene Sheets. *Nat. Commun.* **2020**, *11* (1), 2077. https://doi.org/10.1038/s41467-020-15991-6.

(129) Deka, B. K.; Hazarika, A.; Kim, J.; Kim, N.; Jeong, H. E.; Park, Y.-B.; Park, H. W. Bimetallic Copper Cobalt Selenide Nanowire-Anchored Woven Carbon Fiber-Based Structural Supercapacitors. *Chem. Eng. J.* **2019**, *355*, 551–559. https://doi.org/https://doi.org/10.1016/j.cej.2018.08.172.

(130) Lu, L. L.; Lu, Y. Y.; Zhu, Z. X.; Shao, J. X.; Yao, H. Bin; Wang, S.; Zhang, T. W.; Ni, Y.; Wang, X. X.; Yu, S. H. Extremely Fast-Charging Lithium Ion Battery Enabled by Dual-Gradient Structure Design. *Sci. Adv.* **2022**, *8* (17), eabm6624. https://doi.org/10.1126/sciadv.abm6624.

(131) Rana, H. H.; Park, J. H.; Gund, G. S.; Park, H. S. Highly Conducting, Extremely Durable, Phosphorylated Cellulose-Based Ionogels for Renewable Flexible Supercapacitors. *Energy Storage Mater.* **2020**, *25*, 70–75. https://doi.org/https://doi.org/10.1016/j.ensm.2019.10.030.

(132) Lee, D.; Song, Y.; Song, Y.; Oh, S. J.; Choi, U. H.; Kim, J. Multi-Foldable and Environmentally Stable All-Solid-State Supercapacitor Based on Hierarchical Nano-Canyon Structured Ionic-Gel Polymer Electrolyte. *Adv. Funct. Mater.* **2022**, *32* (13), 2109907. https://doi.org/https://doi.org/10.1002/adfm.202109907.

(133) Westover, A. S.; Tian, J. W.; Bernath, S.; Oakes, L.; Edwards, R.; Shabab, F. N.; Chatterjee, S.; Anilkumar, A. V; Pint, C. L. A Multifunctional Load-Bearing Solid-State Supercapacitor. *Nano Lett.* **2014**, *14* (6), 3197–3202. https://doi.org/10.1021/nl500531r.

(134) Reece, R.; Lekakou, C.; Smith, P. A.; Grilli, R.; Trapalis, C. Sulphur-Linked Graphitic and Graphene Oxide Platelet-Based Electrodes for Electrochemical Double Layer Capacitors. *J. Alloys Compd.* **2019**, *792*, 582–593. https://doi.org/https://doi.org/10.1016/j.jallcom.2019.04.072.

(135) Reece, R.; Lekakou, C.; Smith, P. A. A High-Performance Structural Supercapacitor. *ACS Appl. Mater. Interfaces* **2020**, *12* (23), 25683–25692. https://doi.org/10.1021/acsami.9b23427.

(136) Meng, C.; Muralidharan, N.; Teblum, E.; Moyer, K. E.; Nessim, G. D.; Pint, C. L. Multifunctional Structural Ultrabattery Composite. *Nano Lett.* **2018**, *18* (12), 7761–7768. https://doi.org/10.1021/acs.nanolett.8b03510.

(137) Ransil, A.; Belcher, A. M. Structural Ceramic Batteries Using an Earth-Abundant Inorganic Waterglass Binder. *Nat. Commun.* **2021**, *12* (1), 6494. https://doi.org/10.1038/s41467-021-26801-y.

(138) Jin, T.; Ma, Y.; Xiong, Z.; Fan, X.; Luo, Y.; Hui, Z.; Chen, X.; Yang, Y. Bioinspired, Tree-Root-Like Interfacial Designs for Structural Batteries with Enhanced Mechanical Properties. *Adv. Energy Mater.* **2021**, *11* (25), 2100997. https://doi.org/https://doi.org/10.1002/aenm.202100997.

(139) Sha, Z.; Huang, F.; Zhou, Y.; Zhang, J.; Wu, S.; Chen, J.; Brown, S. A.; Peng, S.; Han, Z.; Wang, C.-H. Synergies of Vertical Graphene and Manganese Dioxide in Enhancing the Energy Density of Carbon Fibre-Based Structural Supercapacitors. *Compos. Sci. Technol.*

2021, *201*, 108568. https://doi.org/https://doi.org/10.1016/j.compscitech.2020.108568.

(140) Javaid, A.; Khalid, O.; Shakeel, A.; Noreen, S. Multifunctional Structural Supercapacitors Based on Polyaniline Deposited Carbon Fiber Reinforced Epoxy Composites. *J. Energy Storage* **2021**, *33*, 102168. https://doi.org/https://doi.org/10.1016/j.est.2020.102168.

(141) Ganguly, A.; Karakassides, A.; Benson, J.; Hussain, S.; Papakonstantinou, P. Multifunctional Structural Supercapacitor Based on Urea-Activated Graphene Nanoflakes Directly Grown on Carbon Fiber Electrodes. *ACS Appl. Energy Mater.* **2020**, *3* (5), 4245–4254. https://doi.org/10.1021/acsaem.9b02469.

(142) Pernice, M. F.; Qi, G.; Senokos, E.; Anthony, D. B.; Nguyen, S.; Valkova, M.; Greenhalgh, E. S.; Shaffer, M. S. P.; Kucernak, A. R. J. Mechanical, Electrochemical and Multifunctional Performance of a CFRP/Carbon Aerogel Structural Supercapacitor and Its Corresponding Monofunctional Equivalents. *Multifunct. Mater.* **2022**, *5* (2), 25002.

(143) Qi, G.; Nguyen, S.; Anthony, D. B.; Kucernak, A. R. J.; Shaffer, M. S. P.; Greenhalgh, E. S. The Influence of Fabrication Parameters on the Electrochemical Performance of Multifunctional Structural Supercapacitors. *Multifunct. Mater.* **2021**, *4* (3), 34001.

(144) O'Brien, D. J.; Baechle, D. M.; Wetzel, E. D. Design and Performance of Multifunctional Structural Composite Capacitors. *J. Compos. Mater.* **2011**, *45* (26), 2797–2809. https://doi.org/10.1177/0021998311412207.

(145) Patel, A. G.; Johnson, L.; Arroyave, R.; Lutkenhaus, J. L. Design of Multifunctional Supercapacitor Electrodes Using an Informatics Approach. *Mol. Syst. Des. Eng.* **2019**, *4* (3), 654–663. https://doi.org/10.1039/c8me00060c.

(146) Johannisson, W.; Nguyen, S.; Lindbergh, G.; Zenkert, D.; Greenhalgh, E. S.; Shaffer, M. S. P.; Kucernak, A. R. J. A Residual Performance Methodology to Evaluate Multifunctional

Systems. *Multifunct. Mater.* **2020**, *3* (2), 25002. https://doi.org/10.1088/2399-7532/ab8e95.

(147) Kim, B. C.; Hong, J. Y.; Wallace, G. G.; Park, H. S. Recent Progress in Flexible Electrochemical Capacitors: Electrode Materials, Device Configuration, and Functions. *Adv. Energy Mater.* **2015**, *5* (22), 1500959. https://doi.org/10.1002/aenm.201500959.

(148) Wang, F.; Wu, X.; Yuan, X.; Liu, Z.; Zhang, Y.; Fu, L.; Zhu, Y.; Zhou, Q.; Wu, Y.; Huang, W. Latest Advances in Supercapacitors: From New Electrode Materials to Novel Device Designs. *Chem. Soc. Rev.* **2017**, *46* (22), 6816–6854. https://doi.org/10.1039/c7cs00205j.

(149) Salanne, M.; Rotenberg, B.; Naoi, K.; Kaneko, K.; Taberna, P.-L.; Grey, C. P.; Dunn, B.; Simon, P. Efficient Storage Mechanisms for Building Better Supercapacitors. *Nat. Energy* **2016**, *1* (6), 16070. https://doi.org/10.1038/nenergy.2016.70.

(150) Wang, Y.; Su, S.; Cai, L.; Qiu, B.; Wang, N.; Xiong, J.; Yang, C.; Tao, X.; Chai, Y. Monolithic Integration of All-in-One Supercapacitor for 3D Electronics. *Adv. Energy Mater.* **2019**, *9* (15), 1900037. https://doi.org/10.1002/aenm.201900037.

(151) Andreas, H. A. Self-Discharge in Electrochemical Capacitors: A Perspective Article. *J. Electrochem. Soc.* **2015**, *162* (5), A5047–A5053. https://doi.org/10.1149/2.0081505jes.

(152) Behera, P. K.; Pattnaik, M. Design and Control of DC–DC Converters in a PV-Based LVDC Microgrid BT - DC—DC Converters for Future Renewable Energy Systems; Priyadarshi, N., Bhoi, A. K., Bansal, R. C., Kalam, A., Eds.; Springer Singapore: Singapore, 2022; pp 1–29. https://doi.org/10.1007/978-981-16-4388-0_1.

(153) Conway, B. E.; Pell, W. G.; Liu, T.-C. Diagnostic Analyses for Mechanisms of Self-Discharge of Electrochemical Capacitors and Batteries. *J. Power Sources* **1997**, *65* (1), 53–59. https://doi.org/https://doi.org/10.1016/S0378-7753(97)02468-3.

(154) Zhang, Q.; Rong, J.; Ma, D.; Wei, B. The Governing Self-Discharge Processes in Activated

Carbon Fabric-Based Supercapacitors with Different Organic Electrolytes. *Energy Environ. Sci.* **2011**, *4* (6), 2152–2159. https://doi.org/10.1039/C0EE00773K.

(155) Kowal, J.; Avaroglu, E.; Chamekh, F.; Šenfelds, A.; Thien, T.; Wijaya, D.; Sauer, D. U. Detailed Analysis of the Self-Discharge of Supercapacitors. *J. Power Sources* **2011**, *196* (1), 573–579.

(156) Tevi, T.; Yaghoubi, H.; Wang, J.; Takshi, A. Application of Poly (p-Phenylene Oxide) as Blocking Layer to Reduce Self-Discharge in Supercapacitors. *J. Power Sources* **2013**, *241*, 589–596. https://doi.org/https://doi.org/10.1016/j.jpowsour.2013.04.150.

(157) Xia, M.; Nie, J.; Zhang, Z.; Lu, X.; Wang, Z. L. Suppressing Self-Discharge of Supercapacitors via Electrorheological Effect of Liquid Crystals. *Nano Energy* **2018**, *47*, 43–50. https://doi.org/https://doi.org/10.1016/j.nanoen.2018.02.022.

(158) Chen, L.; Bai, H.; Huang, Z.; Li, L. Mechanism Investigation and Suppression of Self-Discharge in Active Electrolyte Enhanced Supercapacitors. *Energy Environ. Sci.* **2014**, *7* (5), 1750–1759.

(159) Wang, Z.; Chu, X.; Xu, Z.; Su, H.; Yan, C.; Liu, F.; Gu, B.; Huang, H.; Xiong, D.; Zhang, H. Extremely Low Self-Discharge Solid-State Supercapacitors via the Confinement Effect of Ion Transfer. *J. Mater. Chem. A* **2019**, *7* (14), 8633–8640.

(160) Abo-Farha, S. A.; Abdel-Aal, A. Y.; Ashour, I. A.; Garamon, S. E. Removal of Some Heavy Metal Cations by Synthetic Resin Purolite C100. *J. Hazard. Mater.* **2009**, *169* (1), 190–194. https://doi.org/https://doi.org/10.1016/j.jhazmat.2009.03.086.

(161) Ran, J.; Wu, L.; He, Y.; Yang, Z.; Wang, Y.; Jiang, C.; Ge, L.; Bakangura, E.; Xu, T. Ion Exchange Membranes: New Developments and Applications. *J. Memb. Sci.* **2017**, *522*, 267–291. https://doi.org/https://doi.org/10.1016/j.memsci.2016.09.033.

(162) Silva, R. A.; Hawboldt, K.; Zhang, Y. Application of Resins with Functional Groups in the Separation of Metal Ions/Species – a Review. *Miner. Process. Extr. Metall. Rev.* **2018**, *39* (6), 395–413. https://doi.org/10.1080/08827508.2018.1459619.

(163) Antiohos, D.; Folkes, G.; Sherrell, P.; Ashraf, S.; Wallace, G. G.; Aitchison, P.; Harris, A. T.; Chen, J.; Minett, A. I. Compositional Effects of PEDOT-PSS/Single Walled Carbon Nanotube Films on Supercapacitor Device Performance. *J. Mater. Chem.* **2011**, *21* (40), 15987–15994. https://doi.org/10.1039/C1JM12986D.

(164) Duay, J.; Gillette, E.; Liu, R.; Lee, S. B. Highly Flexible Pseudocapacitor Based on Freestanding Heterogeneous MnO2/Conductive Polymer Nanowire Arrays. *Phys. Chem. Chem. Phys.* **2012**, *14* (10), 3329–3337. https://doi.org/10.1039/C2CP00019A.

(165) DiCarmine, P. M.; Schon, T. B.; McCormick, T. M.; Klein, P. P.; Seferos, D. S. Donor–Acceptor Polymers for Electrochemical Supercapacitors: Synthesis, Testing, and Theory. *J. Phys. Chem. C* **2014**, *118* (16), 8295–8307. https://doi.org/10.1021/jp5016214.

(166) Li, Y.; Ren, G.; Zhang, Z.; Teng, C.; Wu, Y.; Lu, X.; Zhu, Y.; Jiang, L. A Strong and Highly Flexible Aramid Nanofibers/PEDOT: PSS Film for All-Solid-State Supercapacitors with Superior Cycling Stability. *J. Mater. Chem. A* **2016**, *4* (44), 17324–17332.

(167) Malti, A.; Edberg, J.; Granberg, H.; Khan, Z. U.; Andreasen, J. W.; Liu, X.; Zhao, D.; Zhang, H.; Yao, Y.; Brill, J. W.; Engquist, I.; Fahlman, M.; Wågberg, L.; Crispin, X.; Berggren, M. An Organic Mixed Ion-Electron Conductor for Power Electronics. *Adv. Sci.* **2015**, *3* (2), 1500305. https://doi.org/10.1002/advs.201500305.

(168) Niu, J.; Conway, B. E.; Pell, W. G. Comparative Studies of Self-Discharge by Potential Decay and Float-Current Measurements at C Double-Layer Capacitor and Battery Electrodes. *J. Power Sources* **2004**, *135* (1), 332–343.

https://doi.org/https://doi.org/10.1016/j.jpowsour.2004.03.068.

(169) Ricketts, B. W.; Ton-That, C. Self-Discharge of Carbon-Based Supercapacitors with Organic Electrolytes. *J. Power Sources* **2000**, *89* (1), 64–69. https://doi.org/https://doi.org/10.1016/S0378-7753(00)00387-6.

(170) Andreas, H. A.; Lussier, K.; Oickle, A. M. Effect of Fe-Contamination on Rate of Self-Discharge in Carbon-Based Aqueous Electrochemical Capacitors. *J. Power Sources* **2009**, *187* (1), 275–283.

(171) Tehrani, P.; Kanciurzewska, A.; Crispin, X.; Robinson, N. D.; Fahlman, M.; Berggren, M. The Effect of PH on the Electrochemical Over-Oxidation in PEDOT:PSS Films. *Solid State Ionics* **2007**, *177* (39), 3521–3527. https://doi.org/https://doi.org/10.1016/j.ssi.2006.10.008.

(172) Rinne, J.; Keskinen, J.; Berger, P. R.; Lupo, D.; Valkama, M. Viability Bounds of M2M Communication Using Energy-Harvesting and Passive Wake-Up Radio. *IEEE Access* **2017**, *5*, 27868–27878. https://doi.org/10.1109/ACCESS.2017.2713878.

(173) Luo, Y.; Pu, L.; Wang, G.; Zhao, Y. RF Energy Harvesting Wireless Communications: RF Environment, Device Hardware and Practical Issues. *Sensors* . 2019. https://doi.org/10.3390/s19133010.

(174) Yang, H.; Zhang, Y. Self-Discharge Analysis and Characterization of Supercapacitors for Environmentally Powered Wireless Sensor Network Applications. *J. Power Sources* **2011**, *196* (20), 8866–8873. https://doi.org/https://doi.org/10.1016/j.jpowsour.2011.06.042.

(175) Keskinen, J.; Lehtimäki, S.; Dastpak, A.; Tuukkanen, S.; Flyktman, T.; Kraft, T.; Railanmaa, A.; Lupo, D. Architectural Modifications for Flexible Supercapacitor Performance Optimization. *Electron. Mater. Lett.* **2016**, *12* (6), 795–803. https://doi.org/10.1007/s13391-016-6141-y.